Multimodal Image Registration Applied to Magnetic Resonance and Ultrasound Prostatic Images

Jhimli Mitra

A Dissertation Presented to the Faculty of
Université de Bourgogne and Universitat de Girona
in Candidacy for the Degree of
Doctor of Philosophy.

Supervisor(s): Prof. Fabrice Meriaudeau (France) and Dr. Robert Martí (Spain)

Dedicated to all the prostate cancer patients

Acknowledgments

I would like to thank Prof. Fabrice Meriaudeau and Dr. Robert Martí for their extreme support and guidance towards the completion of this thesis. Their expertise in the field of computer vision and biomedical imaging have substantially contributed in achieving the goals. I would like to equally convey my gratitude to Dr. Xavier Lladó, Dr. Arnau Oliver and Dr. Désiré Sidibé for being my co-supervisors and for their painstaking efforts in reviewing each and every details of the conference and journal papers that have been published during the thesis period. The timely and detailed feedbacks provided by them have helped me to attain perfection in writing conference or journal papers.

Considering the goals of this thesis, the 'thanksgiving' list is never complete without mentioning the contribution of the radiologist Dr. Joan C. Vilanova and the urologist Dr. Josep Comet from Girona Magnetic Resonance Center and Hospital Dr. Josep Trueta respectively. I specially thank you both for your kind support and prompt responses despite your extremely busy schedules. Without their help it would not have been possible to understand the prostate anatomy and the different hypertrophies of the prostate gland.

The thesis would not have been complete without the generous support of Dr. Zoltan Kato. The adaptation of his mathematical model for the development of a prostate-specific non-rigid registration algorithm has been a major breakthrough in the thesis. I specially thank you Dr. Kato for the enriching discussions related to the development of the thesis.

I would like to also extend my gratitude to the secretaries of Laboratoire Le2i, Mrs. Nathalie Choffay and Ms. Clémence Fontaine, and Ms. Joseta Roca and Mrs. Aina Roldan of VICOROB, who have helped me deal with official matters more

efficiently and so I could devote more time into my research. Finally, the love and support of my father, mother, younger sister and parents-in-law have provided me the strength to continue my research. Nonetheless, the constant source of inspiration and motivation has been my husband Mr. Soumya Ghose who has enthusiastically (irrespective of any hour of the day) contributed to important solutions to my research problems.

Abstract

This thesis investigates the employment of different deformable registration techniques to register pre-operative magnetic resonance and inter-operative ultrasound images during prostate biopsy. Accurate registration ensures appropriate biopsy sampling of malignant prostate tissues and reduces the rate of re-biopsies. Therefore, we provide comparisons and experimental results for some landmark- and intensity-based registration methods: thin-plate splines, free-form deformation with B-splines. The primary contribution of this thesis is a new spline-based diffeomorphic registration framework for multimodal images. In this framework we ensure diffeomorphism of the thin-plate spline-based transformation by incorporating a set of non-linear polynomial functions. In order to ensure clinically meaningful deformations we also introduce the approximating thin-plate splines so that the solution is obtained by a joint-minimization of the surface similarities of the segmented prostate regions and the thin-plate spline bending energy. The method to establish point correspondences for the thin-plate spline-based registration is a geometric method based on prostate shape symmetry but a further improvement is suggested by computing the Bhattacharyya metric on shape-context based representation of the segmented prostate contours. The proposed deformable framework is computationally expensive and is not well-suited for registration of inter-operative images during prostate biopsy. Therefore, we further investigate upon an off-line learning procedure to learn the deformation parameters of a thin-plate spline from a training set of pre-operative magnetic resonance and its corresponding inter-operative ultrasound images and build deformation models by applying spectral clustering on the deformation parameters. Linear estimations of these deformation models are then applied on a test set of inter-operative and pre-operative ultrasound and magnetic resonance images

respectively. The problem of finding the pre-operative magnetic resonance image slice from a volume that matches the inter-operative ultrasound image has further motivated us to investigate on shape-based and image-based similarity measures and propose for slice-to-slice correspondence based on joint-maximization of the similarity measures.

Resum

En aquesta tesi s'investiga l'ús de diferents tècniques de registre deformable per registrar imatges de ressonància magnètica preoperatòries i imatges d'ultrasò interoperatòries en la biòpsia de pròstata. Un registre correcte garanteix l'adequada presa de mostres de biòpsia dels teixits malignes de la pròstata i redueix la taxa de re-biòpsies. Aquesta tesis inicialment presenta una comparació i resultats experimentals d'uns dels mètodes de registre més utilitzats basats en intensitat i en punts (landmarks): thin-plate splines i deformacions free form utilitzant B-splines. La principal contribució d'aquesta tesi és una nova metodologia de registre per imatges multimodals basada en splines i formulació difeomòrfica. En aquesta metodologia, s'assegura el difeomorfisme de la transformació basada en thin-plate splines mitjançant la incorporació d'un conjunt de funcions polinòmiques no lineals. Per tal de garantir deformacions clínicament significatives també introduïm thin-plate splines aproximants de manera que la solució s'obté mitjançant una minimització conjunta de les similituds de la superfície de les regions de la pròstata segmentades i de l'energia de la curvatura del thin-plate spline.

El mètode per establir les correspondències de punts per el registre en thin-plate splines és un mètode geomètric basat en la simetria de la forma de la pròstata. Alhora, es suggereix una millora addicional basada en la utilització de la mètrica Bhattacharyya en la representació de forma (shape context) dels contorns de la pròstata segmentats.

La metodologia de deformació proposada inicialment és computacionalment costosa i no està ben adaptada per el registre interoperatiu durant la biòpsia de pròstata. Per tant, s'investiga més a fons un procediment d'aprenentatge off-line per aprendre els paràmetres de deformació dels thin-plate splines a partir d'un con-

junt d'entrenament de dades ressonància magnètica preoperatòries i les seves corresponents imatges d'ultrasò interoperatòries i es construeixen models de deformació mitjançant l'aplicació de mètodes d'agrupació espectral (spectral clustering) en els paràmetres de deformació. Les estimacions lineals d'aquests models de deformació s'apliquen després en un conjunt de test de ressonància magnètica i ultrasò.

El problema de trobar la llesca del volum de ressonància magnètica preoperatòria que coincideixi amb la imatge d'ultrasò interoperatòria ens ha motivat a investigar sobre les mesures de similitud basades en la forma i contingut de la imatge i ens ha portat a proposar un nou mètode per a la correspondència tall a tall basat en la maximització conjunta de les mesures de similitud esmentades.

Résumé

Introduction au problème

Le Cancer de la prostate (CaP) est l'un des problèmes médicaux les plus fréquemment diagnostiqués au sein de la population masculine. En Europe, c'est une tumeur (maligne ou bénigne) concernant 214 cas pour 1000 hommes et représente un type de cancer bien plus nombreux que les autres, comme ceux des poumons ou les cancers colorectaux [25, 71]. Environ 15% des cancers touchant la population masculine sont des CaP dans les pays développés, contre 4% des cancers dans les pays sous-développés [125]. Par conséquent, il est un problème de santé majeur dans les pays développés dotés d'une plus grande proportion d'hommes âgés où il représente la deuxième cause de décès par cancer dans la population masculine [81]. Les premiers stades de CaP sont généralement non-symptomatiques, mais avec l'avancée de la maladie, les hommes peuvent éprouver des difficultés à uriner. Environ 62% des cas de CaP sont diagnostiqués chez des hommes de 65 ans et plus, et 97% se produisent chez des hommes de 50 ans et plus. Par conséquent, de nombreux programmes de dépistage de masse ont été initiés en Europe et aux Etats-Unis depuis les 15 dernières années, programmes ciblants des populations jugées à risque de CaP [6, 42, 136]. L'objectif des programmes de dépistage est de détecter plus d'adénocarcinomes (malignes formes du CaP) et ainsi de réduire le taux de mortalité dû au cancer de la prostate, le taux de survie est cependant fortement influencée par le délai de diagnostic.

Le diagnostic du cancer de la prostate est principalement fait par toucher rectal (TR), par mesure de la concentration de l'antigène prostatique spècifique (PSA) et par l'échographie transrectale (ETR). Son diagnostic définitif dépend de la présence

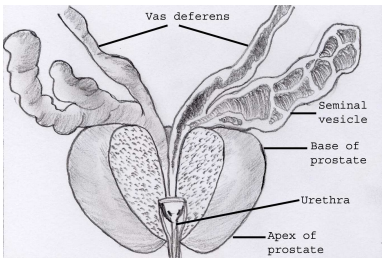

(e) Base-Apex régions de la prostate

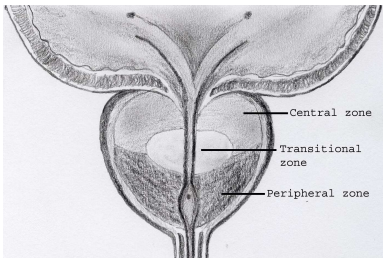

(f) Prostate par zones

Figure 1: Prostate anatomie.

d'un adénocarcinome dans les tissus biopsiés de la prostate. Environ 68% des cancers de la prostate sont principalement situés dans la zone périphérique par rapport à 24% dans la zone de transition et 8% dans la zone centrale de la prostate [107](voir la Figure 1). L'examen médical TR permet de déceler des excroissances de plus de $0,2$ ml. Une valeur du PSA de plus de $4,0$ ng/ml avec une vitesse de PSA de $0,4$ à $0,75$ ng/ml/an peut être considérée comme étant associée au risque de cancer de la prostate [29]. Toutefois, les niveaux de PSA peuvent également augmenter en raison de l'élargissement de la prostate, par exemple pour l'hyperplasie prostatique bénigne. Par conséquent, les niveaux de TR et de PSA ne suffisent pas à eux seuls pour statuer sur le'éventualité d'un cancer de la prostate et doivent être suivis d'une biopsie.

Les biopsies de la prostate guidée par échographie sont maintenant une norme suivie par les urologues. La plupart des biopsies sont effectuées en utilisant une approche transrectale. Porter et al. [126] suggère $10-12$ prèlévements par biopsie par rapport à la British Prostate Testing for Cancer and Treatment Study qui en recommandait 10 [45]. La figure 2 montre les zones typiques de biopsie guidée par échographie.

L'aspect le plus commun pour les cancers de la prostate en échographie transrectale (ETR) est une lésion hypoéchogène (zone foncée par rapport au tissu normal) dans la zone périphrique. Cependant, seulement 43% des lésions hypoéchogènes de la zone périphérique sont des tumeurs malignes. Les tissus cancéreux peuvent également apparaitre comme des zones isoéchogènes dans $25\% - 42\%$ des cas, bien que les tissus isoéchogènes soient normalement associées à des tissus sains. La Figure

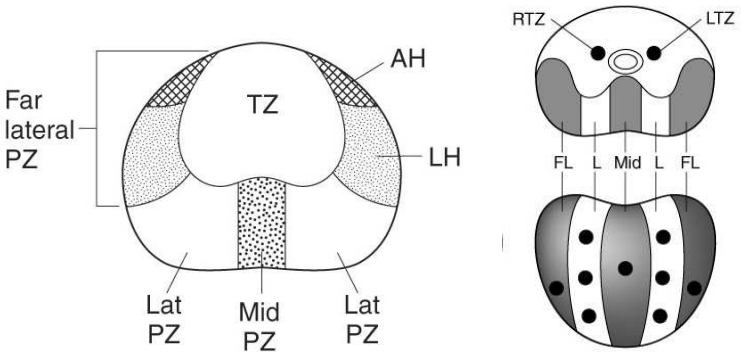

(a) Zones de biopsie de la prostate (b) Typique 11-noyau biopsie

Figure 2: Les sites de biopsie de la prostate. (a) Un modèle pour les zones de biopsie de la prostate. PZ-peripheral zone, Mid PZ-Mid peripheral zone, Lat PZ-Lateral peripheral zone, AH-Anterior horn, LH-Lateral Horn, TZ-Transition zone; (b) Un modèle de biopsie multi-dirigée de la prostate. Image courtesy Carroll et al. [29]

3 montre deux cas de lésions hypoéchogènes et isoéchogène CaP. En revanche, les modalités T1 et T2 en imagerie IRM permettent d'apprécier pleinement l'anatomie de la prostate ainsi que les tissus cancéreux [34, 4, 128, 17](voir la Figure 4).

Par conséquent, l'IRM peut servir de test de triage pour les hommes jugés à risque de CaP et permettre ainsi de réduire le nombre de re-biopsies tout en fournissant des informations plus utiles pour les patients qui sont envoyés pour une biopsie. Par conséquent, la fusion des deux modalités, images IRM pré-biopsie et images ETR inter-opératoires pourraient augmenter la précision globale des prélèvements lors de la biopsie [75, 85, 142, 168].

Dans cette thèse, nous avons exploré différentes méthodes de recalage déformables pouvant être appliquées entre les images IRM et les images ETR acquises pendant la biopsie. Nous avons observé à partir d'une étude de la littérature que les méthodes de recalage déformables existantes pour le recalage des images de prostate multimodales ne fournissent pas de précisions satisfaisantes et que la plupart sont coûteuse en ressources informatiques, notre méthode proposée n'étant pas une exception à cette tendance. Dans ce contexte, **notre objectif secondaire a été de rechercher une méthode de recalage déformable qui puisse être appliquée au cours des interventions (nécessitant du temps réel). Par**

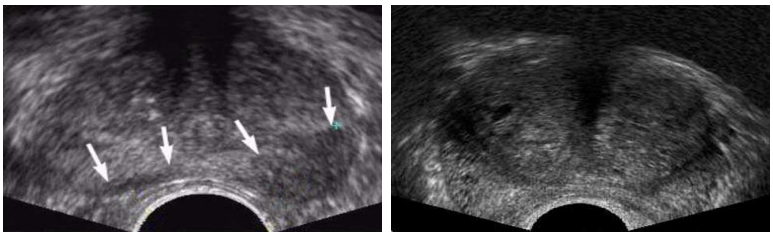

(a) Adénocarcinome hypoéchogène (b) Adénocarcinome isoéchogène

Figure 3: L'échographie de CaP (adénocarcinome). (a) Axial ETR montre une zone hypoéchogène dans la zone périphérique gauche et une petite zone hypoéchogène dans la zone périphérique droite (les flèches). La biopsie a révélé un adénocarcinome; (b) Axial ETR balayage d'un patient présentant des signes cliniques hyperplasie bénigne de la prostate. L'élargissement de la zone de transition est présent, mais aucune anomalie focale est observée dans la zone périphérique. Une biopsie a révélé un adénocarcinome de deux lobes de la prostate (c'est une tumeur isoéchogène dans la zone périphérique des deux lobes de la prostate). Copyright © 1994-2012 par WebMD LLC.

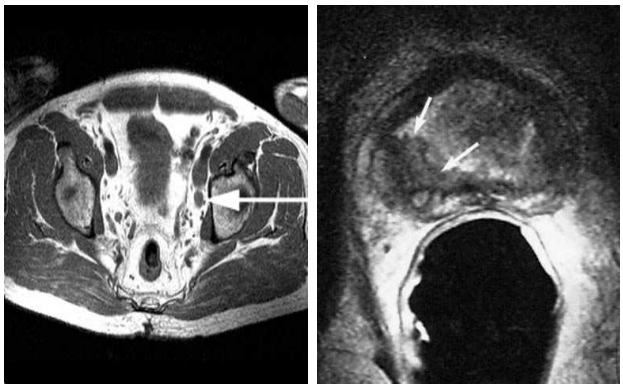

(a) (b)

Figure 4: IRM de la prostate. (a) T1-pondéré IRM image du bassin montre un noeud obturateur élargie gauche (flèche) révélée par une biopsie du cancer, (b) endorectale, axiale, T2 image IRM d'un patient atteint d'un cancer du côté droit de la prostate. Signal de faible intensité est démontré dans la zone périphérique droite (flèche). Copyright ©1994-2012 par WebMD LLC.

conséquent, nous proposons un schéma d'apprentissage où les paramètres de déformation sont appris sur une série d'images d'entraînement puis modélisés et une estimation linéaire de ces modèles est ensuite appliquée pour recaler les images ETR-IRM . Cette solution assure une vitesse de calcul sans compromettre beaucoup la précision de recalage.

Dans les expérimentations réalisées pour valider nos travaux, la sonde transrectale de biopsie n'était pas équippée pour permettre une localisation 3D (par conséquent, la position spatiale (coordonnée z) des ETR images par rapport au système d'imagerie n'était pas disponible). Toutefois, pour la fusion ETR-IRM, il est important d'identifier la coupe pré-biopsie axiale IRM qui correspond à l'image ETR acquise au cours de la biopsie. Par conséquent, **un autre objectif de ce travail a été d'identifier automatiquement la coupe axiale IRM d'un volume pré-biopsie correspondant à l'image ETR en utilisant une méthode qui exploite les métriques de similarité basées sur l'image et la forme**.

Les solutions proposées

Les principales contributions de cette thèse sont les suivantes:

1. Une nouvelle méthode non linéaire de recalage déformable, spécifique à la prostate est proposée afin de minimiser l'erreur algébrique entre les masques binaires d'une image fixe et d'une image transformée en mouvement. L'image ETR de la prostate est l'image fixe et l'image IRM est l'image en mouvement dans toutes nos expérimentations.

2. Une méthode pour apprendre les paramètres de déformation hors-ligne est proposée pour améliorer la vitesse de recalage entre l'image fixe et l'image en mouvement afin d'être applicable en temps réel pendant les interventions.

3. Une méthode automatique pour identifier la coupe axiale IRM à partir d'un volume prè-biopsie qui corresponde bien a l'image ETR vue lors de la biopsie est proposée.

Les résumés des trois contributions sont fournis dans les paragraphes suivants.

Recalage non-linéaire déformable

Méthode: Nous présentons une nouvelle méthode de recalage non-rigide de l'échographie transrectale et des images IRM de la prostate basée sur un cadre non-linéaire régularisée de correspondances de points obtenus à partir d'une mesure statistique des contextes de formes [14]. Les formes de la prostate segmentée sont représentées par des contextes de formes et la distance de Bhattacharyya entre les représentations de formes est utilisée pour trouver les points de correspondance entre les images 2D fixe et en mouvement. La méthode de recalage exploite l'estimation paramétrique d'un difféomorphisme non-linéaire entre les images multimodales et est basée sur la solution d'un ensemble d'équations non-linéaires de thin-plate splines. La solution est obtenue comme la solution des moindres carrés d'un système sur déterminé d'équations non linéaires construits par l'intégration d'un ensemble de fonctions non linéaires définies sur les images fixes et en mouvement. Toutefois, ceci ne peut aboutir à des transformations cliniquement acceptables respectant des objectifs anatomiques. Par conséquent, l'énergie de flexion régularisée des thin-plate splines ainsi que l'erreur de localisation de correspondances établies ont été incluses dans le système d'équations.

Résultats: La méthode de recalage déformable proposée est comparée aux méthodes de recalage basées sur des thin-plate splines [23] et sur des B-splines [137] ainsi qu'à deux autres variantes de la méthode proposée. Des évaluations quantitatives sur 20 patients montrent que la méthode proposée donne un coefficient similarité (DSC) de $0,980 \pm 0.004$ avec une erreur de recalage des objectifs anatomiques de $1,60 \pm 1.17$ mm et est statistiquement-significativement meilleure avec $p < 0,0006$ que les autres méthodes. La méthode proposée montre ègalement une meilleure précision dans le recalage des images des glandes non-centrales. La Figure 5 montre un résultat qualitatif de la méthode de recalage proposée.

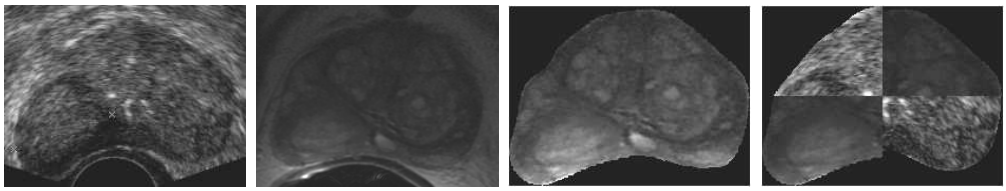

Figure 5: Les résultats qualitatifs de recalage. Les deux premières colonnes sont les images ETR et IRM respectivement, suivis par le résultat de fusion et un affichage de l'image ETR et de l'image transforme IRM en damier.

L'apprentissage des paramètres de déformation

Méthode: Nous proposons une méthode pour apprendre les paramètres de déformation hors-ligne pour le recalage rapide des images ETR et IRM de la prostate au cours de la biopsie guidée. La méthode est basée sur une phase d'apprentissage lorsque les modèles de déformation sont construits à partir des paramètres de déformation non-linéaire d'une thin-plate spline utilisée pour recaler un ensemble d'images entraînement ETR et IRM de la prostate en utilisant la classification spectrale. Les modèles de déformation comprenant des eigen-modes (modes propres) de chaque groupe dans un espace gaussien sont appliqués sur une nouvelle image d'IRM. Le modèle de dformation avec le moins d'erreur de recalage est finalement choisi comme le modèle optimal pour le recalage déformable. Ceci permet de réaliser rapidement le recalage des images multimodales de la prostate tout en conservant une précision de recalage.

Résultats: La validation de la méthode se fait en utilisant une approche de leave-one-out à partir de 25 patients. Une erreur d'alignement de $2,44 \pm 1.17$ mm est atteint, ce qui est cliniquement significatif pour les procédures de biopsie. Néanmoins, le temps de calcul est considérablement réduit à $4,99 \pm 3.52$ secs, ce qui est statistiquement-significativement meilleure avec $p < 0,0001$ par rapport à la méthode sans l'apprentissage des paramètres de déformation. La Figure 6 montre le résultat qualitatif du recalage avec l'apprentissage préalable de paramètres de déformation non-linéaire.

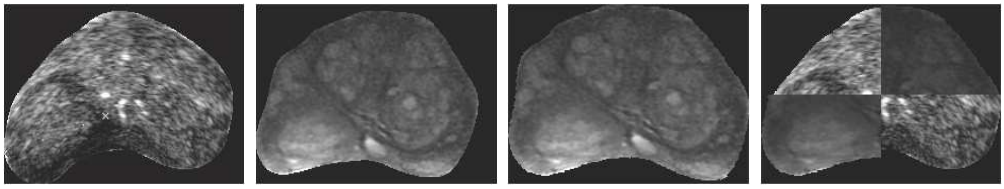

Figure 6: Les résultats de recalage qualitatif de l'apprentissage de déformation hors-ligne. Les deux premières colonnes indiquent l'ETR fixe et l'image IRM en mouvement respectivement. Le 3ème et le 4ème colonnes présentent les résultats de recalage pour la méthode proposée avec des acquis des paramètres de déformation non-linéaire.

La correspondance des tranches 2D ETR-IRM

Méthode: Dans cette partie, nous présentons une nouvelle méthode pour identifier la coupe 2D axiale IRM d'un volume pré-acquis correspondant à la tranche 2D axiale ETR obtenue au cours de biopsie de la prostate. La méthode combine des informations sur la forme et sur l'intensité des images. Les contours segmentés de la prostate dans les deux modalités sont décrits par des contextes de forme et appariés en utilisant la distance du Chi-deux. Les valeurs issues des calculs de l'informations mutuelle normalisée (NMI) et d'inter-corrélation (CC) entre l'ETR et les coupes IRM sont calculés afin de trouver des similarités entre les différentes images. Enfin, les valeurs de probabilité conjointe associant la forme et les indices d similarités d'image sont utilisés dans un cadre à base de règles pour fournir la coupe IRM qui corresponde bien à la coupe ETR acquise au cours de la biopsie.

Résultats: Les résultats sont validés par rapport aux choix des coupes IRM à plus ou moins une coupe obtenue à partir d'un radiologue expert et d'un urologue expert pour 20 patients. On observe que le choix automatique des coupes IRM correspond au moins à l'un des choix des experts pour 18 des cas alors que les experts sont d'accord avec leurs choix pour seulement 11 des cas, signifiant que la précision inter-expert est de 55%, comparativement à un taux global de précision de 90% avec notre méthode automatique. La Figure 7 montre les résultats choix adoptés par les deux experts et par notre méthode.

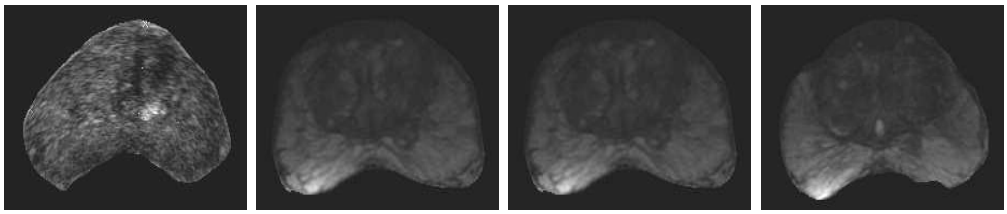

Figure 7: Choix de lacoupe IRM correspondant à la coupe ETR. La première colonne indique la coupe ETR et les deuxième et troisième colonnes montrent les choix adoptés par les deux experts. La dernière colonne montre le choix de la coupe par notre méthode qui est juste une coupe loin des choix des experts et qui est très proche visuellement.

Liste des Publications

Revues

- "A spline-based non-linear diffeomorphism for multimodal prostate registration", J. Mitra, Z. Kato, R. Martí, A. Oliver, X. Lladó, D. Sidibé, S. Ghose, J. C. Vilanova, J. Comet, F. Meriaudeau, *Medical Image Analysis*, In Press, http://dx.doi.org/10.1016/j.media.2012.04.006, May 2012.

- "Prostate multimodality image registration based on B-splines and quadrature local energy", Jhimli Mitra, Robert Martí, Arnau Oliver, Xavier Lladó, Soumya Ghose, Joan C. Vilanova, Fabrice Meriaudeau, *International Journal of Computer Assisted Radiology and Surgery*, vol. 7, pp. 445-454, Heidelberg, Germany, Springer-Verlag, May 2012.

Conferences Intérnationales

- "Spectral clustering to model deformations for fast multimodal prostate registration", J. Mitra, Z. Kato, S. Ghose, D. Sidibé, R. Martí, X. Lladó, A. Oliver, J. C. Vilanova, F. Meriaudeau, IAPR International Conference on Pattern Recognition (ICPR), to appear, Tsukuba, Japan, November 2012.

- "Joint Probability of Shape and Image Similarities to Retrieve 2D TRUS-MR

Slice Correspondence for Prostate Biopsy", J. Mitra, S. Ghose, D. Sidibé, R. Martí, A. Oliver, X. Lladó, J. C. Vilanova, J. Comet, F. Meriaudeau, IEEE Engineering in Medicine and Biology Society (EMBS) Conference, to appear, San Diego, California, USA, Sep-Oct, 2012.

- "Weighted Likelihood Function of Multiple Statistical Parameters to Retrieve 2D TRUS-MR Slice Correspondence for Prostate Biopsy", J. Mitra, S. Ghose, D. Sidibé, A. Oliver, R. Martí, X. Lladó, J. C. Vilanova, J. Comet, F. Meriaudeau, International Conference on Image Processing (ICIP), to appear, Orlando, Florida, USA, September 2012.

- "A shape-based statistical method to retrieve 2D TRUS-MR slice correspondence for prostate biopsy", J. Mitra, A. Srikantha, D. Sidibé, R. Martí, A. Oliver, X. Lladó, S. Ghose, J. C. Vilanova, J. Comet and F. Meriaudeau, Proc. of SPIE Medical Imaging: Image Processing, vol. 8314, pp. 83143M-1-9, San Diego, California, February 2012.

- "A Non-linear Diffeomorphic Framework for Prostate Multimodal Registration", J. Mitra, Z. Kato, F. Meriaudeau, R. Martí, A. Oliver, X. Lladó, S. Ghose, J. C. Vilanova, Proc. of International Conference on Digital Image Computing: Techniques and Applications (DICTA), pp.31-36, Noosa, Australia, December 2011.

- "Quadrature Filter Enhanced B-spline registration applied to prostate multimodal images", J. Mitra, R. Martí, A. Oliver, X. Lladó, S. Ghose, J. C. Vilanova, F. Meriaudeau, Proc. of Computer Assisted Radiology and Surgery (CARS), vol. 6 (supplement 1) pp. S323-S324, Berlin, Germany, June 2011.

- "A comparison of thin-plate splines with automatic correspondences and b-splines with uniform grids for multimodal prostate registration", J. Mitra, R. Martí, A. Oliver, X. Lladó, J. C. Vilanova, and F. Meriaudeau, SPIE Medical Imaging, vol. 7964, pp. 79642T-1-8, Lake Buena Vista, Orlando, Florida, February 2011.

- "Multimodal prostate registration using thin-plate splines from automatic correspondences", J. Mitra, A. Oliver, R. Martí, X. Lladó, J. C. Vilanova, and

F. Meriadeau, Proc. of International Conference on Digital Image Computing: Techniques and Applications (DICTA), pp. 587-592, Sydney, Australia, December 2010.

- "A thin-plate spline based multimodal prostate registration with optimal correspondences", J. Mitra, A. Oliver, R. Martí, X. Lladó, J. C. Vilanova, and F. Meriaudeau, Proc. of International Conference on Signal-Image Technology & Internet-Based Systems (SITIS), pp. 7-11, Kuala Lumpur, Malaysia, December 2010.

Co-auteur de Publications

Revues

- "Statistical shape and texture model of quadrature phase information for prostate segmentation", Soumya Ghose, Arnau Oliver, Robert Martí, Xavier Lladó, Jordi Freixenet, Jhimli Mitra, Joan C. Vilanova, Josep Comet, Fabrice Meriaudeau, *International Journal of Computer Assisted Radiology and Surgery*, vol. 7, issue 1, pp.43-55, Heidelberg, Germany, Springer-Verlag, January 2012.

- "A Survey of Prostate Segmentation Methodologies in Ultrasound, Magnetic Resonance and Computed Tomography Images", Soumya Ghose, Arnau Oliver, Robert Martí, Xavier Lladó, Jordi Freixenet, Jhimli Mitra, Joan C. Vilanova, Désiré Sidibé, Fabrice Meriaudeau, *Computer Methods and Programs in Biomedicine* , In Press, http://dx.doi.org/10.1016/j.cmpb.2012.04.006, June 2012.

Conferences Intérnationales

- "Graph Cut Energy Minimization in a Probabilistic Learning Framework for 3D Prostate Segmentation in MRI", S. Ghose, J. Mitra, A. Oliver, R. Martí, X. Lladó, J. Freixenet, J. C. Vilanova, D. Sidibé, F. Meriaudeau, IAPR International Conference on Pattern Recognition (ICPR), to appear, Tsukuba,

Japan, November 2012.

- "A Mumford-Shah Functional based Variational Model with Contour, Shape, and Probability Prior information for Prostate Segmentation", S. Ghose, J. Mitra, A. Oliver, R. Martí, X. Lladó, J. Freixenet, J. C. Vilanova, J. Comet, D. Sidibé, F. Meriaudeau, IAPR International Conference on Pattern Recognition (ICPR), to appear, Tsukuba, Japan, November 2012.

- "A Supervised Learning Framework for Automatic Prostate Segmentation in TransRectal Ultrasound Images", S. Ghose, J. Mitra, A. Oliver, R. Martí, X. Lladó, J. Freixenet, J. C. Vilanova, J. Comet, D. Sidibé, F. Meriaudeau, Advanced Concepts for Intelligent Vision Systems (ACIVS), to appear, Brno, Czech Republic, September 2012.

- "Spectral Clustering of Shape and Probability Prior Models for Automatic Prostate Segmentation in Ultrasound Images", S. Ghose, J. Mitra, A. Oliver, R. Martí, X. Lladó, J. Freixenet, J. C. Vilanova, J. Comet, D. Sidibé, F. Meriaudeau, IEEE Engineering in Medicine and Biology Society (EMBS) Conference, to appear, San Diego, California, USA, Sep-Oct, 2012.

- "A Coupled Schema of Probabilistic Atlas and Statistical Shape and Appearance Model for 3D Prostate Segmentation in MR Images", S. Ghose, J. Mitra, A. Oliver, R. Martí, X. Lladó, J. Freixenet, J. C. Vilanova, D. Sidibé, F. Meriaudeau, International Conference on Image Processing (ICIP), to appear, Orlando, Florida, USA, September 2012.

- "A hybrid framework of multiple active appearance models and global registration for 3D prostate segmentation in MRI", S. Ghose, A. Oliver, R. Martí, X. Lladó, J. Freixenet, J. Mitra, J. C. Vilanova, J. Comet, and F. Meriaudeau, SPIE Conference on Medical Imaging: Image Processing, vol. 8314, pp. 83140S-1-9, San Diego, California, February 2012.

- "Statistical shape and probability prior model for automatic prostate segmentation", S. Ghose, A. Oliver, R. Martí, X. Lladó, J. Freixenet, J. Mitra, J. C. Vilanova, J. Comet, and F. Meriaudeau, Proc. of International Conference on

Digital Image Computing: Techniques and Applications (DICTA), pp.340-345, Noosa, Australia, December 2011.

- "Multiple mean models of statistical shapes and probability priors for automatic prostate segmentation", Soumya Ghose, Arnau Oliver, Robert Martí, Xavier Lladó, Jordi Freixenet, Jhimli Mitra, Joan C. Vilanova, Josep Comet, Fabrice Meriaudeau, MICCAI Workshop on Prostate Cancer Imaging: Computer Aided Diagnosis, Prognosis, and Intervention, vol. 6963, pp. 35-46, Toronto, Canada, Springer Lecture Notes in Computer Science, September 2011.

- "Quadrature phase-based statistical shape and appearance for prostate segmentation", S. Ghose, A. Oliver, R. Martí, X. Lladó, J. Freixenet, J. Mitra, J. C. Vilanova, F. Meriaudeau, Proc. of CARS 2011, vol. 6 (supplement 1), pp. S12-16, Berlin, Germany, June 2011.

Contents

1 Introduction **1**

1.1 Prostate Cancer 1

1.2 Diagnosis 2

1.3 Transrectal Ultrasound (TRUS) 4

1.4 Magnetic Resonance Imaging (MRI) 5

1.5 Thesis Objectives 8

1.6 Overview of the Thesis 10

2 Preliminaries **13**

2.1 Image Registration: An Overview 13

2.2 The Theory of Image Registration 14

2.2.1 Problem Definition 14

2.2.2 Alignment Measure 15

2.2.3 Geometric Transformations 17

2.2.4 Optimization 18

2.2.5 Interpolation 18

2.3 Evaluation of Image Registration 19

2.4 Summary 20

3 A Literature Review **23**

3.1 Rigid/Affine Registration Applied to Prostate 23

3.2 Deformable Registration Applied to Prostate 27

3.2.1 Radial-basis Transformations 28

3.2.2 Registration based on Deformable Models 29
3.2.3 Registration based on Biomechanical Finite Element Modeling 30
3.2.4 Other Non-parametric Registration Methods 31
3.3 Summary 33

4 Registration based on Radial-Basis Transformations 35
4.1 Point correspondences 35
4.1.1 Automatic Point Correspondences (Geometric) 36
4.2 Thin-plate Splines (TPS) 39
4.3 B-spline free-form deformations (FFDs) 44
4.3.1 Deformation modeling with B-splines 44
4.3.2 Similarity 46
4.3.3 Optimization 47
4.4 A variant of B-splines multimodality registration based on quadrature local energy 48
4.4.1 Quadrature filters 48
4.5 Data and Analysis 51
4.6 Results and Discussions 53
4.7 Conclusions 56

5 A Spline-based Non-linear Diffeomorphism for Prostate Registration 59
5.1 Introduction 60
5.2 Shape-contexts and point correspondences 61
5.3 Non-linear Diffeomorphism 66
5.4 Experimental setup 70
5.5 Experiments and Results 71
5.5.1 Control Points 71
5.5.2 Registration Methods 73
5.5.3 Automatic Segmentation 77
5.5.4 Registration of Non Mid-Gland Slices 83
5.5.5 Statistical Analysis 85

5.6 Discussions 91
5.7 Conclusions 93

6 Off-line Deformation Learning for Fast Multimodal Registration 95
6.1 Introduction 95
6.2 Learning Prostate Deformations 97
6.2.1 Spectral Clustering 98
6.2.2 Linear Estimation 99
6.3 Experiments and Results 100
6.4 Conclusions 101

7 2D TRUS-MRI Slice Correspondence for Prostate Biopsy 103
7.1 Introduction 103
7.2 The Slice Correspondence Method 104
7.2.1 Shape Similarity 105
7.2.2 Image Similarities 106
7.2.3 Choosing the Best Matching MR Slice 106
7.3 Results and Discussions 107
7.4 Conclusions 110

8 Conclusions 111

Publications 115

Bibliography 120

List of Figures

1 Prostate anatomie. viii
2 Les sites de biopsie de la prostate ix
3 L'échographie de CaP (adénocarcinome) x
4 IRM de la prostate x
5 Les résultats qualitatifs de recalage xiii
6 Les résultats de recalage qualitatif de l'apprentissage de déformation hors-ligne xiv
7 Choix de la coupe IRM correspondant à la coupe ETR xv

1.1 Prostate anatomy 2
1.2 Prostate biopsy sites 3
1.3 Ultrasonography of PCa (adenocarcinoma) 4
1.4 Transverse sonogram showing hypertrophy 5
1.5 MRI of the prostate 6
1.6 Multiparametric MRI 7

2.1 A schema of a typical image registration algorithm. 14

4.1 Method of generating correspondence points in different resolutions. . 38
4.2 Point correspondences example with modified internal points 39
4.3 Geometric methods for correspondence points generation. 40
4.4 Points correspondences with different methods of contour sampling . . 40
4.5 Fundamental solution of the biharmonic equation 41
4.6 An example TPS transformation with correspondences established across the fixed and the moving images 44

4.7 B-splines control point mesh 45
4.8 A schematic diagram of the proposed algorithm. 49
4.9 Even and Odd log-Gabor quadrature filter pairs in spatial domain. . . 49
4.10 Application of quadrature filters on TRUS and MR images 52
4.11 B-splines control grid with 2 refinements over the initial placement . . 53
4.12 Qualitative comparison of results using different registration methods 58

5.1 Schema diagram of the proposed registration framework. 62
5.2 Uniformly sampled contours 63
5.3 Point correspondences example with shape-context histograms 64
5.4 Point correspondences on TRUS and MR prostate contours using Bhattacharyya distance 65
5.5 Point correspondences on TRUS and MR images 66
5.6 6 point correspondences on the boundary with 3 internal points and 1 point on prostate centroid 72
5.7 10 Point correspondences on the boundary with 5 internal points and 1 point on prostate centroid 73
5.8 8 Point correspondences on the boundary with no internal points or centroid 75
5.9 Deformation of the prostate gland with different sets of control points for Patient 6 76
5.10 Qualitative registration results of NLTPS-UNI, NLTPS-CORR and NLTPS-REGCORR 80
5.11 Qualitative registration results for TPS, B-splines compared with the proposed method (NLTPS-REGCORR) 81
5.12 Qualitative registration results with point correspondences established according to automatically segmented prostate contours 82
5.13 Qualitative results of the proposed method when applied to non mid-gland slice 84
5.14 TRE means for different methods 87
5.15 Kruskal-Wallis comparison of medians of ranked TRE values 89
5.16 TRE means for different methods with statistically significant difference 90

6.1 Point correspondences example 97

6.2 Qualitative registration results 101

7.1 TRUS-MR corresponding slices 109

List of Tables

4.1 A comparison of registration accuracies of the B-spline registration with NMI computed from intensities, from texture and TPS registration 54

5.1 A comparison of global and local registration accuracies for the proposed method with varying control points 74

5.2 A comparison of registration accuracies of the non-linear TPS registration NLTPS-UNI, NLTPS-CORR, NLTPS-REGCORR, traditional TPS and B-splines 78

5.3 Comparison of registration accuracies in terms of 95% HD and timing requirements for NLTPS-UNI, NLTPS-CORR and NLTPS-REGCORR, TPS and B-splines registration methods 79

5.4 Quantitative global and local registration accuracies when automatic segmentation ([62]) method is used 83

5.5 Slice-by-slice registration accuracies for base to apex slices 85

5.6 Quantitative registration results for mid-gland and off mid-gland registration with manual or automatic segmentation on different patient cohorts. 85

5.7 A comparison of the global and local registration accuracies for the different methods and their statistical significance 86

6.1 Registration accuracies and computation time for different methods . 100

7.1 Expert choices and the results for the MR slices corresponding to a TRUS slice obtained by our method 108

Chapter 1

Introduction

The aim of this research is to search for a registration method with good accuracy that would facilitate sampling of prostate tissues during transrectal ultrasound guided needle biopsy. In this chapter we elaborate on prostate cancer, diagnosis of prostate cancer, imaging modalities involved in the diagnosis of prostate cancer like ultrasound and magnetic resonance imaging and provide the objectives for our research. Finally, we provide the general image registration framework and overview of the remaining chapters in the thesis.

1.1 Prostate Cancer

Prostate cancer (PCa) is one of the most frequently diagnosed medical problems facing the male population. In Europe it is a common solid neoplasm with an incidence rate of 214 cases per 1000 men outnumbering others like lung and colorectal cancers [25, 71]. An estimate of $240,890$ new cases of PCa had been made for US in 2011 [143]. About 15% of male cancers are PCa in developed countries compared to 4% of male cancers in undeveloped countries [125]. Therefore it is a major health concern in developed countries with its greater proportion of elderly men and is also the second leading cause of cancer deaths in men [81].

Early stages of PCa are usually non-symptomatic, however with the advanced disease, men may experience difficulties in urinating. There are three well-established risk factors associated with PCa: increasing age, ethnicity and heredity. About 62%

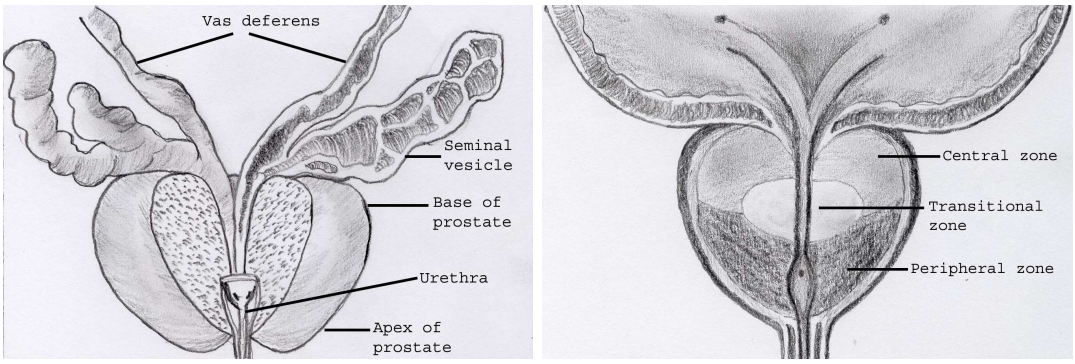

(a) Prostate Base-Apex regions (b) Prostate by zones

Figure 1.1: Prostate anatomy

of all prostate cancer cases are diagnosed in men 65 years of age and older, and 97% occur in men 50 and older. African American men and Jamaican men of African descent have the highest prostate cancer incidence rates in the world. Strong familial predisposition is also contributes to 5% – 10% of PCa. Therefore, mass screening programs have been existent in Europe and USA for the past 15 years targeting asymptomatic men deemed to be at risk of PCa [6, 42, 136]. The goal of the screening programs is to detect more and more adenocarcinomas and reduce the mortality rate from PCa, while survival rate is strongly influenced by the lead-time from diagnosis.

1.2 Diagnosis

The diagnosis of PCa is primarily done by Digital Rectal Examination (DRE), serum concentration of Prostate Specific Antigen (PSA) and Transrectal Ultrasonography (TRUS). Its definitive diagnosis depends on the presence of adenocarcinoma in prostate biopsy cores and thereafter a histopathological examination allows the grading and determination of the extent of tumor growth. A larger proportion of about 68% of prostate cancers are located mostly in the peripheral zone compared to 24% in transition zone and 8% in the central zone of the prostate [107] (see Figure 1.1 for prostate zone anatomy). Therefore prostate volumes of more than 0.2 ml can be determined by DRE and may be recommended for a follow-up biopsy.

The measurement of PSA level has revolutionized the diagnosis of PCa [146]. A

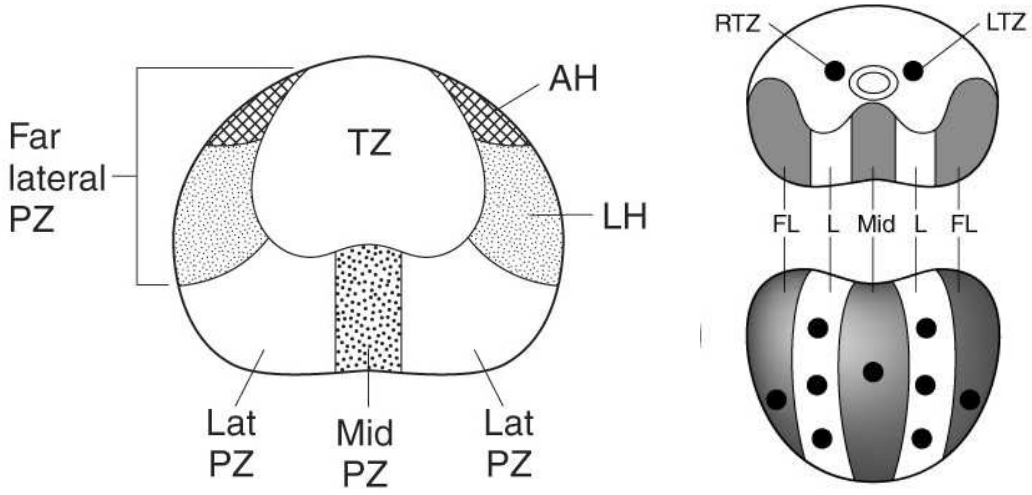

(a) Prostate biopsy zones (b) Typical 11-core biopsy

Figure 1.2: Prostate biopsy sites. (a) A template for prostate biopsy zones. PZ-peripheral zone, Mid PZ-Mid peripheral zone, Lat PZ-Lateral peripheral zone, AH-Anterior horn, LH-Lateral Horn, TZ-Transition zone; (b) A template for multisite-directed prostate biopsy. Image courtesy Carroll et al. [29]

PSA level of over 4.0 ng/mL with a PSA velocity of $0.4 - 0.75$ ng/mL/yr may be considered to be associated with the risk of PCa [29]. However, PSA levels may also be increased due to prostate enlargement i.e. benign prostatic hyperplasia. Therefore, DRE and PSA levels are inconclusive about PCa without biopsies.

Prostate biopsies guided by ultrasound is now a standard followed by urologists. Most biopsies are done using a transrectal approach although some urologists prefer the transperineal approach. The sample sites for a biopsy should be as far posterior and lateral as possible in the peripheral gland. Additional cores may also be obtained from suspect areas determined by DRE/TRUS that are chosen on an individual basis. A glandular volume of $30 - 40$ mL requires at least 8 cores to be sampled while more than 12 cores are not significantly more conclusive [49]. Porter et al. [126] suggests $10 - 12$ core biopsies while the British Prostate Testing for Cancer and Treatment Study has recommended 10 core biopsies [45]. Figure 1.2 shows the typical biopsy zones for ultrasound guided prostate biopsy.

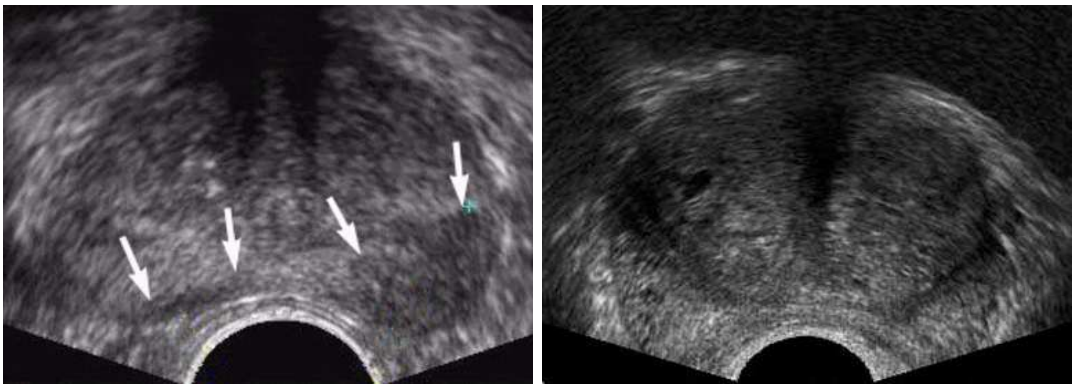

(a) Hypoechoic Adenocarcinoma (b) Isoechoic Adenocarcinoma

Figure 1.3: Ultrasonography of PCa (adenocarcinoma). (a) Axial TRUS scan shows a hypoechoic area in the left peripheral zone and a small hypoechoic area in right peripheral zone (arrows). Biopsy revealed an adenocarcinoma; (b) Axial TRUS scan in a patient with clinical benign prostatic hyperplasia. Enlargement of the transition zone is present, but no focal abnormality is observed in the peripheral zone. A systematic, 6-core biopsy revealed adenocarcinoma from both lobes of the prostate (i.e. this is an isoechoic tumor in the peripheral zone of both prostatic lobes). Copyright © 1994-2012 by WebMD LLC.

1.3 Transrectal Ultrasound (TRUS)

The TRUS procedure involves laying the patient down in either the right or left lateral decubitus position that allows easy insertion of the ultrasound probe. A 5.0 to 7.5 mHz transducer probe is gently advanced into the rectum, to the base of the bladder until the seminal vesicles are visualized. Transverse images are then obtained as the probe is moved back from the prostate base to the prostate apex. The most common appearance for PCa is a hypoechoic lesion (dark compared to normal tissue) in the peripheral zone. The chance of a hypoechoic peripheral zone lesion being malignant has a sensitivity of 85.5%, specificity of 28.4%, a positive predictive value of 29%, a negative predictive value of 85.2% and an overall accuracy of 43% [46]. The prevalence of isoechoic PCa lesions on TRUS ranges from 25% – 42% while isoechoic tissues are normally associated with healthy prostate tissues. Figure 1.3 shows two cases of hypoechoic and isoechoic PCa lesions.

An 18-gage biopsy needle with spring-action attached to the end-firing or side-firing biopsy probe is used to procure multiple 1.5 cm prostate biopsy specimens

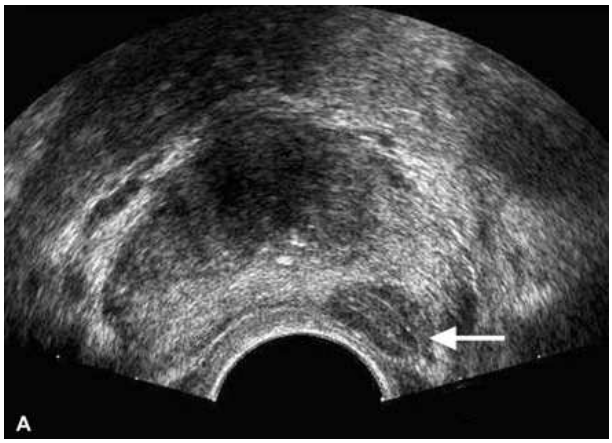

Figure 1.4: Transverse sonogram showing a hypoechoic nodule in the PZ (arrow) whose biopsy revealed a benign hyperplasia. Image courtesy Tang et al. [151]

from multicore sites in a systematic biopsy. If specimens from a suspicious lesion as visible on TRUS needs to sampled, then it is important to place the probe at the boundary of the lesion before firing the needle that ensures sampling accuracy. A hypoechoic lesion detectable with gray-scale TRUS is not necessarily a malignant lesion [157]. For instance, the chances of a hypoechoic lesion evaluated in TRUS guided biopsy being malignant is between 7% – 57% [21]. This results in multiple negative biopsies and thereby increases the number of re-biopsies required. Figure 1.4 shows hypoechoic benign hyperplasia in the peripheral zone of the prostate.

1.4 Magnetic Resonance Imaging (MRI)

The magnetic resonance imaging of the prostate is usually done in a 1.5 T *(Tesla)* whole-body scanner using a pelvic phased-array coil combined with an inflatable balloon-covered surface coil placed inside the rectum. The endorectal coil allows better visualization of the prostate zonal anatomy and accurate delineation of tumor, estimation of tumor volume and its extent [132]. Prostate MRI can also be done in a 3.0 T whole-body scanner using a torso phased-array coil without the endorectal coil. However it has been demonstrated by Beyersdorff et al. [18] that both 1.5 and 3.0 T MRI have the accuracy of 73% in local staging of cancer and that the image quality and tumor delineation are significantly better with 1.5 T pelvic coil

(a) (b)

Figure 1.5: MRI of the prostate. (a) T1-weighted MRI scan of the pelvis shows an enlarged left obturator node (arrow) proven to be cancer by biopsy, (b) endorectal, axial, T2-weighted MRI scan in a patient with a right-sided prostate cancer. Low signal intensity is demonstrated in the right peripheral zone (arrow). Copyright ©1994-2012 by WebMD LLC.

combined with the endorectal coil than only with the torso coil in 3.0 T scanner.

T1- and T2-weighted spin-echo MRI of the prostate are required to evaluate PCa. Thin axial or coronal images are acquired that are helpful for tumor localization and assessment of the extracapsular or seminal vesicle invasion of PCa [30]. The prostate gland is seen with intermediate signal intensity in T1-weighted images and therefore the neither the prostate zonal anatomy nor the intraprostatic pathology can be fully appreciated. However, on T2-weighted images the peripheral zone is of high signal intensity and is surrounded by a thin rim of low signal intensity that represents the capsule of the gland (see Figure 1.5). The central and transition zones are both of lower T2 signal intensities than the peripheral zone. The transition zone increases in size with increase in patient ages, thereby compressing the peripheral zone that increases the T2 signal intensity of the peripheral zone. PCa is characterized by low T2 signal intensity in the normally high signal intensity peripheral zone. However, certain benign conditions like prostatitis, intra-prostatic hemorrhage and scarring may also have similar appearances therefore, only T2-weighted MRI has a

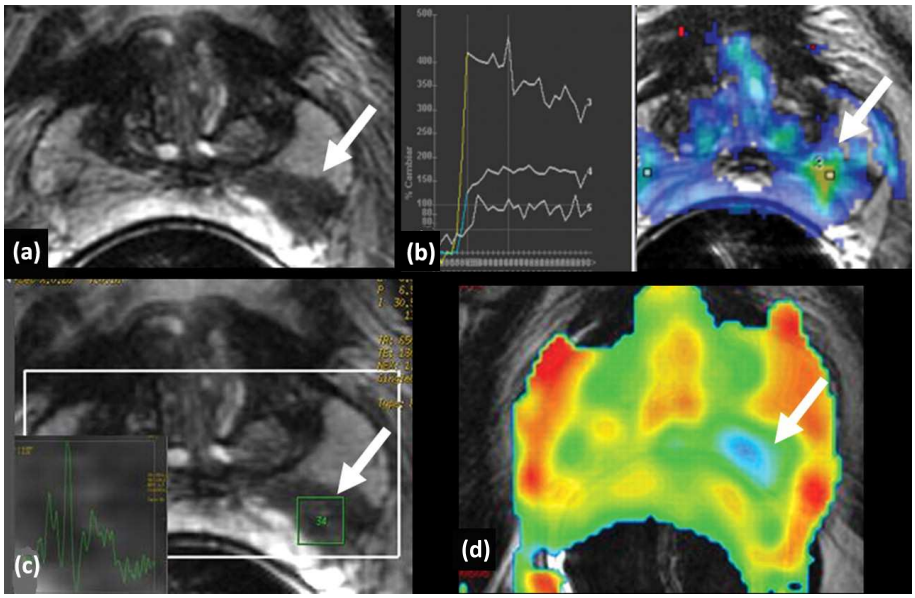

Figure 1.6: Multiparametric MRI. (a) Axial T2-weighted scan shows low signal intensity nodular lesion (arrow) within left peripheral zone, suspicious PCa, (b) DCE-MRI images shows early wash-in and wash-out curves from region of interest of lesion (arrow) suspicious for cancer, (c) MRS image shows normal metabolic curve within voxel from lesion (arrow), and (d) apparent diffusion coefficient map from DWI shows restricted diffusion from lesion (arrow), suspicious for malignant tumor. Biopsy was positive for prostate cancer within the peripheral zone. Image courtesy Vilanova et al. [158]

low specificity ranging from 54% – 82% and a widely varied sensitivity of 46% – 92% in detecting PCa [89, 51, 163]. MRI can determine the physiological properties of the tissue through different imaging techniques such as the diffusion-weighted MRI (DWI), which measures the diffusion of water molecules in the tissue. PCa in DWI is identified by lower diffusion due to increased cellular density of PCa tissues. Similarly, dynamic contrast-enhanced MRI (DCE-MRI) measures the microvascular properties of tissue and therefore, PCa having abundant microvasculature, the tumors show an early enhancement and wash-out of signal intensities. Finally, magnetic resonance spectroscopic imaging (MRS) can be used to measure metabolite levels in the tissue particularly choline, citrate, creatine, and various polyamines. PCa usually shows an increased concentration of choline, a reduction of citrate and lower levels of polyamines while, creatine is usually unaffected [93].

Recently, the combination of different imaging modalities of MRI such as multiparametric scanning has improved the specificity and sensitivity in detection of PCa [90, 154, 70]. Vilanova et al. [158] demonstrated the accuracy of detecting PCa combining endorectal T2-weighted MRI with functional imaging of DWI, MRS and DCE-MRI and PSA ratio. The method showed an accuracy for all combinations of the imaging methods and PSA ratio within a range of 90.2% – 95.2%, sensitivity between 64.7%–88.2%, specificity between 89.9%–95.5%, a positive predictive value ranging from 83.0% – 92.3% and a negative predictive value between 82.7% – 93.1% to detect PCa. Figure 1.6 shows PCa in T2-weighted MRI, DCE-MRI, MRS and DWI.

1.5 Thesis Objectives

TRUS biopsy is currently the 'gold standard' for PCa detection that relies on random sampling of the prostate [121]. Sampling error is an inherent feature of a prostate biopsy procedure because only a small amount of tissue is used to evaluate the whole organ. Therefore, it is absolutely possible that certain areas of adenocarcinoma within the prostate may be missed during biopsy. Although each of the standard cores on average contains a similar amount of prostatic tissue, the areas of the prostate sampled differ significantly in size. This problem is further complicated by the fact that different areas of the prostate are known to vary in their propensity to harbor cancer. Furthermore, it is possible that certain areas of the prostate could be more difficult to access via biopsy needles introduced through the rectum. Therefore, a standard 12 core TRUS guided biopsy can detect PCa with an average sensitivity ranging between 39.8%–48%, an overall accuracy between 55.7%–64.2% and a negative predictive value ranging between 43%–62.8% [78]. Hence the recent trend is to sample from a greater number of cores during biopsies in order to increase the detection of PCa [100, 82, 138].

The isoechogenicity of PCa lesions and low probabilities of hypoechoic lesions being malignant in addition to the need of increasing the number of biopsy cores have driven the use of pre-biopsy MRI data to direct TRUS biopsies. The use of MRI has been shown to have greatly improved PCa detection in patients with prior negative biopsy and suspicion of harboring malignancy [34, 4, 128, 17]. Therefore, MRI may

serve as a triage test for men deemed to be at risk of PCa and may reduce the number of re-biopsies while at the same time provide more useful information for those who are sent for biopsy. Consequently, fusion of pre-biopsy MR images onto inter-operative TRUS images might increase the overall biopsy accuracy [75, 85, 142, 168].

The prostate of the same patient may exhibit some deformations under certain conditions. The inflation of the endorectal coil inside the rectum during the MRI procedure, full bladder, bowel or gas inside the rectum and altered patient positions between the TRUS and MRI procedures may deform the prostate [28]. In order to cope with these deformations, non-rigid (deformable) registration methods need to be applied for prostate multimodal registration [2, 11, 47, 31, 109, 112, 133, 167].

In this research we have explored the possibility of various deformable registration methods that may be applied to translate the pre-biopsy MRI information onto the TRUS images during prostate biopsy. More specifically, **the primary goal of this research is to propose a new deformable registration method that may be applied to register 2D TRUS and 2D MR images.** We have observed from a literature study that deformable methods that exist for prostate multimodal images do not provide satisfactory accuracies and most of the existing deformable registration methods are computationally expensive and our proposed method is not an exception to this trend. In this context, **our secondary goal is to search for a deformable registration method that can be applied during real-time interventions. Therefore, we propose a learning scheme where the deformation parameters learned from a training set of corresponding TRUS-MR images are modeled and a linear estimation of these models are applied to register a test set of TRUS-MR images.** This scheme ensures speed of computation without compromising much on the registration accuracies.

In the experiments carried out to validate this research, an electro-magnetic (EM) tracker was not attached with the TRUS biopsy probe. Therefore, the spatial location (z-coordinate) of the TRUS images with respect to the imaging system has not been available. However, for the TRUS-MRI fusion it is important to identify the pre-biopsy axial MR image slice that corresponds to the axial TRUS slice acquired during biopsy. Hence, **a sub-goal of this research is to automatically identify the axial MR slice from a set of slices in the pre-biopsy volume that closely corresponds to the TRUS slice, exploiting the image-based and**

shape-based similarity metrics.

1.6 Overview of the Thesis

The remaining of the thesis consists of 7 chapters in total. The 2^{nd} chapter deals with some preliminary concepts related to image registration i.e. the general registration methodology, the similarity measures used, the optimization techniques and the interpolation methods.

Chapter 3, provides with a literature review related to prostate registration which are mostly mutlimodal registration techniques. The registration methods are categorized into rigid and non-rigid methods, where the deformable methods are sub-categorized into radial-basis transformations, deformable model, biomechanical finite-element modeling and non-parametric methods like demons registration. The chapter provides a consensus on the efficient use of radial-basis transformations in prostate TRUS-MR registrations.

The study of the state-of-the art methods of prostate registration led us to investigate further on radial-basis transformations and Chapter 4 provides a detailed discussion on two commonly used spline-based transformations, the thin-plate splines and the B-splines. Additionally, the chapter provides a proposed variant of B-splines with NMI as similarity metric on quadrature local energy images and its comparison with the other methods presented.

Chapter 5 provides a discussion of a new diffeomorphic registration of prostate multimodal images proposed in this thesis. The chapter includes a discussion of the proposed point correspondence method and the diffeomorphism based on a set of non-linear equations. The chapter provides extensive details on the various experiments performed to validate the proposed method.

The diffeomorphic method in Chapter 5 being computationally expensive, an offline learning of deformation parameters is proposed in Chapter 6. The method involved offline spectral clustering of deformation parameters and online linear estimation of the obtained deformation clusters to achieve fast multimodal registration.

Chapter 7 provides a discussion of the method to achieve the sub-goal of our research as mentioned in Section 1.5. This chapter provides the discussion of a

new method that identifies the axial MR slice from a pre-acquired volume that closely corresponds to the axial TRUS slice during prostate biopsy. Finally, Chapter 8 provides some general conclusions on the different proposals of our thesis and highlights some of the avenues of future research.

Chapter 2

Preliminaries

The primary objective of the thesis being image registration, this chapter provides a basic overview of an image registration framework and its components. The surveys of Maintz and Viergerver [103] and Zitová and Flusser [174] provide excellent overviews and categorizations of general image registration techniques and those applied to register medical images. Much of the contents presented in this chapter follow the surveys. However, we limit our discussions in the thesis to the registration of 2D multimodal images and affine and non-rigid geometric transformations.

2.1 Image Registration: An Overview

Registration is a procedure of geometrical alignment of one image (moving) into another image (fixed) of the same scene taken at different times and from different viewpoints so that they match each other as closely as possible. The procedure involves a geometric transformation that includes matching of homologous points or image intensities on the images by trying to maximize the similarity between such points or the intensities while estimating the transformation parameters.

A typical image registration algorithm consists of four coupled components: an *alignment measure* (also known as *similarity measure*) that quantifies the quality of alignment; a class of admissible *geometric transformations* that can be applied to the image(s), i.e., employed to spatially warp the image(s); an *optimizer* that seeks the transformation that maximizes the similarity as quantified by the alignment

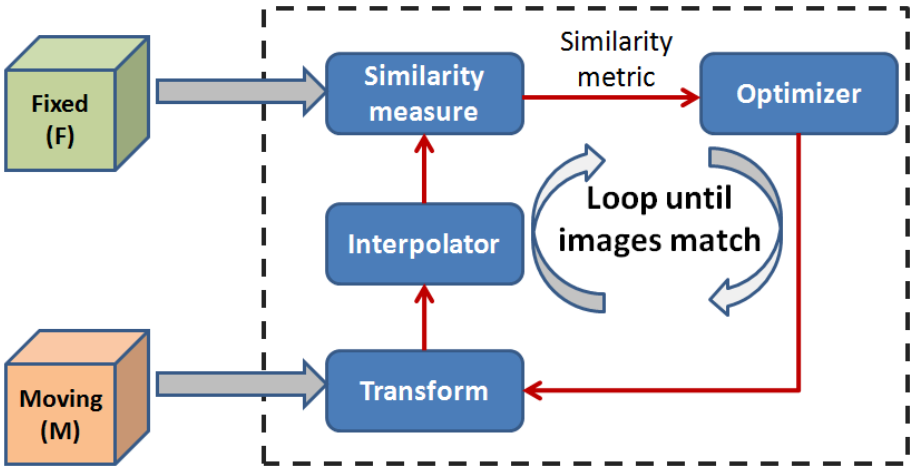

Figure 2.1: A schema of a typical image registration algorithm.

measure; and an *interpolator* that interpolates intensities at non-grid locations of the transformed moving image. Figure 2.1 shows a typical image registration framework.

2.2 The Theory of Image Registration

This section provides the formulation of the registration problem and mathematical interpretations of the different components described in Section 2.1.

2.2.1 Problem Definition

Let the fixed image F and the moving image M be defined in Ω, which is a finite subset of $\mathbb{R}^d$, where $d \in \mathbb{Z}^+$ denotes dimensionality. The relationship between the images F and M may be written as

$$F = \Phi(M), \tag{2.1}$$

where, $\Phi : \mathbb{R}^d \mapsto \mathbb{R}^d$ is the geometric transformation that models the misalignment that we want to recover. In this model $(F, \Phi(M))$ is a (optimally) registered pair of images. The goal of the algorithm is to estimate Φ, by maximizing an alignment measure (or, minimizing a misalignment measure).

2.2.2 Alignment Measure

Let us consider F, M and Φ be random variables. F and M follow a uniform distribution and Φ can be uniformly distributed over a set of admissible rigid-body transformations. In a maximum likelihood framework, a registration problem can be framed as

$$\arg\max_{\Phi} p(F, M|\Phi) \tag{2.2}$$

In order to compute Equation (2.2), we need to make certain modeling assumptions. For example, let us consider a mono-modal case, where the mapping between the images may be considered as an identity function. Then the log-likelihood function of Equation (2.2) can be shown to be proportional to the sum-of-squared differences (SSD) [124, 152] as in Equation (2.3).

$$\log p(F, M|\Phi) \propto -\sum_{f,m\in\Omega} (F(f) - \Phi(M(m)))^2 \tag{2.3}$$

where f and m are the pixel intensities on images F and $\Phi(M)$ respectively. The SSD of Equation (2.3) can also be extended for a homologous pair of extrinsic fiducials [111, 27, 110, 155, 60, 52, 162] or intrinsic anatomical landmarks [85, 120] placed on the fixed and the moving images.

Another common alignment measure is the Cross Correlation (CC) between the pixel intensities of the fixed and the moving images [130]. This is related with the well-known Pearson's correlation (r) where a linear relationship is assumed to exist between the pixel intensities of the fixed and the moving images.

$$\mathrm{CC} = r(F, \Phi(M)) = \frac{\sum_{f,m\in\Omega} (F(f) - \overline{F}(f))(\Phi(M(m)) - \Phi(\overline{M}(m)))}{\sqrt{\sum_{f\in\Omega} (F(f) - \overline{F}(f))^2}\sqrt{\sum_{m\in\Omega} (\Phi(M(m)) - \Phi(\overline{M}(m)))^2}}, \tag{2.4}$$

where, $\overline{F}(f)$ and $\overline{M}(m)$ are the average intensities of the fixed and the moving images respectively.

A commonly used information theoretic measure used for image alignment is the Mutual Information (MI) that measures the mutual dependence between the

images F and M [166, 149], i.e. if the images are mutually dependent, knowing F should provide enough information about M. MI is defined in terms of the joint and marginal probability density functions (pdf's) of the fixed and the moving images derived from their 2D-normalized joint intensity histograms [35] as

$$\mathrm{MI}(F, \Phi(M)) = \sum_{f \in \Omega} \sum_{m \in \Omega} p(f, m) \log_2 \frac{p(f, m)}{p(f)p(m)}, \tag{2.5}$$

where $p(f, m)$ is the joint probability of the fixed and the moving images and $p(f)$, $p(m)$ are the respective marginal probabilities.

A normalized version of MI is sometimes used for image alignment that is represented as the *symmetric uncertainty* between the fixed and the moving images [131] as

$$\mathrm{NMI}(F, \Phi(M)) = 2\frac{\mathrm{MI}(F, \Phi(M)}{H(F) + H(M)}, \tag{2.6}$$

where $H(F)$ and $H(M)$ are the marginal entropies of the fixed and moving images respectively.

$$\begin{aligned} H(F) &= -\sum_{f \in \Omega} p(f) \log_2 p(f) \\ H(M) &= -\sum_{m \in \Omega} p(m) \log_2 p(m) \end{aligned} \tag{2.7}$$

However, Studholme et al. [149] defined the NMI as

$$\mathrm{NMI}(F, \Phi(M)) = \frac{H(F) + H(M)}{H(F, \Phi(M))}, \tag{2.8}$$

where $H(F, \Phi(M))$ is the joint entropy of the fixed and the transformed moving images,

$$H(F, \Phi(M)) = -\sum_{f,m \in \Omega} p(f, m) \log_2 p(f, m). \tag{2.9}$$

Here, any change in uncertainty of the image values and therefore, the marginal entropies, will not result in a change in the alignment measure. Maximization of

NMI seeks a transformation where the joint entropy is minimized with respect to the marginal entropies.

2.2.3 Geometric Transformations

Different transformation models are utilized for various registration applications. In general, there are two approaches to define a geometric transformation: using parametric models, and in a nonparametric fashion using a dense deformation field. The first approach employs a small number of parameters to define the warp, whereas the latter method defines a deformation or motion vector at each pixel location.

For the sake of compactness let us assume a 2D space where $\mathbf{x} = (x, y) \in (R)^2$ and $\mathbf{x}' = \Phi(\mathbf{x})$. In this thesis we will concentrate on two basic parametric transformation models:

- **Affine:** In 2D, it is parameterized by six parameters $(a_1, a_2, a_3, a_4, a_5, a_6)$:

$$\begin{aligned} x' &= a_1 + a_2 x + a_3 y \\ y' &= a_4 + a_5 x + a_6 y \end{aligned} \tag{2.10}$$

  which can map a parallelogram onto a square. This model is defined by three non-collinear corresponding points that preserves straight lines and straight line parallelism. Rigid-body (rotation and translation), reflective-similarity (rotation, translation and global scale) and affine (rotation, translation, scale and shear) are the special cases.

- **Radial-basis:** This method provides a group of global transformations that can handle local distortions. In general, they can be expressed as:

$$\begin{aligned} x' &= a_1 + a_2 x + a_3 y + \sum_i c_i g(\|\mathbf{x} - p_i\|) \\ y' &= a_4 + a_5 x + a_6 y + \sum_i c_i g(\|\mathbf{x} - p_i\|), \end{aligned} \tag{2.11}$$

where $\mathbf{x} = (x, y)$, p_is are called the control points and $g(.)$ is the radial basis function. Popular choices for $g(.)$ are the thin-plate spline, where $g(r) = r^2 \log r^2$ [23], and

B-splines [137] where the basis functions are Bernstein's polynomials discussed in details in Chapter 4.

The advantage of parameterized techniques is that the dimensionality of the problem is relatively low and thus robust optimization is possible.

In a nonparametric approach each image pixel is transformed independently. One popular technique to impose some regularization on this formulation employs a global objective function that consists of two terms: the alignment measure and an external regularization term that reflects our expectations by penalizing unlikely transformations as in the demons [153]. Other methods employ modeling the transformation under the principles of linear elasticity, thereby yielding the deformation vectors for the triangular or tetrahedral mesh nodes used to model the image/volume e.g. biomechanical modeling [69]. Some methods employ a Bayesian approach with a prior distribution model, e.g. Brownian warps [119]. An alternative strategy is an iterative scheme where a 'rough' warp field obtained from the gradient of the similarity measure is projected onto a known function space. This projection is done by spatial smoothing [122] and has yielded fast nonrigid registration algorithms [39].

2.2.4 Optimization

Registration is merely an optimization problem that finds the optimum transformation parameters maximizing the alignment measure. Some methods that deal with simple transformation spaces (e.g. translation only) and simple alignment measures (e.g. SSD) can be easily solved. Most methods, on the other hand, do not enjoy a well-behaved, low dimensional objective function. Typically, registration algorithms attempt to solve the optimization using an iterative strategy. A detailed survey is available in [102]. Popular choices of optimizers are gradient-descent and its variants [159], Powell's method [127], Downhill simplex method [115] and *Levenberg-Marquardt* optimization [104]. The similarity measure gradient (with respect to transformation parameters) is commonly used to speed up this search.

2.2.5 Interpolation

The purpose of image registration (or matching) is to spatially align two or more single modality images taken at different times or several images acquired by multiple

imaging modalities. In the registration process it is often required to estimate the gray value at a point which does not lie on the transformed image grid. A gray value for such a non-grid point can be found by interpolation of grid values in the vicinity of the point. The type of interpolation is dependent on the geometric transformation used for the registration. The commonly used interpolation methods are bilinear, nearest-neighbor, bicubic [87], spline and inverse-distance weighting [141] method.

2.3 Evaluation of Image Registration

The accuracy of a registration method is evaluated using some standardized measures. The registration accuracies that measure global overlap are evaluated in terms of Dice Similarity Coefficient (DSC) ([43]) and 95% Hausdorff Distance (HD) ([76]). Local registration accuracies of anatomical structures inside the prostate gland are measured by Target Registration Error (TRE) and Target Localization Error (TLE) ([106], [105]).

DSC is a measure of overlap of the same foreground labels (E) between the transformed moving image ($M(E)$) and the fixed image ($F(E)$) and is given by

$$\mathrm{DSC} = \frac{2(M(E) \cap F(E))}{M(E) + F(E)}. \tag{2.12}$$

This means that a high DSC ($> 90\%$) signifies a good overlap between the prostate regions after registration.

Given a finite set of points $A = \{a_1, \ldots, a_p\}$ and $B = \{b_1, \ldots, b_q\}$, the Hausdorff distance between the point sets is defined by

$$HD(A, B) = \max(h(A, B), h(B, A)) \tag{2.13}$$

where

$$h(A, B) = \max_{a \in A}(\min_{b \in B} \|a - b\|) \tag{2.14}$$

The HD measure plays a significant role in identifying the similarity between the deformed moving image contour and the fixed image contour. A low value of HD signifies good contour registration accuracy. Therefore, even if a DSC measure signifies good region overlap, the HD measure may not signify a good contour registration.

A target is an anatomical landmark in the patient's body and is normally the centroid of a lesion, tumor, gland, etc. that is not used to compute the transformation of the moving image to the fixed image. TRE is the root mean square distance of such homologous targets tp_i and tq_i, $i = 1, 2, \cdots, N$ on the moving and the fixed images respectively and is given by

$$\text{TRE} = \frac{1}{N}\sqrt{\sum_{i=1}^{N}(\Phi(tp_i) - tq_i)^2} \tag{2.15}$$

where, $\Phi(.)$ is the transformation of the moving image.

The targets used in our experiments in the following chapters are primarily the centroids of lesions and tumors in the central gland, the prostatic urethra, sometimes the centroids of tumors in the peripheral region and the centroid of the central gland in few cases where lesions or other homologous structures are not visible in TRUS as in the corresponding MRI. One target for each pair of TRUS and MR image is used for the experiments. The repeatability error in the localization of the targets is given as the TLE computed from the centroids of manually selected regions from 5 independent trials by an experienced radiologist and an experienced urologist. A low TRE and a low TLE values signify good local registration accuracy. The clinical significance of TRE is the accuracy in identifying the anatomical targets in the deformed moving image. Actual TRE values may also incorporate TLE values, which is useful for clinical purposes to avoid under-estimation of the true TRE values.

2.4 Summary

In this chapter we provided the general framework of image registration and briefly described its components. The similarity measures that are primarily used for multimodal registration are defined and the notations are being consistently used in the remaining thesis. The registration methods have been broadly categorized as parametric and non-parametric based on the geometric transformations. The following chapter however follows a more specific categorization to organize the state-of-the-art prostate registration methods. The registration evaluation metrics and their

clinical significances have been discussed in this chapter and these metrics have been consistently used in the following chapters.

Chapter 3

A Literature Review

In this chapter we focus on registration methods that have been applied on prostate images or volumes for needle guided biopsy, radiation therapy, brachytherapy and surgery. This discussion also involves different prostate imaging modalities like US, MRI, MRS and CT. Some of the methods involved only rigid or affine transformations while some required additional deformable geometric transformations to cope with the prostate deformations exhibited in the multimodal images. Therefore we have made a broad categorization of the prostate registration methods into rigid/affine and deformable transformations.

3.1 Rigid/Affine Registration Applied to Prostate

Fusion of TRUS-MRI for guided needle biopsy of the prostate was reported by [85] where a set of axial pre-biopsy MRI slices were rigidly registered with the axial ultrasound (US) images acquired during a transrectal biopsy procedure. The registration was driven by the minimization of the corresponding fiducials manually chosen in both the US and MR images. The experiment was validated with two patient datasets with only qualitative results provided as the results of the registration process.

A validation and integration for 3D TRUS-guided robotic surgery for prostate brachytherapy was done by Wei et al. [164], where they performed a rigid registration of 3D point sets using a least-squares fitting algorithm [8]. The needle

placement accuracy of the robot was found to be 0.15 ± 0.06 mm when evaluated on two phantoms.

Fei et al. [53] registered 0.2 T live time-interventional magnetic resonance imaging (iMRI) slices to previously obtained high resolution 1.5 T MRI volume of prostate images for iMRI guided radio frequency thermal ablation of prostate cancer. They proposed a rigid registration (3 translations and 3 rotations) method with a multiresolution approach and automatic restarting of the algorithm to avoid local maxima. The similarity measures used for registration were MI and CC respectively for high and low resolution images and volumes. They observed smooth peak of CC while noisy edges and false peaks of MI at low resolution. In case of high resolution images and volumes, MI had a sharper peak than CC. On the first two low resolutions, CC was applied and MI on the higher resolutions. The algorithm automatically restarted on each resolution depending on a threshold value of absolute CC to avoid the false maxima of CC and MI. Downhill Simplex [115] or Powell's method [127] was applied for optimization. The registration was evaluated on simulated iMRI images from the 12 pair of MRI volumes, where one volume of each pair was used to simulate thick iMRI slices and register to the other volume. Evaluation of slice-volume registration was also done for 3 patients each having 3 MRI volumes and 50 actual iMRI slices in three standard orthogonal orientations. Voxel displacement error was used on a volume of interest around the prostate and compared against the volume-volume registration method [55] previously established by the authors. For the simulated images, the transverse slice had the least registration error in terms of average voxel displacement of (0.4 ± 0.2 mm) followed by the coronal (0.5 ± 0.2 mm) and the sagittal (2.6 ± 1.6 mm) orientation slices. The results further showed that the transverse slice centered on the prostate provided less registration error than the slice above the prostate that contained the deformable bladder and that below contained muscles and fat from the hip region that were also deformable. The actual iMRI data showed an average and standard deviation of 1.1 ± 0.7 mm for the transverse slice. The speed for the slice to volume registration was typically around 15 seconds. The authors claimed that the slice to volume registration method for transverse slices covering the prostate area was effective for image-guided therapy.

Steggerda et al. [147] proposed a method of rigid registration between TRUS and CT images of the prostate based on the position of the TRUS transducer present

in both modalities. The main idea of the authors was to evaluate the dose distribution after implantation of the radioactive iodine (I-125) seeds in the prostate. The CT provides better visualization of the seeds but poor contrast between the prostate and surrounding tissues and hence is not very promising for delineation of the prostate. However, the TRUS provides a better contrast between the prostate and the surrounding tissues but a poor visualization of the implant seeds. Therefore, a method was proposed to fuse the two modalities based on the visibility of the transducer probe. Thereafter, a fine-tuning of the registration was performed based on the seed visibility. The method involved three steps of registration. Firstly, the prostate phantom with the transducer probe inside was scanned in both TRUS and CT. A manual registration was performed to fuse these two modalities based on the visibility of the two needles and the transducer probe. The CT was resampled to be the same voxel size as the TRUS. Hence, a relation between the TRUS and the CT in the experimental phantom setup was established. However, the original patient TRUS and CT scan had different transducer positions in their own cartesian coordinates and so the second step was manual translation of a region of interest of the patient TRUS volume on the reference TRUS to align the transducer. This established a transformation between the patient TRUS and the reference (phantom) TRUS. The transformation between the reference TRUS and CT was already established. Therefore, what remained was the transformation between the reference CT and the patient CT based on the position of the transducer in both volumes. This was achieved by minimizing the voxel-wise RMS gray level differences of the two modalities. This total procedure provided a nearly approximate registration based on the transducer visibilities. This brought the implanted seeds also close to each other in the two modalities. However, again a gray-scale based minimization on the voxels was performed based on the visibility of the individual seeds for greater accuracy. This minimization employed the RMS difference of the gray level of voxels and the correlation ratio [134] between the voxel intensities. Downhill simplex method was used as optimization. The deviation error for the gray level seed registration against the transducer registration was measured in terms of translation along left-right, cranio-caudal and anterior-posterior directions for rotations along these axes respectively. The highest translational error was 0.5 mm along the left-right direction for a rotation of 1.4° along the same axis. Successful transducer gray

value-based registration was obtained in 21 cases out of a total of 23 cases. The authors stated that poor visualization of the seeds led to the failure of the two cases in the seed gray value-based registration.

Betrouni et al. [16] described a method of registration for effective conformal radiotherapy between tracked US images and a set of planning images or planning volume obtained from prior MR/CT examinations. The patient was setup in the operating room (OR) and MR/CT planning images were acquired. During the treatment the US images were captured and the 3D positions of the ultrasound were determined from epipolar geometry of the stereo video cameras capturing the movement of the US probe with 3 LEDs attached. A rigid registration method was applied based on a sequence of coordinate transformations between the US images and the OR and subsequently between the OR and the MR/CT planning images. Multiplanar reconstruction of the previously acquired MR/CT volume yielded a volume with the same orientation as the US. Prostate images were automatically segmented (using active contours) from the 3D US while the planning images were manually segmented. Consequently, both the US and planning image contours were represented with 3D points. The registration involved alignment of these sets of points using the ICP algorithm [15] with the translations of the sets of points about contour centroids. Target localization error (TLE) [111] was used to evaluate the registration accuracy. The TLE after registration of phantom balloons was 1.34 mm, while the highest TLE obtained among three volunteers was 1.48 mm. The registration time required was 13 to 20 secs.

Xu et al. [168] presented a method for real-time registration of US and MRI for guided prostate biopsies. Before the biopsy procedure, a 3D TRUS volume (reconstructed from 2D axial sweep of the prostate with a US probe attached to a electro-magnetic tracker) was manually registered with a 3D MRI volume acquired previously using rigid body transformation. Thereafter, an image based registration was employed for motion correction between the intra-operative 2D US frames and the reference US volume. A set of 2D frames within a short time frame were rigidly registered using a SSD based minimization with their respective 2D slices in the reference US volume. Finally, to further compensate for in-plane prostate motion, the current 2D US frame and its corresponding reconstructed frame from the reference US volume were registered using an image gradient and correlation coefficient

based registration. In patient studies for a new target the average time taken for biopsy was 101 ± 68 secs. The registration method was validated on phantoms with a registration accuracy of 2.4 ± 1.2 mm. A total of 20 patient studies showed an average overlap between MRI and the US images of $90\% \pm 7\%$ after motion compensation. The authors further validated their method with 101 patient cases [84] and the clinical results showed significant improvement of target visualization and of positive cancer detection rates during TRUS-guided biopsies.

Singh et al. [142] proposed a method of fusion-guided prostate biopsy from TRUS images. The 2D US was automatically converted into a 3D volume and this volume was registered with the pre-acquired MR volume manually with the help of a workstation attached to the operating room. Thereafter, the real-time 2D TRUS slices were registered with the 3D US volume using the method of Xu et al. [168]. The RMS value was found to be 3.3 ± 0.4 mm and the maximum mean distance was found to be 12.7 ± 1.2 mm. The registration process was completed in about 10 mins.

3.2 Deformable Registration Applied to Prostate

Although rigid registration has been frequently used for prostate multimodal fusion, the prostate of the same patient may undergo deformations under certain conditions. The inflation of the endorectal coil inside the rectum during MRI procedure, full bladder or bowel or gas inside the rectum and altered patient positions during the TRUS and MRI procedures may deform the prostate. In order to cope with these deformations, non-rigid registration methods need to be applied for prostate multimodal registration [109, 47, 133, 2, 88, 112, 11, 167, 72, 37, 139]. It may be noted that to initiate a deformable registration method an initial manual rigid or an automatic affine alignment is generally required. In this section we propose to sub-categorize the prostate deformable registration methods based on the employed geometric transformations.

3.2.1 Radial-basis Transformations

Spline-based transformations have been commonly used to register prostate images or volumes. TPS warping was also employed by Lu et al. [99] to generate a statistical volumetric model of the prostate for localization of prostate cancer. The registration error reported was too high to be considered for clinical procedures. The TRE for 7 cases was reported to be 295.66 pixels, but the physical dimensions were not provided. Similarly, prostate MR volumes were warped using TPS by Fei et al. [54] for brachytherapy and the registration was driven by the maximization of NMI. The accuracy of the registration showed that the lowest prostate centroid displacement for a volume pair out of 17 volume pairs was 0.6 mm.

Cheung and Krishnan [32] registered prostate MR volumes with and without the deformation of the endorectal coil using TPS with manually placed correspondences. Although the qualitative results were shown in terms of checkerboard overlap, the quantitative registration error was not reported. An improved system was proposed by Reynier et al. [133] for brachytherapy where manually segmented point clouds from MRI and TRUS were used to either rigidly or elastically align MRI with TRUS. The advantage of this system was the ability to model potential nonlinear deformation between the two modalities using octree splines [150]. The elastic registration results were validated using 11 patient cases with an average residual distance of 1.11 ± 0.54 mm for surface points on TRUS and MRI. Daanen et al. [38] used octree splines elastic registration to fuse TRUS and MRI prostate volumes for dosimetric planning of brachytherapy. The registration accuracy showed an average TRE of 2.07 ± 1.57 mm for 4 patients. Vishwanath et al. [160] registered prostate histological slices and MR slices to detect prostate cancer using B-splines. Since the aim was to detect cancer, quantitative values related to registration accuracy were not presented. A recent work by Xiao et al. [167] proposed to build a spatial disease atlas of the prostate using both B-splines and TPS. However, only qualitative results were presented.

Oguro et al. [120] registered pre- and intra-operative MR images for prostate brachytherapy using B-splines based deformation. The DSC value for the total gland was reported as 0.91 and the fiducial registration error was 2.3 ± 1.8 mm for 16 cases. The accuracies of surface-based and image-based registration methods to

register intra-session 3D TRUS-TRUS volumes were evaluated by Karnik et al. [86]. The surface-based registration involved a rigid registration using the ICP algorithm [15] and the non-rigid registration was based on TPS. The image-based registration employed the block-matching technique of Ourselin et al. [122] for rigid registration and the non-rigid deformation was defined by a 3D uniform grid of B-splines control points. A total of 16 patient datasets were used in the evaluation of the registration accuracies. The mean TRE for 60 fiducials for the TPS based registration was reported to be 2.09 ± 0.77 mm and for the B-splines based registration was found to be 1.50 ± 0.83 mm.

A recent work by Cool et al. [36] suggested a pre-biopsy 3D TRUS-MR fusion with a landmark-based rigid registration and a subsequent deformable registration using TPS. Thereafter an image-based registration using the methods of Chrisochoides et al. [33] and Ourselin et al. [122] was performed to rigidly register the intra-biopsy 3D TRUS and prebiopsy 3D TRUS (already co-registered with the pre-biopsy MR). The TRUS-TRUS rigid registration required 60 secs. The MRI-TRUS fusion study was carried out on 19 patients with a retrospective study on 5 patients showing a mean TRE of 4.3 ± 1.2 mm. Prostate cancer was identified in 42% (8/19) of all patients having suspicious lesions.

3.2.2 Registration based on Deformable Models

Narayanan et al. [112] proposed elastic registration between 3D TRUS and 3D MRI surfaces using adaptive focus deformable model [140] and elastic warping [41] for localization of prostate biopsy targets. The average Fiducial Registration Error (FRE) was shown to be 3.06 ± 1.41 mm for 6 and 12 bead phantoms.

Natarajan et al. [113] also proposed elastic warping of MR volume to match the TRUS volume acquired for targeted prostate biopsy. The fusion method involves rigid alignment of the two volumes using manually selected anatomical landmarks and thereafter, the methods of Narayanan et al. [112] and Karnik et al. [86] were used for surface deformation. The MR-fusion based targeted biopsy was performed on 47 patients where a 33% biopsy positivity rate was found versus a 7% positivity rate for systematic biopsy. The biopsy procedure took 15 minutes with an additional 5 minutes for the TRUS-MR fusion.

3.2.3 Registration based on Biomechanical Finite Element Modeling

Bharatha et al. (2001) proposed a method of rigid and non-rigid registration based on biomechanical finite element modeling to fuse intraoperative 0.5 T MR images with preoperative 1.5 T MR images. The evaluation of registration accuracy involved 10 patient cases that showed DSC values of 0.94 for the deformed total gland, 0.86 for the deformed central gland and 0.76 for the deformed peripheral zone. The total system worked in about 6 mins.

Alterovitz et al. (2004) proposed a deformable registration method for aligning MRS prostate images acquired with the help of endorectal coil with the MR images taken during treatment, based on the biomechanical model of the prostate tissue stiffness and force parameters. The input for the registration were manually segmented prostate and rectum images from probe-in MRS and probe-out MR. The deformations of the soft tissues were based on the finite element model and the nodal displacements of the tetrahedral volume mesh were obtained using the Gauss-Siedel method. The force and stiffness parameters were additionally optimized by Steepest Descent method with Armijo's rule [13] for line search. The evaluation of the registration for 5 patient datasets show a mean DSC for the central gland and the peripheral zone was obtained 95.6% ± 1.3%. The time taken to complete the registration was 27.8 ± 17.6 seconds. In a further work [3], the authors improved their DSC value to 97.5% when evaluated on 10 patient cases

Bois d'Aische et al. [40] proposed a non-rigid registration method based on finite element model and MI with an elastic constraint for fast registration of preoperative 1.5 T MR images and 0.5 T MR intra-operative images of the prostate for guided biopsy. The registration of the two datasets involved several stages. The datasets were first centered and scaled proportionately to match each other using an affine transformation. Then the surface of the prostate of both datasets was matched using conformal mapping [7]. The volumetric displacement field was estimated from the finite element model of both the datasets. A MI based non-rigid registration applied with a linear elastic energy constraint to smooth the nodes of the finite element model ensured registration of the internal structures properly. The optimization scheme used was based on Simultaneous Perturbation Stochastic

Optimization introduced by Spall [145]. The surface registration required around 90 secs and the final MI registration required 2 mins. The minimum distance between the landmarks after surface and MI registration was 0.3 mm. The largest distance of 3.8 mm went down to 2.5 mm after surface registration; and after MI registration the mean distance of 2.3 mm went down to 1.3 mm for a voxel size of $0.9 \times 0.9 \times 2.5$ mm.

Brock et al. [26] proposed a similar method as Bharatha et al. [19] to estimate the large deformations of the prostate due to the endorectal receiver coil during radiotherapy. A finite element model based elastic registration with different material properties was used to predict the prostate deformations due to the endorectal balloon inflated from 0cc to 100 cc. The registration time was around 7.3 mins. Gold seed markers were used to estimate the displacements that showed an average residual error for all three seeds of 8 patients as 0.21 cm.

Hu et al. [74, 75] proposed a model-to-image registration method to fuse a patient-specific biomechanically simulated finite element-based statistical motion model of the pre-acquired MR volume with the TRUS volume during biopsy procedure. The deformable registration involved maximizing the likelihood of a particular model shape given a voxel intensity-based feature that provided an estimate of surface normal vectors at the boundary of the gland. The registration was constrained by the statistical motion model subspace. This statistical motion model subspace accommodated the random TRUS probe induced deformations of the gland. The median RMS TRE for 8 patients with 100 MR-TRUS registration experiments for each patient was found to be 2.40 mm.

3.2.4 Other Non-parametric Registration Methods

Mizowaki et al. [109] proposed a simple method of registration of MRS volumes with the US/CT images with the assumption that any position inside the prostate did not change with respect to the prostate contours and the center of mass. Therefore, they accommodated the deformations of the prostate that resulted from the insertion of the endorectal coil in MRS. The deformations were assumed to be along the z-axis (craniocaudal) in direct proportion to the superior-inferior dimensions of the gland with respect to its center of mass. During the registration procedure, the center of

mass of both the volumes of MRS and US/CT were computed. The z-coordinates of both the volumes were adjusted proportionate to the superior and inferior aspects of the prostate. Similarly, the x- and y- coordinates of the volumes were adjusted maintaining the same aspect ratio in the left-right and anterior-posterior directions respectively. The experiment was carried out on a phantom for which two series of CT scans were acquired one without the endorectal balloon inflated and the other with the inflated endorectal balloon. The second series simulated the MRS. The average 3D positional displacement of seeds implanted into the prostate phantom was observed as 2.2 ± 1.2 mm. The maximum displacement was about 4.9 mm. Experiment with a patient showed that the absolute difference between the predicted and the measured seed displacement was about 2.4 ± 1.3 mm. The registration was performed in real-time and was accurate.

Chen et al. [31] proposed a non-rigid registration technique for image guided prostate radiotherapy. The registration process took place after the segmentation of planning CT and intraoperative cone beam CT images using level sets method of deformable models. Both the CT and cone beam CT volumes were resampled to equal voxel sizes. Sampling points on the surface of the level sets segmented volumes were used for the registration process. The deformation process was considered to be a combination of a global and local deformations. The global affine deformation for each sampling point in each iteration was obtained by minimizing the weighted least-squares distance. The local deformation of a sampling point was based on a modification of the demons forces acting on the sampling point [153]. A total of 15 datasets were used for validation and after registration the volumetric similarity was observed to be around 91% and the maximum registration time as 44 secs.

Khamene et al. [88] proposed a deformable registration technique based on a similarity measure that considers prior intensity distribution of the regions to be registered. The authors suggested dividing the fixed image into non-overlapping regions where the regions were indexed to be zero, if there existed, a corresponding pixel of the fixed image in the moving image that was to be transformed. Else, the regions were indexed with non-zero values. For regions indexed as zero, SSD was used as a similarity metric and for other regions a log-likelihood based energy constraint was used based on the prior probability of the intensity distributions derived from several training images. Finally, the deformation was formulated as the summation

of these similarity measures of the regions along with a global elastic regularization term of the deformation (displacement) field. Euler-Lagrange formulation was employed to compute the deformation field for each iteration. A total of 20 datasets of CT abdominal images from 10 patients were used for the validation of results and three different similarity metrics were used like SSD, MI and the proposed method. It was always observed that the proposed method outperformed the two former metrics in terms of the average surface distance measured for the prostate, bladder and rectum with values 2.4 mm, 3.0 mm and 4.1 mm respectively. The total registration process took less than 30 secs including a rigid initial alignment.

3.3 Summary

The state-of-the-art registration methods applied to prostate intramodal and multimodal images/volumes have been discussed in this chapter. A broad classification into rigid and non-rigid registration methods has been made to organize the methods available in the literature. While the rigid registration methods are strictly parametric as described in the previous chapter, the deformable registration methods comprise of both parametric and non-parametric approaches. The deformable registration methods are sub-categorized based on the underlying geometric transformations. It is observed from the previous sections that radial-basis functions and deformable models have been successfully used for TRUS-MR fusion. However, deformable models have been more suitable in case of 3D registration. Finite element model-based registration has been successfully used for same modality 3D volumes but with increased computation time that may not be suitable for real-time procedures. Certain other non-parametric approaches also showed promising registration accuracies, however, they were primarily used to register same modality prostate volumes.

Chapter 4

Registration based on Radial-Basis Transformations

In this chapter we focus on the details of the radial-basis functions that may be applied for deformable registration between TRUS and MR prostate images. Analyzing Chapter 3 we found that deformable registration is necessary to accommodate the inter-modal prostate deformations. We also found that spline-based deformations have been a popular choice and provided clinically significant TREs [156] required for 90% tumor hit-rate during biopsy. Therefore, we considered TPS [23] with automatic point-correspondences and B-splines with uniformly-spaced control points [137] for the deformable registration between pre-biopsy MR and inter-operative TRUS images.

4.1 Point correspondences

In the works of Lu et al. [99] and Fei et al. [53] manually chosen point correspondences were used to drive the TPS transformation. Establishing point correspondences can be a challenging task when the shapes of the prostate in the respective modalities have deformations. Hill et al. [73] proposed a method of polygon-based, automatic corresponding landmarks generation between two similar shapes and thereby, generated a mean point distribution model. Salient points on prostate contour were automatically identified using equal angle sampling by

Padilla-Castañeda and Arámbula-Cosío [114]. Yan et al. [169] used equally spaced salient points on prostate contour based on Euclidean distance to build a partial active shape model for segmentation. Zhan et al. [171, 172] used both the similarities between the prostate boundary landmarks and salient internal landmarks to drive the registration between histological and MR images. The boundary landmarks were identified as the nodes of the triangular mesh used to parameterize the prostate surface. The Euclidean distance between the attribute vectors of the boundary landmarks were used to find the landmark correspondences across the two modalities [140]. On the other hand, the internal landmarks were obtained from the Laplacians of scale-spaces (blob-detection). Finally, the similarity measure between the detected landmarks in terms of NMI was minimized to find the correspondences. In this thesis, we propose a novel approach to establish an optimal set of correspondence points automatically in the US and MR modalities to achieve deformable multimodal prostate registration employing TPS.

4.1.1 Automatic Point Correspondences (Geometric)

The 2D MR slice corresponding to the US slice is manually resliced from the MR volume and the prostates in both the images are automatically segmented using the method of Ghose et al. [66]. The US image is treated as the reference and the MR as the moving image. Principal Component Analysis (PCA) of the segmented contour in the reference US image provides the principal axes of the prostate. These axes are then projected on the center of gravity of the prostate MR image. The intersection points of the principal axes with the prostate boundaries for both the reference and moving images are identified automatically. All correspondence point generation methods described hereafter, are based on the principal axes of the prostate.

Our proposed method to establish point correspondences is based on triangulated approximation of the prostate quadrants. The triangulation method begins by traversing the intersections of the principal axes in a clockwise or anti-clockwise manner in each image. Triangles are generated by joining the adjacent intersections of the principal axes forming a quadrant and dropping a perpendicular from the midpoint of the line joining these intersections. The adjacent intersection points and the point of intersection of the perpendicular dropped on the prostate contour

comprise a triangular approximation of the prostate region in the quadrant. Likewise, other quadrants of the shape are processed for both the reference and moving images. Hence, new points formed by the triangulation method are generated on the shape contours for the first level (see Figure 4.1(b)). The points are reordered and further triangulations are made at subsequent resolutions, approximating smaller prostate regions close to the boundary. The process may be summarized as follows: Let p_i, where, $i = 1, ..., n$ and $n = 4$ for level $r = 0$, represent the four intersections of the principal axes with the prostate contour. With the final level $R = 3$, the algorithm is as follows:

1. Level $r = 0$.
2. Loop while $r <= R$.
3. $r = r + 1$.
4. Generate midpoint q_i between p_i and p_{i+1} as $(p_i + p_{i+1})/2$.
5. Find a point d_i on the contour between p_i and p_{i+1} such that $slope(p_i, p_{i+1}) \times slope(d_i, q_i) = -1$.
6. (p_i, d_i, p_{i+1}) comprise the triangulated region of the prostate between p_i and p_{i+1}.
7. Repeat steps 4-6 until $p_i = p_n$ and $p_{i+1} = p_1$.
8. If $r <= R$, then update $n = 2n$ and save $p_1, d_1, p_2, ..., p_{n-1}, d_{n-1}, p_n, d_n$ as new p_i with $i = 1, ..., n$ and repeat from Step 3. Else, end the loop.

The order of traversing the p_is should be the same for both the reference and moving images. Figure 4.1 shows the triangulation method for three subsequent levels/resolutions.

Instead of considering only the contour points for the deformable registration, certain points inside the prostate contour are also considered for a smooth deformation of the internal glandular structures of the prostate that are quite evident in MR images and sometimes partially visible in US images. The internal points are primarily the q_i's generated in resolution $r = 1$ and the prostate centroid c (see Figure

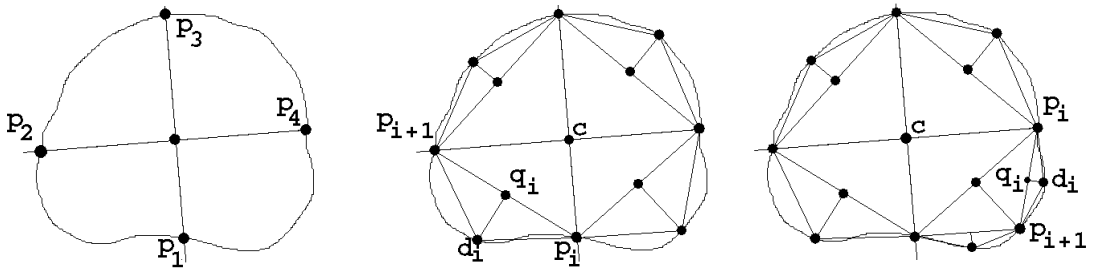

(a) Level 0 (b) Level 1 (c) Level 2, only shown for right-bottom quadrant

Figure 4.1: Method of generating correspondence points in different resolutions.

4.1(b)). However, we noticed that if the lower part of the prostate has higher concavity then either of these internal points (q_i) may fall outside the prostate boundary and therefore will hinder in obtaining a proper deformation field. Therefore, we further improved the choice of the internal points by considering the mid-points of the q_i's and c as z_i's. Figure 4.2 shows the points generated for the 1st level and the 37 final correspondences at the 3rd level on the fixed and moving prostate contour images respectively with the modified internal points.

Two methods of prostate contour sampling with equal angles and equal spaces are also implemented to compare the accuracies of our proposed correspondence generation method. These geometric sampling methods are intuitive where, in equal-angle sampling, the angles are equally spread inside each quadrant formed by the principal axes. In equal-space contour sampling, the points are also generated in each quadrant i.e. depending on the number of points falling in each quadrant, the points are sampled in equal intervals. Figure 4.3(a) and Figure 4.3(b) show the contour points obtained with equal-angle sampling and equal-space sampling approaches respectively. Figure 4.4 shows a case when non-uniformly spaced correspondences are generated with equal-angle sampling due to significant deformation between the reference and moving images. The plausible reason for the difference in sampling points between our method and other methods is that our method makes triangular approximations of prostate quadrants and smaller regions and moves towards the prostate boundary in a symmetric manner with the perpendicular bisector of the triangle as reference. While, other methods use the prostate centroid only as the reference lying far from the boundary and therefore the localization error of

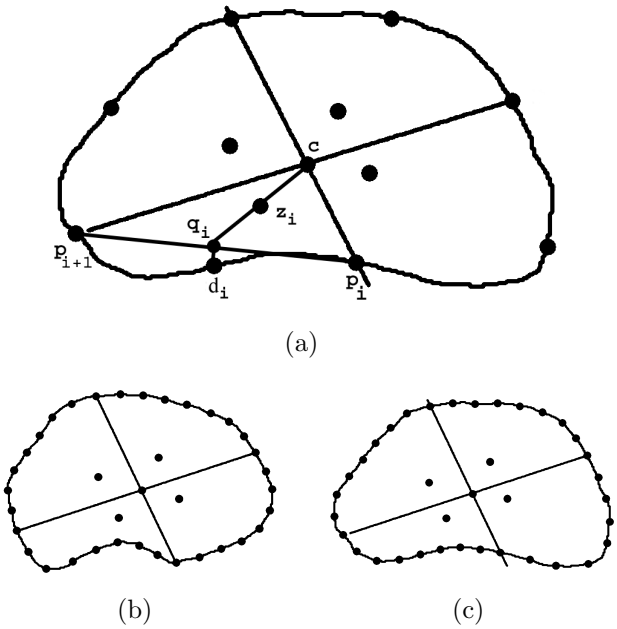

Figure 4.2: Point correspondences example with modified internal points. (a) Points generated for 1st level, (b) fixed image points at 3rd level and (c) moving image points at 3rd level.

correspondences increases.

4.2 Thin-plate Splines (TPS)

A thin-plate is conceived as a 2D thin metal plate which when tacked by a point or set of points produces bending of the surface in z-direction i.e. the surface

$$z(x, y) = -U(r) = -r^2 \log r^2 \tag{4.1}$$

where, r is the Euclidean distance of the Cartesian co-ordinate points on the surface from the tacked points. Here, U is a so-called fundamental solution of the biharmonic equation $\Delta^2 U = 0$, the equation for the shape of a thin steel plate lofted as a function $z(x, y)$ above the xy-plane (see Figure 4.5).

The thin-plate spline is a commonly used basis function in 2D-Euclidean space [22] to map the coordinates of a moving image into a fixed image, when a set of

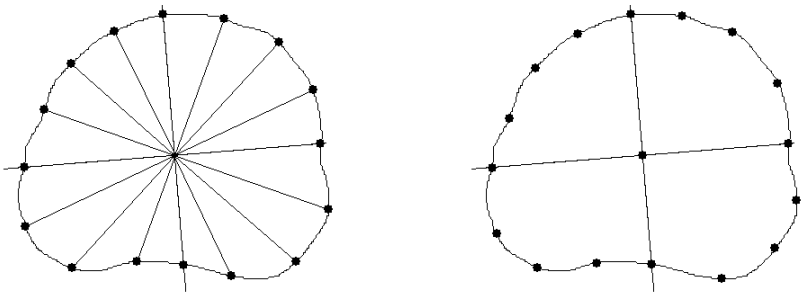

(a) Equal-angle sampling (b) Equal-space sampling

Figure 4.3: Geometric methods for correspondence points generation.

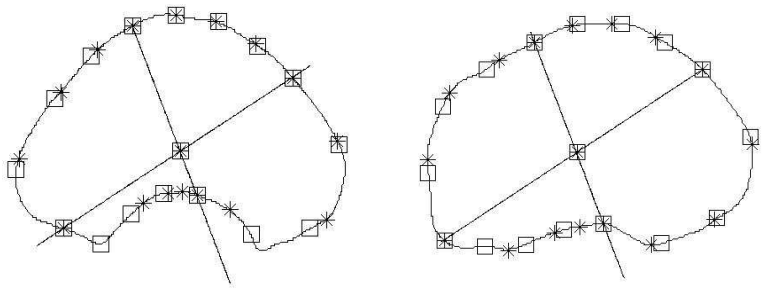

(a) Points generated in US (b) Points generated in MR

Figure 4.4: Points correspondences with different methods of contour sampling. The '*'s indicate points generated with equal-angle sampling and the squares indicate the points generated with our approach. Note that in the bottom-left quadrant, our method is able to get a uniform set correspondences on the prostate contours even in the presence of a significant deformation.

homologous correspondence points are established in both images. In its regularized form, the deformable TPS model includes the affine model as a special case. Correspondences are generated automatically on both the moving and fixed images as described in the previous section. Following is a brief algebraic description of the crux of the TPS model.

If $p_i = (x_i, y_i)$ and $q_i = (x_i', y_i')$, $i = 1, \ldots, n$ represent two sets of corresponding landmarks in the moving and fixed images respectively, then, the TPS interpolant $\Phi(x, y)$ minimizes the bending energy or the integral bending norm

$$I_\Phi = \int_{\mathbb{R}^2} \int \left(\left(\frac{\partial^2 \Phi}{\partial x^2} \right)^2 + 2 \left(\frac{\partial^2 \Phi}{\partial x \partial y} \right)^2 + \left(\frac{\partial^2 \Phi}{\partial y^2} \right)^2 \right) dx dy \tag{4.2}$$

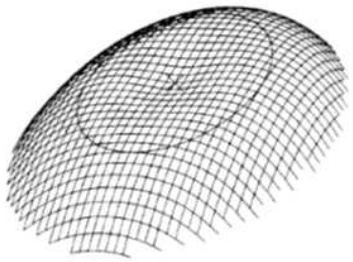

Figure 4.5: Fundamental solution of the biharmonic equation: a circular fragment of the surface $z(x,y) = -r^2 \log r^2$ viewed from above. The 'X' is at $(0,0,0)$; the remaining zeros of the function are on the circle of radius $r = 1$ drawn. Image courtesy Bookstein [22].

and the transformation function has the form

$$\Phi(x,y) = a_{u1} + a_{u2}x + a_{u3}y + \sum_{i=1}^{n} w_{iu} U(\|(x_i,y_i) - (x,y)\|), \tag{4.3}$$

where, $u = 1,2$, $U = r^2 \log r^2$ is the radial-basis function and w_{iu}'s are the weights assigned to each of the control point of the moving image. $\Phi(x,y)$ should have square integrable derivatives if

$$\sum_{i=1}^{n} w_{iu} = 0 \quad \text{and} \quad \sum_{i=1}^{n} w_{iu}x_i = \sum_{i=1}^{n} w_{iu}y_i = 0 \tag{4.4}$$

The boundary conditions in Equation (4.4) ensures that the thin-plate does not bend or rotate when acted upon by the loads of the control points.

Considering the interpolation conditions as $\Phi(x_i,y_i) = q_i$, let us rewrite $r_{i,j} = \|p_i - p_j\|$, $i,j = 1,\ldots,n$ as the distances between all the control points p_i and p_j. Then a linear system is obtained for the TPS as

$$\begin{bmatrix} K & P \\ P^T & O \end{bmatrix} \begin{bmatrix} W \\ A \end{bmatrix} = Q. \tag{4.5}$$

The matrices may be defined as

$$K = \begin{bmatrix} 0 & U(r_{12}) & \cdots & U(r_{1n}) \\ U(r_{21}) & 0 & \cdots & U(r_{2n}) \\ \cdots & \cdots & \cdots & \cdots \\ U(r_{n1}) & U(r_{n2}) & \cdots & 0 \end{bmatrix}, \quad n \times n;$$

$$P = \begin{bmatrix} 1 & x_1 & y_1 \\ 1 & x_2 & y_1 \\ \cdots & \cdots & \cdots \\ 1 & x_n & y_n \end{bmatrix}, \quad n \times 3; \quad L = \begin{bmatrix} K & P \\ P^T & O \end{bmatrix}, \quad (n+3) \times (n+3);$$

$$W = \begin{bmatrix} w_{11} & w_{12} \\ w_{21} & w_{22} \\ \vdots & \vdots \\ w_{n1} & w_{n2} \end{bmatrix}, \quad n \times 2; \quad A = \begin{bmatrix} a_{11} & a_{21} \\ a_{12} & a_{22} \\ a_{13} & a_{23} \end{bmatrix}, \quad 3 \times 2$$

and

$$Q = \begin{bmatrix} x_1' & x_2' & \cdots & x_n' & 0 & 0 & 0 \\ y_1' & y_2' & \cdots & y_n' & 0 & 0 & 0 \end{bmatrix}^T, \quad (n+3) \times 2,$$

where O is a 3×3 matrix of zeros, W and A are the matrices for the TPS weight parameters and the affine parameters respectively that need to be estimated. Let us define $G = [W; A]$. Therefore, the linear system of equations may be solved in the least-squares sense as

$$L.G = Q, \quad G = L^{-1}Q \tag{4.6}$$

The interpolation condition $\Phi(p_i) = q_i$ is based on the assumption that the control points on the moving image exactly maps onto the fixed image control points. However, in a real situation this is not always true as there may be some error in the localization of the point correspondences across the two images. Localization errors of the correspondence points may be considered by extending the interpolation to approximation and regularization of the TPS bending energy [135]. This is

accomplished by the minimization of

$$H_\Phi = \sum_{i=1}^{n} \frac{(q_i - \Phi(p_i))^2}{\sigma_i^2} + \lambda I_\Phi. \tag{4.7}$$

The covariance σ_i^2 is the sum of the covariances of the points p_i and q_i across both the fixed and moving images and λ is the regularization or smoothing term. The weighting of the correspondence localization error with the inverse of the variances ensures that if the variance is high i.e. if the measurements are uncertain, less penalty is given to the approximation error at this point. The relative weight between the approximation behavior and the smoothness of the transformation is determined by the parameter $\lambda > 0$. If λ is small we obtain a solution with good approximation behavior (in the limit of $\lambda \to 0$) we have an interpolating transformation. In the other case of a high value for λ we obtain a very smooth transformation, with little adaption to the local structure of the distortions determined by the sets of point correspondences. In the limit of $\lambda \to \infty$ we get a global transformation that has no smoothness energy I_Φ at all.

Finally, the quadratic approximation term of Equation (4.7) can be analytically introduced into the linear system of equations of Equation (4.5) as

$$\begin{bmatrix} K + n\lambda C^{-1} & P \\ P^T & O \end{bmatrix} \begin{bmatrix} W \\ A \end{bmatrix} = Q \tag{4.8}$$

where,

$$C^{-1} = \begin{pmatrix} \sigma_1^2 & & 0 \\ & \ddots & \\ 0 & & \sigma_n^2 \end{pmatrix}$$

Introducing the term $n\lambda C^{-1}$ yields a better conditioned linear system and a robust numerical solution. After obtaining the affine and TPS weight parameters, the moving image pixels are transformed using Φ as in Equation (4.3). An example TPS transformation is shown in Figure 4.6.

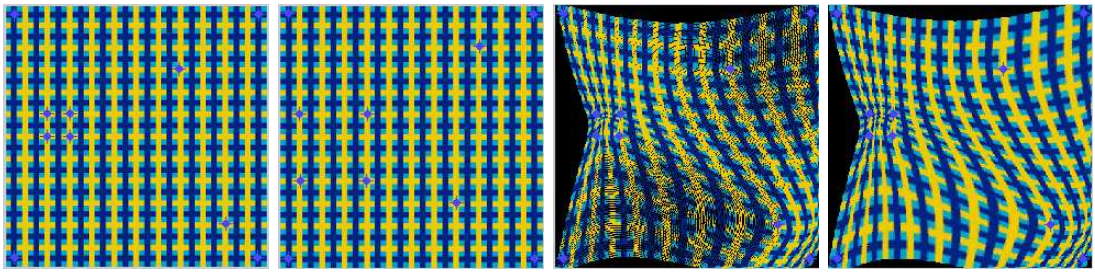

(a) (b) (c) (d)

Figure 4.6: An example TPS transformation with correspondences established across the fixed and the moving images in 'blue' dots. (a) Shows the fixed image with control points, (b) shows the moving image with the corresponding control points, (c) shows the TPS transformation without gray value interpolation, and (d) shows the interpolated TPS transformation using inverse weighted distance.

4.3 B-spline free-form deformations (FFDs)

The local deformation of an anatomical part may be described by FFDs based on B-splines. The basic idea of FFD's is to deform an object by manipulating an underlying mesh of control points [94, 95, 9]. The resulting deformation controls the shape of the 2D/3D object and produces a smooth and continuous C^2 transformation.

4.3.1 Deformation modeling with B-splines

Let us consider a domain of image as $\Omega = \{(x, y)|0 \leq x < X, 0 \leq y < Y\}$, Ψ as a mesh of $n_x \times n_y$ control points $\phi_{i,j}$ with uniform spacing δ. Then a spline-based FFD may be defined as a 2D tensor product of the familiar 1D cubic B-splines as

$$\mathbf{T}_{local}(x, y) = \sum_{l=0}^{3} \sum_{m=0}^{3} B_l(u) B_m(v) \phi_{i+l,j+m} \tag{4.9}$$

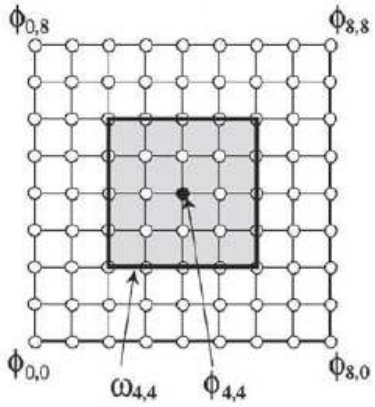

Figure 4.7: B-splines control point mesh. Control point $\phi_{i,j}$ affects points only inside its $4\delta \times 4\delta$ neighborhood domain $\omega_{i,j}$. Image courtesy Ino et al. [77].

where $i = \lfloor x/\delta \rfloor - 1, j = \lfloor y/\delta \rfloor - 1$, $u = x/\delta - \lfloor x/\delta \rfloor, v = y/\delta - \lfloor y/\delta \rfloor$ and B_l represents the lth basis function of the 1D cubic B-spline [129] given as

$$
\begin{aligned}
B_0(u) &= (1-u)^3/6 \\
B_1(u) &= (3u^3 - 6u^2 + 4)/6 \\
B_2(u) &= (-3u^3 + 3u^2 + 3u + 1)/6 \\
B_3(u) &= u^3/6.
\end{aligned}
$$

Unlike thin-plate splines [22], B-spline FFDs are locally controlled that makes them computationally efficient even for a large number of control points. It is evident from Equation (4.9) that the deformation at any point (x, y) is determined by its surrounding 4×4 neighborhood of control points. In other words, as shown in Figure. 4.7, each control point $\phi_{i,j}$ affects only its $4\delta \times 4\delta$ neighborhood domain which is a sub-domain of Ω.

In particular, the basis functions of cubic B-splines have a limited support, i.e., changing control point affects the transformation only in the local neighborhood of that control point. The control points Ψ act as parameters of the B-spline FFD and the degree of nonrigid deformation which can be modeled depends essentially on the resolution of the mesh of control points. A large spacing of control points allows modeling of global nonrigid deformations, while a small spacing of control points allows modeling of highly local nonrigid deformations. At the same time, the

resolution of the control point mesh defines the number of degrees of freedom and consequently, the computational complexity. The trade-off between model flexibility and computational complexity is mainly an empirical choice which is determined by the accuracy required to model the deformation of the object versus the increase in computing time. However, the best approach is to adopt a hierarchical multiresolution approach [95] in which the resolution of the control point mesh is increased, along with the image resolution in a coarse to fine fashion.

Let us consider $\Psi^1, \ldots, \Psi^L$ as a hierarchy of control point meshes at different resolutions. The spacing between the control points decreases from resolution Ψ^l to Ψ^{l+1}, i.e. the resolution of control points increases. It is assumed that the spacing of the control points in Ψ^{l+1} is half of those in Ψ^l and the new positions of the control points in Ψ^{l+1} can be computed directly from Ψ^l using the B-splines subdivision algorithm [57].

In order to constrain the spline-based FFD transformation to be smooth, a penalty term which regularizes the transformation may be introduced. The general form of such a penalty term has been described by Wahba [161]. In 2D, it is equivalent to the TPS integral bending norm defined in Equation (4.2) and is written as:

$$C_{smooth} = \int_0^X \int_0^Y \left(\left(\frac{\partial^2 \mathbf{T}}{\partial x^2} \right)^2 + 2 \left(\frac{\partial^2 \mathbf{T}}{\partial x \partial y} \right)^2 + \left(\frac{\partial^2 \mathbf{T}}{\partial y^2} \right)^2 \right) dx dy \tag{4.10}$$

where $\mathbf{T}$ is the total transformation that comprises of T_{global} i.e. an affine transformation and T_{local} a non-rigid transformation. It is to be noted that the regularization term is zero for any affine transformations and, therefore, penalizes only non-affine transformations. A step-by-step description of the FFD based deformation is given in Algorithm 1.

4.3.2 Similarity

The multimodal image alignment as proposed by Rueckert et al. [137] employing B-splines, is based on the maximizing the similarity of pixel intensities using the NMI as defined in Equation (2.8) of Chapter 2. It has been experimentally proved by Studholme et al. [149] that NMI is more robust in multimodal registration than

Algorithm 1 The non-rigid registration algorithm using B-splines.

calculate the optimal affine transformation parameters Θ by maximizing $C_{similarity}$.
initialize the control points Ψ.
repeat
  calculate the gradient vector of the cost function in Equation (4.11) with respect to the non-rigid transformation parameters Ψ: $\nabla C = \frac{\partial C(\Theta, \Psi^l}{\partial \Psi^l}$.
  while $\|\nabla C\| > \varepsilon$ **do**
    recalculate the control points $\Psi = \Psi + \mu \frac{\nabla C}{\|\nabla C\|}$.
    recalculate the gradient vector ∇C.
  end while
  increase the control point resolution to Ψ^{l+1} from Ψ^l.
  increase the image resolution.
until finest level of resolution is achieved.

MI proposed by Maes et al. [101]. In this chapter, we refer to the NMI image similarity as $C_{similarity}$.

4.3.3 Optimization

To find the optimal transformation, the cost function associated with the global transformation parameters Θ, as well as the local transformation parameters Ψ. The first term of the cost function represents the cost associated with the image similarity $C_{similarity}$, while the second term corresponds to the cost associated with the smoothness of the transformation C_{smooth} as in Equation (4.10). The cost function is defined as

$$C(\Theta, \Psi) = -C_{similarity}(F, \mathbf{T}(M)) + \lambda C_{smooth}. \tag{4.11}$$

The term λ is the regularization factor that makes the trade-off between alignment of the images and the smoothness of the transformation. It is to be noted that the regularization factor is of more importance at finer resolutions than coarser resolutions. A λ value equals to 0.01 provides a good trade-off between alignment and smoothness of the transformation as has been also mentioned in Section 4.2.

The optimization proceeds in two stages. During the first stage, the affine transformation parameters Θ are optimized, using an iterative multiresolution search

strategy [148]. This step is equivalent to maximizing the image similarity measure defined in $C_{similarity}$. The nonrigid transformation parameters Ψ are optimized as a function of the cost function in Equation (4.11) in the subsequent stage. A simple gradient descent optimization is employed at each stage and the algorithm stops if the magnitude of the gradient of the cost function $\|\nabla C\|$ is below a small value ε.

4.4 A variant of B-splines multimodality registration based on quadrature local energy

In this section we propose a new registration method involves B-spline deformations with NMI as the similarity measure computed from the texture images obtained from the amplitude responses of the directional quadrature filter pairs. The novelty of the proposal is to use directional quadrature filter pairs to transform both the MR and TRUS images into texture images obtained from the amplitude response of the filter pairs and use these transformed images for NMI computation. A similar method has been used by Jarc et al. [80] employing Law's texture to compute the MI in order to register far-infrared and visible spectrum gray-scale images. Francois et al. [58] used texture-based statistical measures to register carotid ultrasound volumes where the texture information was given by spatial Gabor filters. The advantage of computing NMI by this method is that the gray level differences in the TRUS and MR modalities are minimized, enhancing the inherent texture information of the prostate. A schematic diagram in Figure 4.8 shows the work flow of the proposed algorithm. The optimization is to minimize the cost function as in Equation (4.11) is solved using a quasi-Newton optimization method as Limited Memory Broyden-Fletcher-Glodfarb-Shanno (L-BFGS) algorithm [98].

4.4.1 Quadrature filters

Band-pass quadrature filters have been used in computer vision to access multi-scale image information like local-phase, energy, angular frequency etc. Central to the theory of quadrature filters in the analytical domain is the Hilbert transform [24].

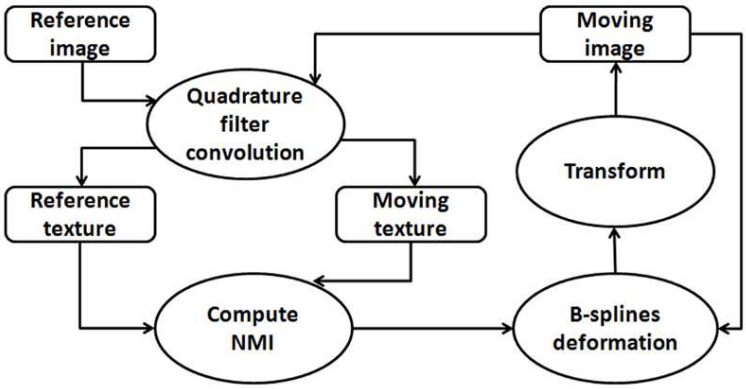

Figure 4.8: A schematic diagram of the proposed algorithm.

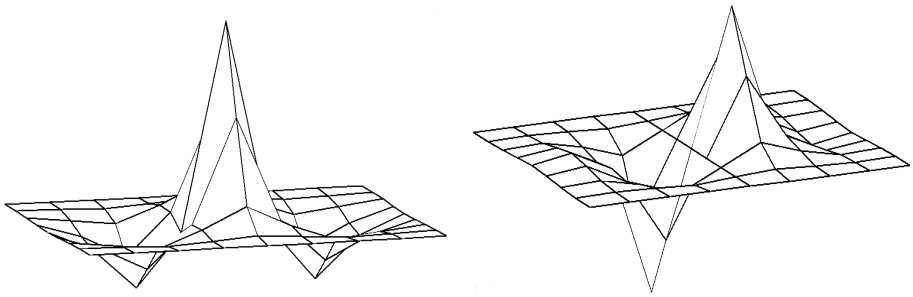

Figure 4.9: Even and Odd log-Gabor quadrature filter pairs in spatial domain.

The analytical signal of a 1D real signal $f(x)$ is given by

$$f_A(x) = f(x) - i f_{\mathcal{H}}(x); \tag{4.12}$$

where $i = \sqrt{-1}$ and $f_{\mathcal{H}}(x)$ is the Hilbert transform of $f(x)$ defined by:

$$\begin{aligned} f_{\mathcal{H}}(x) &= \frac{1}{\pi} \int_{-\infty}^{+\infty} \frac{f(\tau)}{\tau - x} d\tau \\ \Leftrightarrow F_{\mathcal{H}}(\omega) &= F(\omega).i \ \mathrm{sign}(\omega), \end{aligned} \tag{4.13}$$

where, $F(\omega)$ is the Fourier transform of $f(x)$ and

$$\mathrm{sign}(\omega) = \begin{cases} -1 & \omega < 0 \\ +1 & \omega \geq 0 \end{cases} \tag{4.14}$$

Therefore, the analytical signal in Fourier domain is obtained from Equation (4.12) and Equation (4.14) as

$$F_A(\omega) = F(\omega).\left[1 + \text{sign}(\omega)\right]. \tag{4.15}$$

To compute the local features of an image, localization of both space and frequency is required and is not possible directly from the resulting analytical signal since the Hilbert transform or analytical signal in Equation (4.12) and Equation (4.14) is defined over the entire signal. Therefore, an alternative approach is to compute the local phase or energy from the filtered version of the signal. The filter is an even, symmetric, zero-DC filter $f_e(x)$ and its odd counterpart is $f_o(x)$ which is the Hilbert transform of $f_e(x)$, hence they are in quadrature. Therefore, the analytical signal can be written as

$$\begin{aligned} \hat{f}_A(x) &= f_e(x) * f(x) - i\mathcal{H}(f_e(x) * f(x)) \\ &= (f_e(x) - i\mathcal{H}(f_e(x)) * f(x) \\ &= (f_e(x) - if_o(x)) * f(x), \end{aligned} \tag{4.16}$$

where $\mathcal{H}(.)$ is the Hilbert transform and '*' is the 1-D convolution operator.

In practice, an approximation of the local amplitude or energy ($\hat{A}(x)$) and phase ($\hat{\phi}(x)$) is obtained by using band-pass quadrature even and odd filter pair, $f_e(x)$ and $f_o(x)$ respectively, where,

$$\hat{A}(x) = \sqrt{\left[f_e(x) * f(x)\right]^2 + \left[f_o(x) * f(x)\right]^2} \tag{4.17}$$

$$\hat{\phi}(x) = \arctan\left\{f_e(x) * f(x) / f_o(x) * f(x)\right\}. \tag{4.18}$$

A generalization of quadrature filters in 2-D is provided as a set of filters tuned to a particular orientation and are therefore called directional quadrature filters [79].

The magnitude of the complex filter response with images gives the power portions of the texture process contained in different spectral bands [1]. Log-Gabor quadrature filters are used in this paper that are Gaussian functions on the logarithmic scale. The 1-D representation of a log-Gabor function in the frequency

domain is given by

$$G_l(\omega) = \exp\left(-\frac{\ln^2(\omega/\omega_0)}{2\ln^2(\kappa_\beta)}\right) \tag{4.19}$$

where ω_0 is the peak tuning frequency at $\pi/3$ and $0 < \kappa_\beta < 1$.

$$\kappa_\beta = \exp\left(-\frac{1}{4}\sqrt{2\ln(2)}\beta\right),$$

where β is the bandwidth fixed to 2 octaves. The peak tuning frequency and bandwidth are optimized values obtained from the MATLAB toolbox provided by Andersson and Knutsson [5]. Quadrature filters in directions $0°, 45°, 90°$ and $135°$ are used and the individual even and odd filter responses are added to provide the magnitude of the combined filter response. The even and odd filters tuned to $0°$ are shown in Figure 4.9. Figure 4.10 shows the texture energies of the fixed TRUS and the moving MR images when the 4 directional even-odd quadrature filter pairs are applied. It is evident that the gray level differences between the internal structures of the prostate are minimized in MR image as well as the shadow regions which have disappeared in the TRUS image.

4.5 Data and Analysis

The proposed method is evaluated for prostate mid-gland images of 20 patient datasets with average prostate volume of 56.7 ± 22.0 cm^3. The TRUS images were acquired with a 6.5MHz side-firing probe with SIEMENS Allegra and TOSHIBA Xario machines and the axial T2 fast relaxation fast spin echo MRI slices with slice thickness of 3 mm, repetition time of $3460-3860$ ms and echo time of $113.62-115.99$ ms were acquired with a GE Signa HDxt. The axial middle slices in TRUS are chosen for which the corresponding axial MR slices are identified by an expert. Ideally the axial MR slice corresponding and parallel to the axial TRUS slice should be obtained by rotating the MR volume in accordance with the rotational angle of the TRUS slice and then resampling the axial MR slice parallel to the axial TRUS slice under observation. However, we have not quantified the TRUS rotational angle in our current experimental process. The prostate is manually segmented from both the moving MR and fixed TRUS images. A NMI-based affine transformation

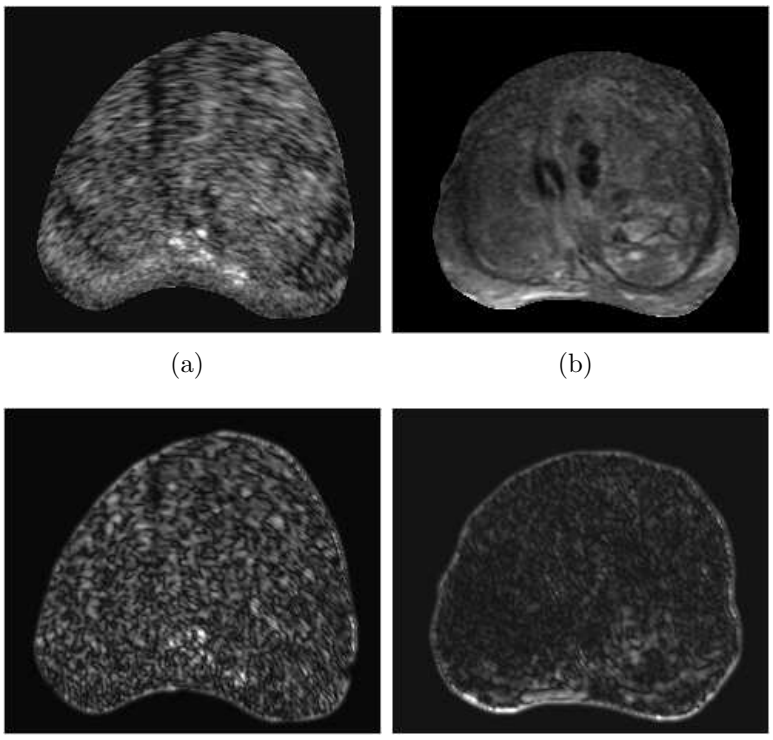

(a) (b)

(c) (d)

Figure 4.10: Application of quadrature filters on TRUS and MR images. (a) and (c) are the fixed TRUS image and its corresponding quadrature texture; and (b) and (d) are the moving MR image and its corresponding quadrature texture respectively.

between the TRUS and the MR images is followed by the free-form B-spline deformation. A uniform initial B-spline control grid with a spacing of 64×64 is placed on the moving image with an average image size of 256×256. Figure 4.11 shows the uniform B-spline control grids on the moving MR image of size 219×249 at the initial and final resolutions. The size of each image pixel is 0.2734×0.2734 mm. The B-splines deform at each resolution to maximize the NMI computed from texture images that are obtained from the magnitudes of quadrature filter responses.

We have compared the proposed method against two spline-based registration methods; 1) B-splines registration that maximizes the NMI computed from the raw intensities of the multimodal images [137], and 2) registration using TPS that uses contour-based automatic correspondences to solve the affine and TPS weight parameters [22, 108].

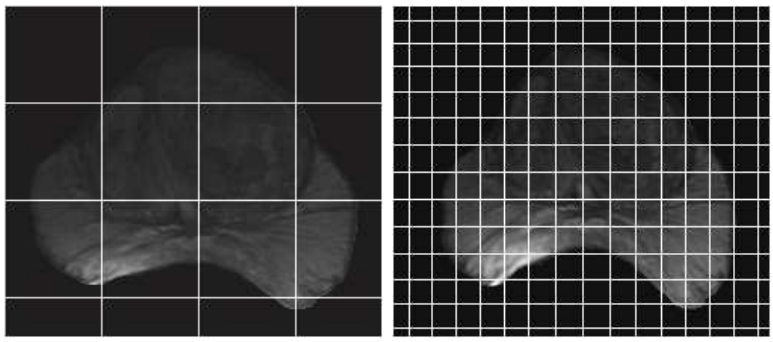

(a) (b)

Figure 4.11: B-splines control grid with 2 refinements over the initial placement on the moving MR image of size 219×249. (a) shows the initial placement of the B-spline grids with 64×64 pixel spacing on the moving MR image and (b) shows the final set of B-spline control grids on the transformed moving image.

4.6 Results and Discussions

The registration accuracies of our proposed method are evaluated in terms of DSC and 95% HD values for mid-gland images of 20 patients and TRE and TLE values for 18 patients i.e. only where homologous structures are visible both in TRUS and the transformed MR images. Table 4.1 shows the DSC, TRE, TLE and 95% HD values as obtained from the experiments for B-spline deformations with NMI computed from intensities [137] as explained in Section 4.3, our method for B-spline deformations with NMI computed from textures (Section 4.4) and TPS registration [22, 108] (Section 4.2). A statistically significant reduction with two-tailed t-test $p = 0.02$ is observed in the average TRE value for B-splines with NMI computed from texture when compared to B-splines with NMI computed from intensities with 2.64 ± 1.37 mm and 4.43 ± 2.77 mm respectively. Our proposed method shows an improvement of 1.18 times in TRE when compared with TPS registration with average TRE of 3.11 ± 2.18 mm. However, this improvement of average TRE over TPS is not statistically significant. The average TLE for all the methods are similar with 0.16 ± 0.11 mm, 0.12 ± 0.08 mm and 0.15 ± 0.12 mm for our method, B-splines with NMI from intensities and TPS registration respectively.

The DSC value is a global measure of region overlap and the average DSC values for our method of B-splines with NMI computed from texture, B-splines with NMI

Table 4.1: A comparison of registration accuracies of the B-spline registration with NMI computed from intensities, from texture and TPS registration. μ is the mean and σ is the standard deviation of the measures.

Patient#	**B-spline Registration**								**TPS Registration**			
	NMI from Intensities Rueckert et al. [137]				***NMI from Texture***				Bookstein [22]			
	DSC	TRE (mm)	TLE (mm)	HD (mm)	DSC	TRE (mm)	TLE (mm)	HD (mm)	DSC	TRE (mm)	TLE (mm)	HD (mm)
1	0.902	5.07	0.10	9.35	0.896	4.09	0.22	7.31	0.971	9.36	0.22	1.84
2	0.980	0.37	0.09	1.07	0.964	1.50	0.14	1.30	0.957	3.98	0.10	2.32
3	0.973	-	-	2.08	0.953	-	-	5.45	0.974	-	-	2.09
4	0.985	1.91	0.28	1.07	0.962	1.40	0.29	3.96	0.982	5.21	0.49	1.40
5	0.889	9.08	0.04	8.06	0.869	5.65	0.05	6.76	0.972	2.11	0.07	2.35
6	0.869	6.11	0.04	6.16	0.975	2.70	0.07	2.23	0.979	1.17	0.05	2.32
7	0.959	0.90	0.12	5.04	0.889	1.94	0.09	8.82	0.977	4.43	0.12	2.61
8	0.976	4.70	0.03	3.38	0.964	1.11	0.10	5.81	0.978	3.57	0.05	2.96
9	0.960	-	-	4.93	0.982	-	-	1.32	0.978	-	-	2.39
10	0.952	8.29	0.09	5.98	0.981	4.04	0.13	1.04	0.972	6.09	0.04	1.98
11	0.962	6.12	0.04	3.03	0.950	1.69	0.04	3.72	0.972	2.98	0.12	2.22
12	0.944	1.58	0.25	4.60	0.934	0.31	0.16	5.18	0.971	2.44	0.12	5.00
13	0.961	1.00	0.05	4.83	0.878	3.42	0.05	7.39	0.980	3.06	0.07	1.84
14	0.896	7.32	0.05	6.50	0.965	1.85	0.05	3.12	0.986	1.75	0.07	0.82
15	0.942	5.01	0.05	6.06	0.948	2.32	0.13	5.02	0.968	2.29	0.07	2.22
16	0.974	7.27	0.13	2.90	0.950	4.71	0.13	6.50	0.970	1.86	0.07	2.71
17	0.894	4.32	0.12	7.18	0.872	3.22	0.23	7.64	0.982	0.18	0.32	1.04
18	0.985	0.51	0.26	2.32	0.975	1.77	0.29	2.87	0.982	0.91	0.26	1.64
19	0.936	5.12	0.19	7.01	0.969	2.91	0.43	7.09	0.983	1.47	0.23	1.66
20	0.939	5.03	0.20	5.51	0.975	2.83	0.21	2.45	0.973	3.11	0.30	2.08
μ	**0.944**	**4.43**	**0.12**	**4.85**	**0.943**	**2.64**	**0.16**	**4.75**	**0.975**	**3.11**	**0.15**	**2.17**
σ	**0.036**	**2.77**	**0.08**	**2.30**	**0.039**	**1.37**	**0.11**	**2.40**	**0.007**	**2.18**	**0.12**	**0.85**

computed from intensities and TPS registration are 0.943 ± 0.039, 0.944 ± 0.036 and 0.975 ± 0.007 respectively. 95% HD provides the contour accuracy for which the average values of 4.75 ± 3.40 mm, 4.85 ± 2.30 mm and 2.17 ± 0.85 mm are obtained for our method of B-splines with NMI from texture, B-splines with NMI from intensties and TPS respectively. We observe that TPS registration based on control points placed over the contours always has higher average DSC and lower average HD values over the proposed B-splines registration with statistical significance (two-tailed t-test) of $p < 0.001$ and $p < 0.0001$ for DSC and 95% HD measures respectively.

TRE values of all patients are much lower with the proposed method when

compared to the B-spline method with NMI computed from intensities except for patients 2, 7, 13 and 18 where the dark shadows near the edges of the TRUS images are misinterpreted as the black background. Higher DSC values are obtained from the proposed method when compared to B-spline with NMI computed from intensities especially for patients 6, 9, 10, 14, 15, 19 and 20 and for patients 2, 9, 10 and 20 when compared to TPS.

Figure 4.12 shows the qualitative B-spline registration using NMI from raw intensities, using NMI from texture and the TPS registration in the form of checkerboards for 5 patients (patient 6, 8, 10, 11 and 13). As seen in Figure 4.12 for patients 6 (column 1) and 10 (column 3), the checkerboards (row 6) show good region overlaps that are also evident from Table 4.1 for the proposed method. TRE is a reliable measure of registration accuracy than region overlap measure specially when localization of biopsy site is involved. Therefore, in spite of the less satisfactory region overlaps in Figure 4.12 for the proposed method (row 6) with patients 8 (column 2) and 11 (column 4) when compared to other methods (rows 4 and 8), lower TRE values are obtained for the same patient cases with our proposed method as seen in Table 4.1. In Figure 4.12 we observe poor region overlaps for patients 11 and 13 in columns 4 and 5 respectively. There may be two reasons for the poor registration accuracy around the prostate contour, 1) acoustic shadows in TRUS images around the rectum do not provide any texture information and are considered homogeneous with the black background, and 2) part of the contour of the moving image may lie far from the respective fixed image contour. In both these cases, the control grids placed on the moving image around the contour consider a large part of the black background for the maximization of NMI with the corresponding TRUS (textured) region and therefore the maximization process fails to reach a global maximum. However, blurring of the prostate around the bladder or rectum would not affect the contour registration accuracy since blurred regions still may contain some texture. It is also observed that shadow artifacts and calcifications inside the prostate do not affect the contour registration accuracy. For instance, for patient 11 (row 1, column 4), the acoustic shadow region inside the prostate does not affect the overlap accuracy; however, the large part of the shadow on the lower-right contour region deteriorates the contour overlap accuracy.

The texture obtained from the magnitude of directional quadrature filter trans-

forms of an image measures the power portions of the image. The MR and TRUS images have varied gray-level intensities and contrasts. Therefore, transforming the MR and TRUS images as texture energy images homogenizes the intensity variations between them and reveals the underlying prostate architectural information that is common to both the modalities. Hence, the proposed method shows better registration accuracies in terms of TRE than traditional B-splines deformation with NMI from intensities. The proposed algorithm is validated only on TRUS-MR slices from the prostate mid-gland region and the performance of the same on the base and apex regions is yet to be validated.

The algorithms are implemented in MATLAB 2009b with a machine configuration of 1.66 MHz Core2Duo processor and 2 GB memory. The average time requirements of our method of B-splines with NMI computed from texture, B-splines with NMI computed from intensities and TPS registrations are 797.72 ± 202.59 secs, 147.25 ± 43.81 secs and 76.22 ± 29.79 secs respectively. The computation time includes the time for affine and nonrigid registrations for each of the methods. The obvious reason of B-splines with NMI computed from texture being computationally expensive is due to the use of 4 quadrature convolutions for each of the fixed and moving images at each resolution of B-splines deformations. The lowest time of 397 secs and the maximum time 1316 secs are recorded for the proposed method. However, quadrature convolution and registration of $256 \times 256 \times 256$ 3D volumes are achievable at 3.05 secs when programmed in GPU [50]. Therefore, parallelization of the convolutions and our algorithm implemented on GPU would ideally reduce the execution time to less than 3 secs which is closer to the clinical requirement.

4.7 Conclusions

In this chapter a new method to register TRUS and MR prostate 2D images have been presented that uses B-spline deformations with a novel method of computing the NMI. NMI as the similarity measure for the registration is computed from texture energy of the images obtained from the magnitude of the directional quadrature filter pair responses. Log-Gabor filters with narrow bandwidth have been used that allows to measure power portions of the signal representing texture energy in case of 2D TRUS and MR images. NMI computation involves reduction of the entropy

of the images. The entropy between TRUS and MR raw intensity images is typically more than the entropy of texture images due to variations in the gray-levels. Therefore, B-spline registration with NMI computed from texture images is more accurate than that with NMI computed from intensity images. The method is also consistent in terms of TRE that is evident from the high precision and low standard deviation of the average TRE value. We observed from the experiments that the average DSC and 95% HD values for TPS registration show smaller error compared to the proposed method and B-splines with NMI computed from intensities. This is due to the fact that the TPS registration in [22, 108] is based on control points primarily placed on prostate contour. This results in higher contour accuracy (related to both DSC and HD measures), while B-spline control points are uniformly spread over the prostate image. Since the final aim is accurate localization of biopsy samples and TRE provides a measure of registration accuracy for localized regions, TRE may be a more clinically relevant metric than DSC or other contour accuracy measures. In this respect our method of B-splines with NMI computed from texture shows statistically significant improvement over B-splines with NMI computed from intensitites; and 1.18 times improvement over TPS registration. However, if the clinical requirement is contour accuracy, TPS registration may be preferred over the B-splines registration.

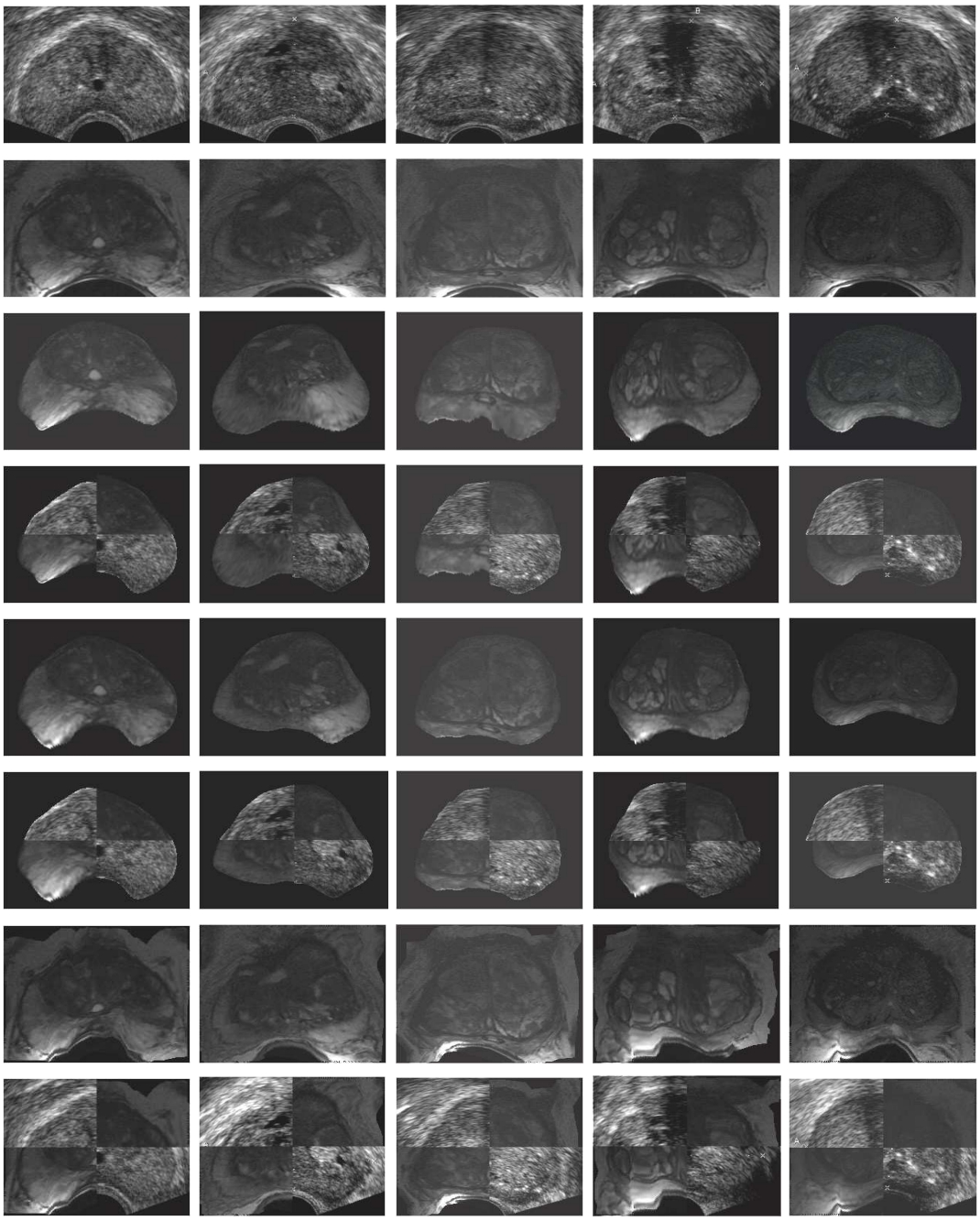

Figure 4.12: Qualitative B-spline registration using NMI from intensity images, NMI from texture images and TPS registration. Patients 6, 8, 10, 11 and 13 in columns. 1^{st} row shows the fixed TRUS slices, 2^{nd} row shows the moving MR slices, 3^{rd} – 4^{th} rows show the fused MR and the checkerboards for B-spline using NMI from intensity images, 5^{th} – 6^{th} rows show the fused MR and the checkerboards for B-spline using NMI from texture images and 7^{th} – 8^{th} rows show the fused MR and checkerboard for TPS registration.

Chapter 5

A Spline-based Non-linear Diffeomorphism for Prostate Registration

In this chapter, we present a novel method for non-rigid registration of transrectal ultrasound and magnetic resonance prostate images based on a non-linear regularized framework of point correspondences obtained from a statistical measure of shape-contexts. The segmented prostate shapes are represented by shape-contexts and the Bhattacharyya distance between the shape representations is used to find the point correspondences between the 2D fixed and moving images. The registration method involves parametric estimation of the non-linear diffeomorphism between the multimodal images and has its basis in solving a set of non-linear equations of thin-plate splines. The solution is obtained as the least-squares solution of an over-determined system of non-linear equations constructed by integrating a set of non-linear functions over the fixed and moving images. However, this may not result in clinically acceptable transformations of the anatomical targets. Therefore, the regularized bending energy of the thin-plate splines along with the localization error of established correspondences should be included in the system of equations.

5.1 Introduction

As observed in Chapter 3, spline-based deformations have been commonly used to register prostate images or volumes. The interpolating Thin-plate Splines (TPS) originally proposed by [23] that involves the establishment of a set of point correspondences on a pair of images. However, these sets of correspondences are prone to error in real applications and therefore [135] extended the bending energy of TPS to approximation and regularization by introducing the correspondence localization error. Nevertheless, all these methods ([23, 135]) are dependant on a set of point correspondences on the pair of images to be registered. Domokos et al. [116, 117, 44] proposed a class of non-rigid registration that does not require explicit point correspondences and instead registers binary images solving a set of non-linear equations.

In this work, we have improved the generic non-linear registration framework of [44] by establishing prostate-specific point correspondences and regularizing the overall deformation. The point correspondences under the influence of which the thin-plate bends are established on the prostate contours by a method based on matching the shape-context [14] representations of contour points using Bhattacharyya distance. The approximation and regularization of the bending energy of the thin-plate splines are added to the set of non-linear TPS equations and are jointly minimized for a solution.

The primary contributions of this chapter may be summarized as follows:

1. The use of shape-context and Bhattacharyya distance to establish point correspondences on both fixed and moving images,

2. the use of a prostate-specific TPS transformation in the non-linear framework of [44],

3. and constraining the non-linear diffeomorphism by adding the approximation error and regularization of the TPS bending energy.

Analyzing the state-of-the art methods in Chapter 3 that exist for prostate TRUS-MR image registration, or are based on spline-based transformations, we observe that many methods provided clinically significant registration accuracies, while some methods provided target registration accuracies greater than 3 mm.

The methods that reported the gland overlap accuracies exhibited significantly poor overlap (approx. 90%). Additionally, few methods also required manual intervention at some stage to drive the registration procedure. In contrast, our proposed deformable registration method is automatic and capable of providing improved global and local registration accuracies that seem to be necessary for TRUS-guided biopsy procedure.

To evaluate the effects of the proposed method to the existing framework of [44] we have compared our method against two variations; 1) the method of [44] where the TPS control points are placed on a uniform grid over the prostate mask images, and 2) the non-linear TPS deformation same as [44], but with point correspondences established by our proposed method and without the approximation and regularization of bending energy. The proposed method is also evaluated against two commonly used spline-based deformable registration methods of TPS ([23, 135]) and B-splines ([137]). The point correspondences required for the algorithm are established by the method explained in Section 5.2. The non-linear registration as described in Section 5.3 involves TPS transformation of the moving MR image non-linearized by a set of polynomial functions. The registration process aims to minimize the difference between the fixed image and the TPS transformed moving image both non-linearized by the same set of polynomial functions. In addition, the TPS bending energy is minimized with a regularization and considers the localization errors of the point correspondences. The schema of the proposed registration method is shown in Figure 5.1. The rectangles in dotted lines represent the point correspondences method of Section 5.2 and the overdetermined system of equations for the non-linear registration framework of Section 5.3 respectively.

5.2 Shape-contexts and point correspondences

The segmented prostate contour points are uniformly sampled using fixed Euclidean distance of ε i.e. if c_i is a contour point, $i = 1, \ldots, N$, then find the number of points N_s such that

$$\arg\max_j \|c_i - c_j\|^2 \leq \varepsilon, \quad i \neq j. \tag{5.1}$$

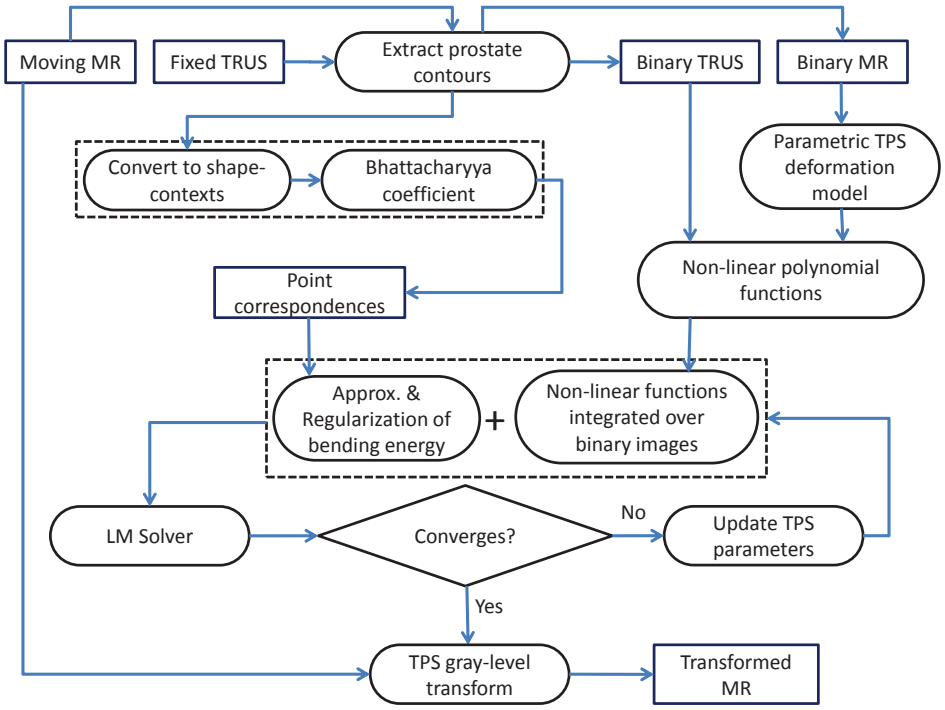

Figure 5.1: Schema diagram of the proposed registration framework.

Figure 5.2 shows the uniformly sampled segmented contours on the TRUS and MR images.

Let the number of uniformly sampled points now be represented as n, then each sample point c_i may be represented by a shape descriptor that is a $n-1$ length vector of log-polar relative distances to points c_j, where $i \neq j$. The shape descriptor is binned into a histogram that is uniform in log-polar space and this histogram is the shape-context representation of a contour point ([14]) i.e. c_i is represented by a histogram $h_i(k,\theta)$ such that

$$h_i(k,\theta) = \#\{c_j, i \neq j \quad : \quad (c_i - c_j) \in bin(k,\theta)\}. \tag{5.2}$$

k is the $\log r = \log(\sqrt{(x_{i1}-x_{j1})^2 + (x_{i2}-x_{j2})^2})$ and $\theta = \tan^{-1}\frac{x_{j2}-x_{i2}}{x_{j1}-x_{i1}}$ of the relative distance $(c_i - c_j)$, where, $c_i = (x_{i1}, x_{i2})$ and $c_j = (x_{j1}, x_{j2})$. As suggested by [14], a total of 5 bins are considered for k and 12 bins for θ that ensures that the histogram is uniform in log-polar space. This also means that more emphasis is given to the

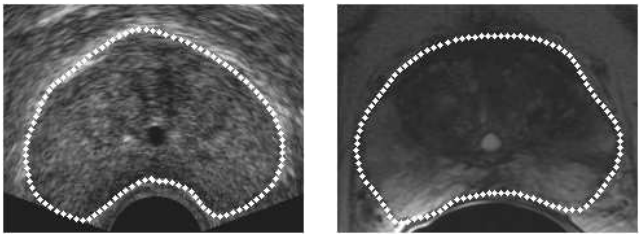

(a) (b)

Figure 5.2: Uniformly sampled contours. (a) and (b) are the uniformly sampled segmented prostate contours on the TRUS and MR images respectively.

nearby sample points than those that are far away.

In the original work of [14], the point correspondence between two shapes is obtained by a bipartite graph matching method. However, in this work we choose to compute the Bhattacharyya distance ([20]) between the shape-context histograms of two shapes to find the point correspondences. The bipartite graph matching using the Hungarian method ([123], [83]) is robust with $O(n^3)$ time complexity in finding point correspondences in shapes which are significantly different and belong to different shape categories ([14]) e.g. correspondences between bird and elephant or bone and apple, etc. However, we considered the Bhattacharyya distance since, it finds point correspondences with $O(n^2)$ time complexity and is sufficient for shapes such as prostate contours in TRUS and MRI which do not significantly differ from each other except for some deformation. Thus, to match a point c_i in a shape to a point c'_j in another shape, the Bhattacharyya coefficients between the shape-context histograms of c_i and all c'_j are computed and the c'_j that maximizes the relation in Equation (5.3) is chosen as the corresponding point.

$$\arg\max_{c'_j} \sum_{k=1}^{5} \sum_{\theta=1}^{12} \sqrt{\hat{h}_i(k,\theta).\hat{h}'_j(k,\theta)}, \tag{5.3}$$

where, $\hat{h}_i(k,\theta)$ and $\hat{h}'_j(k,\theta)$ are the normalized shape-context histograms of c_i and c'_j respectively.

Figure 5.3 shows the log-polar bins of a histogram, the histograms of a point correspondence in two shapes and the contour correspondences overlaid on the TRUS and MR prostate shapes. Figure 5.4 additionally shows some examples

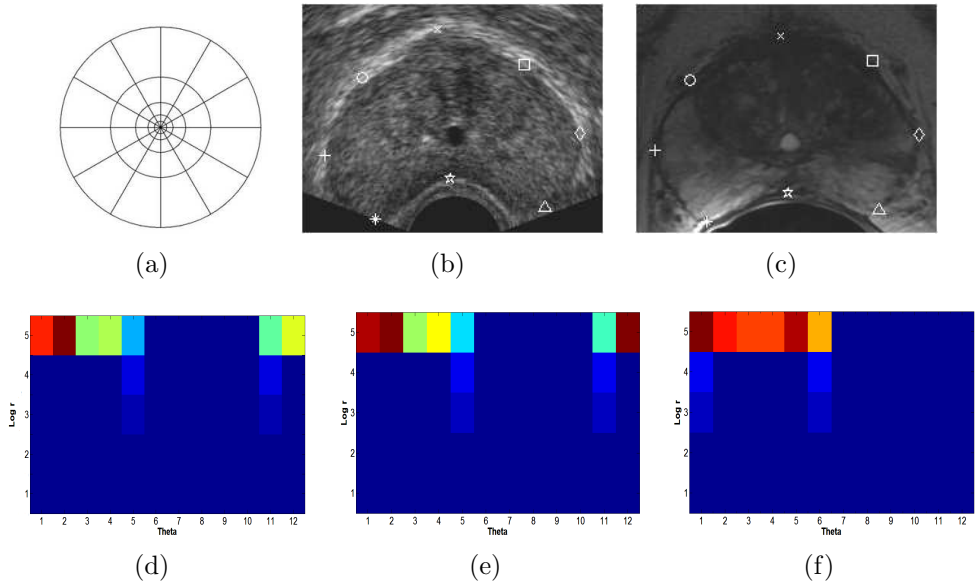

Figure 5.3: Point correspondences example. (a) Log-polar histogram bins; (b) contour points in TRUS; (c) point correspondences of (b) in MR; (d) log-polar shape-context histogram of '∘' in (b); (e) log-polar shape-context histogram of '∘' in (c)- both (d) and (e) show visual correspondence; (f) histogram of '×' in (c) does not show visual correspondence with histogram in (d). The x-y axes in the log-polar shape-context histograms correspond to θ and $\log r$ respectively.

where the prostates are significantly deformed in the MR image than the TRUS image. Nonetheless, Bhattacharyya distance could successfully extract point correspondences on the prostate contours.

The first point correspondence established on both the TRUS and MR prostate boundaries is marked with a '✯' in the posterior part of the axial gland in Figure 5.3(b) and Figure 5.3(c) respectively. This point is obtained in the TRUS image as the intersection point of the longitudinal principal axis with the boundary. The first two principal axes are computed from the principal component analysis of all the contour points of the prostate shape in TRUS. The 8 point correspondences are chosen on the prostate boundary with the rationale of capturing the inflexions of the prostate curve. Therefore, once the first point at the posterior part of the gland is defined on the TRUS boundary, the remaining 7 points are automatically placed dividing the total number of uniformly sampled contour points by 8. Thereafter, the 8 point correspondences are searched for in the MR image using the afore-mentioned

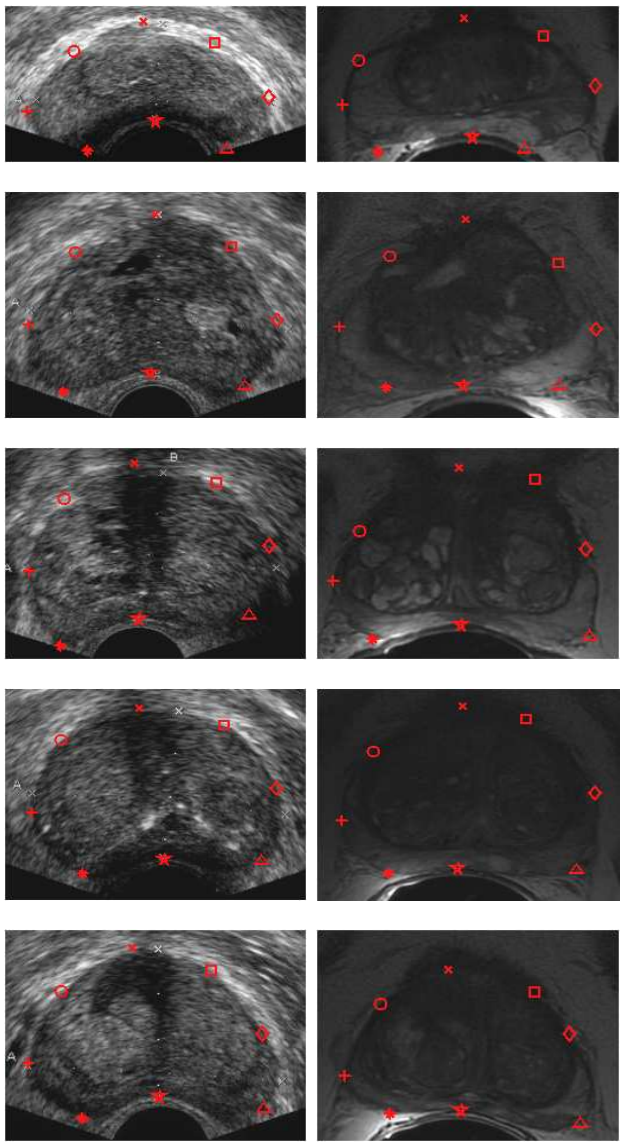

Figure 5.4: Point correspondences on TRUS and MR prostate contours using Bhattacharyya distance. The left column shows the TRUS images and the right column shows the MR images. The MR images show more deformed prostates than those on the TRUS images. The 8 point correspondences are marked in 'red'.

method.

It is evident from the figures 5.3(b) and 5.3(c) respectively that the correspondences are explicitly defined on the prostate contours. Therefore, the regularization of the correspondences will not take the correspondences inside the prostate gland into account and may cause deformations of the gland that are not acceptable for clinical procedures. Hence, the prostate centroids and 4 other points that are the midpoints of the straight lines between '✯' and '+', '+' and '×', '×' and '⋄' and '⋄' and '✯' respectively are considered (see Figure 5.5). The manner in which the internal points are formed i.e. by the mid-points of the lines joining the boundary control points in alternating sequence starting from the first point ('✯'), is necessary to ensure that the control points are placed inside the prostate gland and yet not too close to the boundary control points. The 13 point correspondences finally established may be termed as p_i, where, $i = 1, \ldots, 13$ for further references.

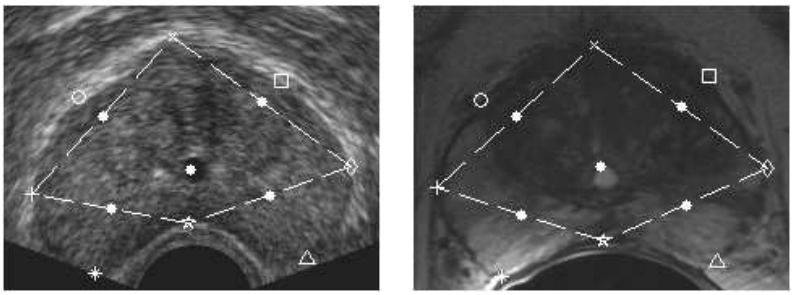

(a) (b)

Figure 5.5: Point correspondences on TRUS and MR images. Correspondences inside the prostate are shown by white '•'s. The dashed line signifies that the white '•' falling on the line is the mid-point of the same joining the correspondences established on the contour.

5.3 Non-linear Diffeomorphism

To align a pair of binary shapes, let us consider the moving and the fixed images be $\mathrm{x} = [x_1, x_2] \in \mathbb{R}^2$ and $\mathrm{y} = [y_1, y_2] \in \mathbb{R}^2$ respectively, such that there exists a bijective

transformation $\varphi(.)$ between the images as

$$\mathrm{y} = \varphi(\mathrm{x}) \Leftrightarrow \mathrm{x} = \varphi^{-1}(\mathrm{y}). \tag{5.4}$$

The deformation field $\varphi(.)$ can be decomposed for the 2D coordinates respectively as $\varphi(\mathrm{x}) = [\varphi_1(\mathrm{x}), \varphi_2(\mathrm{x})]$, where $\varphi_1, \varphi_2 : \mathbb{R}^2 \to \mathbb{R}$. If explicit point correspondences are not established then the diffeomorphism is obtained by integrating over the foreground pixels of the fixed and moving image domains I_f and I_m respectively ([44]):

$$\int_{I_f} \mathrm{y} d\mathrm{y} = \int_{I_m} \varphi(\mathrm{x}) \, |J_\varphi(\mathrm{x})| \, d\mathrm{x}, \tag{5.5}$$

where the integral transformation $\mathrm{y} = \varphi(\mathrm{x})$ and $d\mathrm{y} = |J_\varphi(\mathrm{x})| \, d\mathrm{x}$. $|J_\varphi| : \mathbb{R}^2 \to \mathbb{R}$ is the Jacobian determinant of the transformation at each foreground pixel of the moving image as

$$|J_\varphi(\mathrm{x})| = \begin{vmatrix} \frac{\partial \varphi_1}{\partial x_1} & \frac{\partial \varphi_1}{\partial x_2} \\ \frac{\partial \varphi_2}{\partial x_1} & \frac{\partial \varphi_2}{\partial x_2} \end{vmatrix} \tag{5.6}$$

It is to be noted that the identity relation of Equation (5.4) is also valid under the influence of a set of non-linear functions $\omega_k(.) : \mathbb{R}^2 \to \mathbb{R}$, $k = 1, \ldots, l$ ([44]), acting on both sides of Equation (5.5) as

$$\int_{I_f} \omega_k(\mathrm{y}) d\mathrm{y} = \int_{I_m} \omega_k\big(\varphi(\mathrm{x})\big) \, |J_\varphi(\mathrm{x})| \, d\mathrm{x}. \tag{5.7}$$

Therefore to estimate the parameters of the transformation the number of non-linear functions l, must be larger than the number of parameters to generate a set of linearly independent equations.

In this work, the underlying transformation is considered to be the radial-basis function of TPS where the foreground pixels of the moving image deform under the influence of the control points $p_i \in \mathbb{R}^2$ established by the method of Section 5.2. The

TPS transformation may be written as

$$\varphi_v(\mathrm{x}) = a_{v1}x_1 + a_{v2}x_2 + a_{v3} + \sum_{i=1}^{n} w_{iv}U(p_i - \mathrm{x}), \tag{5.8}$$

where, $i = 1, \ldots n$, $v = 1, 2$, $U : \mathbb{R} \to \mathbb{R}$ is the radial-basis function as $U(r) = r^2 \log r^2$, a_{v1}, a_{v2} and a_{v3} are the 6 affine parameters and w_{iv} are the $2n$ TPS weight parameters for the control points. The additional constraints for the TPS interpolation are that the sum of the weights applied to the plate as well as moments with respect to both axes should be 0 to ensure that the plate will not deform under the action of the loads and are given as

$$\sum_{i=1}^{n} w_{iv} = 0 \quad \text{and} \quad \sum_{i=1}^{n} p_{iu}w_{iv} = 0, \quad u, v = 1, 2. \tag{5.9}$$

If, $\varphi : \mathbb{R}^2 \to \mathbb{R}^2$, $\varphi(\mathrm{x}) = [\varphi_1(\mathrm{x}), \varphi_2(\mathrm{x})]^T$ represents a TPS map with $6+2n$ parameters, then the Jacobian $J_\varphi(\mathrm{x})$ is composed of the partial derivatives ([44]) given below $(u, v = 1, 2)$

$$\frac{\partial \varphi_v}{\partial x_u} = a_{vu} - \sum_{i=1}^{n} 2w_{iv}\big(p_{iu} - x_u\big)\big(1 + \log(\|p_i - \mathrm{x}\|^2)\big) \tag{5.10}$$

where, $\|.\|$ is the Euclidean norm.

However, the transformation of Equation (5.8) when replaced in Equation (5.7) will only consider the point set on the moving image under the influence of which the image deforms to match the fixed image, therefore, the gray-level deformations of the regions inside the prostate may not be meaningful for clinical applications. The correspondences p_i, established across the fixed and moving image domains as $p_i^f = \left[p_{y_{i1}}^f, p_{y_{i2}}^f\right]$ and $p_i^m = \left[p_{x_{i1}}^m, p_{x_{i2}}^m\right]$, $i = 1, \ldots, n$ respectively, play an important role in constraining these deformations. We introduce the bending energy of the TPS along with the correspondence localization errors ([135]) as an additional constraint to solve the set of equations in Equation (5.7) as

$$E_{TPS} = \int_i \int_i \left[\left(\frac{\partial^2 \zeta}{\partial {p_{x_{i1}}^m}^2} \right)^2 + 2\left(\frac{\partial^2 \zeta}{\partial p_{x_{i1}}^m \partial p_{x_{i2}}^m} \right)^2 + \left(\frac{\partial^2 \zeta}{\partial {p_{x_{i2}}^m}^2} \right)^2 \right] \partial p_{x_{i1}}^m \partial p_{x_{i2}}^m, \tag{5.11}$$

where, $\zeta : \mathbb{R}^2 \rightarrow \mathbb{R}^2$, $\zeta = [\zeta_1(p_i^m), \zeta_2(p_i^m)]$ is the transformation of the point correspondences established on the moving image to match with those of the fixed image is defined as

$$\zeta = \zeta_v(p_i^m) = a_{v1}p_{x_{i1}}^m + a_{v2}p_{x_{i2}}^m + a_{v3} + \sum_{j=1}^{n} w_{jv}U(p_i^m - p_j^m), \quad v = 1, 2. \tag{5.12}$$

The 1^{st} and 3^{rd} terms in Equation (5.11) may be written analytically as follows:

$$\frac{\partial^2 \zeta_v}{\partial {p_{x_{iu}}^m}^2} = \sum_{j=1}^{n} 2w_{jv}\left[1 + \log(\left\|p_i^m - p_j^m\right\|^2) + \frac{2(p_{x_{iu}}^m - p_{x_{ju}}^m)}{\left\|p_i^m - p_j^m\right\|^2}\right], \quad u = 1, 2 \tag{5.13}$$

and the 2^{nd} term in Equation (5.11) can be written as

$$\frac{\partial^2 \zeta_v}{\partial p_{x_{i1}}^m \partial p_{x_{i2}}^m} = \sum_{j=1}^{n} 4w_{jv}\left[\frac{(p_{x_{i1}}^m - p_{x_{j1}}^m)(p_{x_{i2}}^m - p_{x_{j2}}^m)}{\left\|p_i^m - p_j^m\right\|^2}\right], \quad v = 1, 2. \tag{5.14}$$

Finally, the equation acting as a constraint is the regularized TPS bending energy with the quadratic approximation term that considers the correspondence localization error, is as follows:

$$\frac{1}{n}\sum_{i=1}^{n} \frac{\left\|p_i^f - \zeta(p_i^m)\right\|^2}{\sigma_i^2} + \lambda E_{TPS} = 0, \tag{5.15}$$

where, σ_i^2s are sum of the variances of the correspondences between the fixed and moving images i.e. $\sigma_i^2 = {\sigma_i^f}^2 + {\sigma_i^m}^2$. The parameter λ is a regularization factor set with a small value 0.0001 that ensures that the thin-plate adapts well to the deformation of the local structures ([135]). Finally, $\zeta(p_i^m)$ is obtained from Equation (5.12) and E_{TPS} from Equation (5.11).

The adopted set of non-linear functions in Equation (5.7) are the power functions as proposed in [44]

$$\omega_k(\mathrm{x}) = x_1^{a_k} x_2^{b_k}, \tag{5.16}$$

with $(a_k, b_k) \in \big\langle(0,0),(1,0),(0,1),(1,1),(2,0),(0,2),(2,1),(1,2),(2,2),\ldots,(6,6)\big\rangle$. The total number of parameters to be estimated is 32 that comprises of

6 affine and 13×2 TPS weight parameters for 13 correspondences. Therefore, 49 linearly independent equations are generated using the power set of $\omega_k(.)$ functions with additional 4 equations for Equation (5.9) and one for Equation (5.15). The solution to the set of non-linear equations i.e. Equation (5.7), Equation (5.9) and Equation (5.15) is obtained using *Levenberg-Marquardt* (LM) algorithm ([104]). It is to be noted that depending on the ω_k functions in Equation (5.7), numerical instability may arise due to the summation of the polynomial functions, i.e. the power functions $\omega_k(.)$ act on the set of coordinate values of the images, therefore summing up the coordinate values (raised by some factor) would result in very large values. In order to solve this problem, the foreground pixels of the moving and fixed images are normalized within a unit square $[-0.5, 0.5] \times [-0.5, 0.5]$ so that the shape centers become the origins while the range of ω_k functions are chosen within the interval $[-1, 1]$. A detailed explanation on the normalization of the image coordinates and the interval of $\omega_k(.)$ functions is provided by [44].

5.4 Experimental setup

The aim of this work is to register a TRUS prostate image acquired during biopsy with a pre-acquired MR image of the same patient. Since the current proposition is to ascertain the feasibility and accuracy of the registration algorithm for biopsy procedures, the method requires an initial step of finding the MR slice corresponding to the axial TRUS slice under observation. This may be accomplished by using an electromagnetic (EM) tracker attached to the TRUS biopsy probe ([168]) or a 3D US-based tracking system ([12]). Slice correspondences are therefore determined manually by an expert for the proposed research. However, a method to automatically determine axial TRUS-MR slice correspondences will be discussed in Chapter 7.

In this work, after the TRUS-MR slice correspondences are established, the prostate is manually segmented from the respective modalities. Although, our research team is investigating on automatic prostate segmentation methods from both TRUS and MRI ([65, 67, 62]), we use manual segmentation to avoid incorporating the segmentation errors in the evaluation of the registration algorithm. The choice of an automatic or semi-automatic prostate segmentation method can be made from

the review paper published by [173].

Prostate mid-gland images of the same 20 patients as described in Section 4.5 of Chapter 4 are used for the evaluation of our algorithm. The axial middle slices in TRUS are chosen for which the corresponding axial MR slices are identified by one expert radiologist and one expert urologist. Axial sweeps of the prostate gland from base to apex/mid-gland are only available for 2 patient cases in TRUS whose corresponding MR slices could also be identified. Therefore, these two cases are used to show the accuracy of the proposed registration method for off-mid-gland TRUS-MR slices. The prostates are manually segmented from both the moving MR and fixed TRUS images. The image backgrounds are removed and only a region of interest i.e. the prostate is used for the evaluation of the algorithm. The proposed point correspondence and registration methods were implemented on MATLAB 2009(b) and were run on an Intel Core2Duo 1.66 GHz processor with 2 GB RAM.

5.5 Experiments and Results

The TRUS slice is the fixed image and the respective MR slice is the moving image for all the experiments. The evaluation metrics used are the same as defined in Chapter 4, Section 4.5.

Various experiments are performed owing to the selection criteria of the number of boundary and internal control points for a smooth and accurate deformation of the prostate gland and its internal structures. The validations of such experiments with varying number of control points are shown in Section 5.5.1. The experimental results with different registration methods are shown in Section 5.5.2. The validation of registration accuracies on a subset of patients when automatic segmentation is used is shown in Section 5.5.3 and experimental results for the validation of the proposed registration method for off mid-gland slices are shown in Section 5.5.4. A comprehensive statistical analysis of the results is presented in Section 5.5.5.

5.5.1 Control Points

As mentioned in Section 5.2 that a total of 8 point correspondences are required on the boundary and 4 internal points along with 1 point on the prostate centroid for

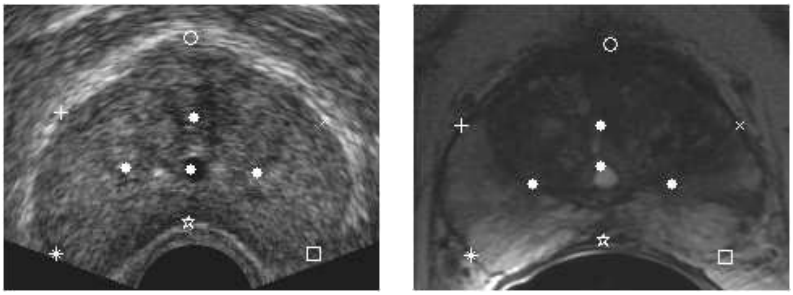

(a) (b)

Figure 5.6: 6 point correspondences on the boundary with 3 internal points and 1 point on prostate centroid. The '✯'s mark the first set of point correspondences on the boundary. (a) Point sets on the TRUS image, (b) corresponding points of TRUS image on the MR prostate image.

a smooth deformation. Therefore, to validate the number of boundary and internal points, several experiments are performed with less and more than 8 boundary points along with the internal points generated in an alternating manner as mentioned in Section 5.2.

The first experiment is done with only 6 points on the boundary and the internal points are generated accordingly as the mid-points of the lines joining the alternate boundary points starting from the first point '✯' as shown in Figure 5.6. It can be seen clearly from Figure 5.6(a) and Figure 5.6(b) respectively that the inflexion points at the posterior parts of the prostate axial slices are not captured properly.

The following experiment is done increasing the number of boundary points from 8 (proposed) to 10. Accordingly the internal points are also generated. Figure 5.7(a) and Figure 5.7(b) show the 10 boundary and 5 internal points along with 1 prostate centroid. Although the boundary has several points to capture the inflexions of the prostate curve, the internal points generated are placed near the boundaries. This may result in distorted deformations of the prostate internal structures.

Finally an experiment is performed using 8 boundary points without any internal points or centroid. Figure 5.8(a) and Figure 5.8(b) show the point correspondences placed on the boundary for the TRUS and the MR prostate images respectively.

Table 5.1 shows the registration accuracies in terms of DSC, TRE and TLE for the experiments performed with varied number of control points for all 20 patient

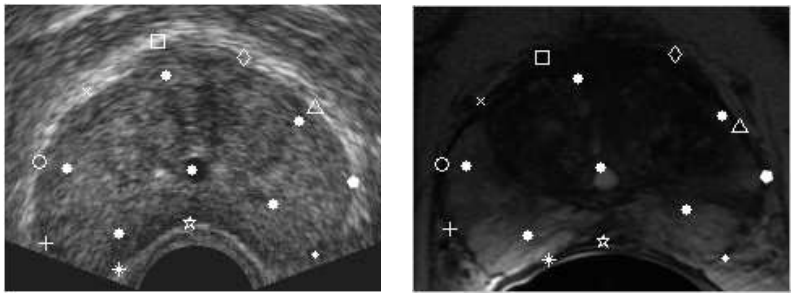

(a) (b)

Figure 5.7: 10 Point correspondences on the boundary with 5 internal points and 1 point on prostate centroid. The '☆'s mark the first set of point correspondences on the boundary. (a) Point sets on the TRUS image, (b) corresponding points of TRUS image on the MR prostate image.

cases. M1 is defined for 6 boundary points and 4 internal points, M2 is defined for 10 boundary points and 6 internal points and M3 is defined for 8 boundary points and no internal points. These abbreviations are being consistently used in the remaining document. As shown by the DSC values of Table 5.1 that with varying point correspondences on the boundary, the global registration accuracies do not change significantly by the virtue of the diffeomorphic function. However, the local registration accuracies measured in terms of TRE have a lot of variation between the different methods M1, M2 and M3 respectively. Figure 5.9 shows the qualitative registration results using the proposed method with different sets of control points for patient 6. Although the qualitative results with M1 and M2 (rows 2 and 3) do not show significant differences with the proposed 8 boundary and 5 internal points (last row), the unconstrained deformation in the absence of the internal points is seen for the method M3 (row 4), i.e. the prostatic urethra in the deformed image is away from that on the fixed image.

5.5.2 Registration Methods

The proposed method and its two variants as mentioned in Section 5.1 are replaced by acronyms for further references as NLTPS-REGCORR (proposed), NLTPS-UNI (non-linear TPS with control points placed on a uniform grid) and NLTPS-CORR (non-linear TPS with proposed point correspondences without regularization of

Table 5.1: A comparison of global and local registration accuracies for the proposed method with varying control points. M1 is the acronym for 6 boundary points and 4 internal points, M2 is the acronym used for 10 boundary points and 6 internal points and M3 is the acronym used for 8 boundary points and no internal points. P# represents the patient number, μ is the mean and σ is the standard deviation of the measures. A high DSC value signifies good global registration accuracy, while a low TRE and TLE signifies good local registration accuracies around anatomical landmarks.

P#	**Varying Point Correspondences**								
	M1			**M2**			**M3**		
	DSC	TRE (mm)	TLE (mm)	DSC	TRE (mm)	TLE (mm)	DSC	TRE (mm)	TLE (mm)
1	0.974	1.08	0.23	0.957	2.79	0.09	0.968	2.37	0.25
2	0.985	1.78	0.06	0.985	1.46	0.05	0.978	1.29	0.05
3	0.980	2.29	0.07	0.981	1.22	0.04	0.980	0.98	1.14
4	0.986	3.01	0.50	0.988	2.39	0.30	0.984	1.85	0.84
5	0.984	0.79	0.05	0.979	0.59	0.07	0.978	1.39	0.95
6	0.970	0.39	0.03	0.973	0.26	0.04	0.971	1.76	0.05
7	0.984	3.89	0.09	0.982	3.60	0.12	0.985	12.05	0.03
8	0.981	5.59	0.20	0.984	2.08	0.58	0.981	2.30	0.32
9	0.983	1.33	0.28	0.981	1.98	0.15	0.981	1.87	0.24
10	0.985	3.98	0.05	0.986	4.03	0.04	0.986	4.15	0.03
11	0.983	2.38	0.08	0.982	1.93	0.08	0.980	2.81	0.05
12	0.982	1.15	0.26	0.982	0.98	0.32	0.981	1.33	0.26
13	0.984	3.84	0.06	0.981	5.21	0.05	0.983	5.64	0.07
14	0.982	0.65	0.04	0.986	0.46	0.02	0.986	2.52	0.04
15	0.984	14.05	0.08	0.982	14.07	1.10	0.984	17.40	0.07
16	0.985	2.91	0.09	0.979	1.44	0.08	0.980	2.08	0.10
17	0.981	2.12	0.28	0.982	1.87	0.19	0.984	2.45	0.16
18	0.977	0.67	0.30	0.980	1.42	0.28	0.980	0.60	0.33
19	0.979	1.96	0.08	0.979	2.05	0.04	0.978	1.36	0.17
20	0.976	0.76	0.21	0.982	1.13	0.36	0.984	0.60	0.19
μ	**0.981**	**2.73**	**0.15**	**0.981**	**2.55**	**0.20**	**0.981**	**3.34**	**0.27**
σ	**0.004**	**3.01**	**0.12**	**0.006**	**2.98**	**0.26**	**0.005**	**4.16**	**0.33**

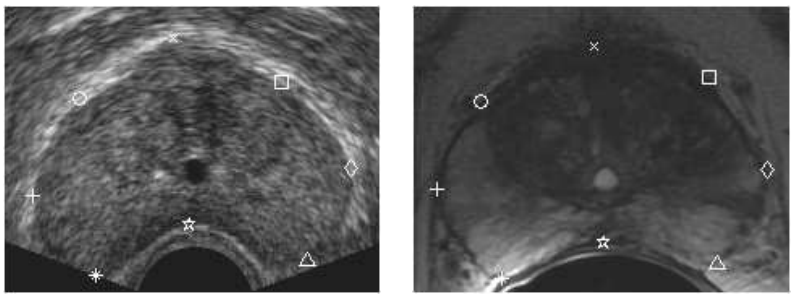

(a) (b)

Figure 5.8: 8 Point correspondences on the boundary with no internal points or centroid. The '✯'s mark the first set of point correspondences on the boundary. (a) Point sets on the TRUS image, (b) corresponding points of TRUS image on the MR prostate image.

bending energy) respectively. The method in NLTPS-REGCORR and NLTPS-CORR use 13 point correspondences established by the method in Section 5.2. A total of 16 uniform grid-points are used for NLTPS-UNI. We have quantitatively compared the registration results of NLTPS-REGCORR against NLTPS-UNI, NLTPS-CORR, traditional TPS ([135]) and B-splines ([137]) method with their global registration accuracies in terms of DSC, 95% HD, local registration accuracies in terms of TRE, TLE and timing requirements in Table 5.2 and Table 5.3 respectively. The traditional TPS ([135]) registration method is used with a total of 32 point correspondences on the boundary with 5 internal points as discussed in [108]. The B-splines registration follows a multiresolution framework in 3 spatial resolutions and uses uniform control grids with 16×16 pixel spacing in the final resolution ([91]). Table 5.3 also shows the number of uniform control grids used for the B-splines ([137]) registration. It is to be noted that the traditional TPS requires a total of 37 point correspondences to provide a smooth transformation, while our proposed method can perform well with only 13 point correspondences. The traditional TPS finds the transformation as a solution to a least-squares problem. Any least-squares solution requires an over-determined system of equations to provide numerically stable solutions. Therefore, the traditional TPS uses more number of control points than our proposed method since only one equation is associated with each control point. On the contrary, a set of power function polynomials are involved

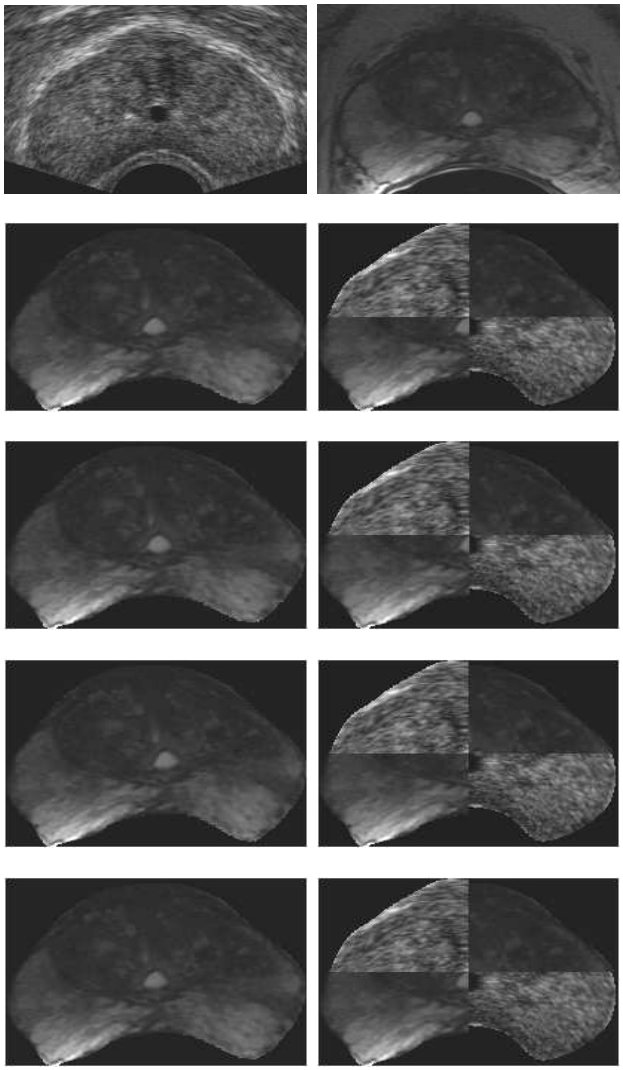

Figure 5.9: Deformation of the prostate gland with different sets of control points for Patient 6. Row 1 shows the TRUS and the MR images, row 2, 3 and 4 show the qualitative results of methods M1, M2 and M3 respectively and row 5 shows the results with the proposed optimum set of control points.

with each control point for our method; thereby providing an over-determined system of equations with less number of control points. Since the B-splines of [137] uses uniform control grid; therefore a consistent number of control points similar to the traditional TPS or the proposed method could not be used.

Figure 5.10 shows some results of the transformation using the methods NLTPS-UNI, NLTPS-CORR and NLTPS-REGCORR respectively. The results for patients $7, 8, 11$ and 12 are shown in each column. Figure 5.11 shows some of the results of TRUS-MR fusion with traditional TPS and B-splines and the corresponding results using our proposed method. The TPS uses point correspondences as described in Section 4.1.1 and the B-splines used uniform grids. The results for patients $1, 5, 15$ and 17 are shown in columns. The choice of a different set of patient cases for Figure 5.11 ensures that more qualitative results obtained from the proposed algorithm are shown. Moreover, the results that are unbiased towards the proposed method and have acceptable registration accuracies when traditional spline-based methods are used are also presented.

5.5.3 Automatic Segmentation

The registration methods as discussed in Section 5.3 are performed using manually segmented prostate contours for both the TRUS and MR images in order to avoid the automatic segmentation errors in the process of evaluating the registration accuracies. However, we have used 10 patient cases i.e. patients $5 - 14$ among the 20 patients to evaluate the sensitivity of the registration accuracies when an automatic segmentation method is employed. The method of [62] is used to segment the prostate from both the TRUS and MR images. Figure 5.12 shows the final segmented contours in red lines for the TRUS and the MR images, the point correspondences placed accordingly and the qualitative registration results for the same patient case. It is observed from the figure that the automatic segmentation of the prostate contour in the MR image has the maximum overlap with the manual segmentation while a satisfactory overlap is obtained for the prostate contour in the TRUS image.

Table 5.4 shows the DSC, HD, TRE and TLE values for the 10 patients (patient $5 - 14$). It is to be noted that despite some segmentation inaccuracies induced

Table 5.2: A comparison of registration accuracies of the non-linear TPS registration NLTPS-UNI, NLTPS-CORR, NLTPS-REGCORR, traditional TPS and B-splines respectively. μ is the mean and σ is the standard deviation of the measures. A high DSC and low TRE and TLE values signify good registration accuracy. The '-' values indicate that the targets could not be identified due to significant deformation of the gland after the transformation.

P#	**NLTPS-UNI**			**NLTPS-CORR**			**NLTPS-REGCORR**			**TPS** ([135])			**B-splines** ([137])		
	DSC	TRE (mm)	TLE (mm)	DSC	TRE (mm)	TLE (mm)	DSC	TRE (mm)	TLE (mm)	DSC	TRE (mm)	TLE (mm)	DSC	TRE (mm)	TLE (mm)
1	0.979	2.30	0.12	0.944	-	-	0.968	1.28	0.28	0.971	9.36	0.22	0.902	5.07	0.10
2	0.987	2.59	0.09	0.989	5.00	0.21	0.981	1.34	0.07	0.957	3.98	0.10	0.980	0.37	0.09
3	0.987	2.63	0.03	0.984	5.80	0.09	0.980	1.12	0.09	0.974	7.92	0.13	0.973	9.93	0.11
4	0.989	1.42	0.07	0.989	2.76	0.02	0.982	0.93	0.54	0.982	5.21	0.49	0.985	1.91	0.28
5	0.990	1.63	0.03	0.989	3.97	0.06	0.979	0.50	0.08	0.972	2.11	0.07	0.889	9.08	0.04
6	0.989	7.03	0.78	0.990	3.24	0.04	0.971	0.29	0.03	0.979	1.17	0.05	0.869	6.11	0.04
7	0.989	14.29	0.26	0.987	13.99	0.50	0.984	3.86	0.10	0.977	4.43	0.12	0.959	0.90	0.12
8	0.992	-	-	0.988	7.55	0.08	0.979	1.23	0.11	0.978	3.57	0.05	0.976	4.70	0.03
9	0.987	1.89	0.02	0.988	1.99	0.03	0.981	1.10	0.24	0.978	2.70	0.46	0.960	1.56	0.41
10	0.989	2.15	0.02	0.989	3.07	0.02	0.984	3.58	0.03	0.972	6.09	0.04	0.952	8.29	0.09
11	0.990	12.95	0.38	0.989	12.68	0.34	0.980	2.63	0.07	0.972	2.98	0.12	0.962	6.12	0.04
12	0.982	1.11	0.05	0.980	1.35	0.12	0.981	0.94	0.21	0.971	2.44	0.12	0.944	1.58	0.25
13	0.985	7.47	0.33	0.986	6.22	0.34	0.983	4.54	0.07	0.980	3.06	0.07	0.961	1.00	0.05
14	0.989	10.64	0.28	0.991	7.28	0.21	0.986	0.24	0.05	0.986	1.75	0.07	0.896	7.32	0.05
15	0.987	1.60	0.09	0.988	3.47	0.06	0.984	1.65	0.07	0.968	2.29	0.07	0.942	5.01	0.05
16	0.984	4.91	0.06	0.986	3.40	0.02	0.980	2.01	0.10	0.970	1.86	0.07	0.974	7.27	0.13
17	0.984	1.11	0.10	0.987	3.22	0.08	0.982	1.30	0.27	0.982	0.18	0.32	0.894	4.32	0.12
18	0.985	0.65	0.02	0.983	1.26	0.01	0.979	1.34	0.23	0.982	0.91	0.26	0.985	0.51	0.26
19	0.983	3.08	0.20	0.983	3.66	0.13	0.978	1.14	0.12	0.983	1.47	0.23	0.936	5.12	0.19
20	0.985	1.61	0.04	0.986	2.41	0.17	0.983	1.07	0.19	0.973	3.11	0.30	0.939	5.03	0.20
μ	**0.987**	**4.27**	**0.16**	**0.985**	**4.86**	**0.13**	**0.980**	**1.60**	**0.15**	**0.975**	**3.33**	**0.17**	**0.944**	**4.56**	**0.13**
σ	**0.003**	**4.20**	**0.19**	**0.010**	**3.49**	**0.13**	**0.004**	**1.17**	**0.12**	**0.007**	**2.33**	**0.14**	**0.036**	**2.98**	**0.10**

Table 5.3: Comparison of registration accuracies in terms of 95% HD and timing requirements for NLTPS-UNI, NLTPS-CORR and NLTPS-REGCORR, TPS ([135]) and B-splines ([137]) registration methods. μ signifies the mean values and σ the standard deviation. A low HD value corresponds to good contour registration accuracy.

P#	**NLTPS-UNI**		**NLTPS-CORR**		**NLTPS-REGCORR**		**TPS** ([135])		**B-splines** ([137])		
	Time (s)	HD (mm)	Time (s)	HD (mm)	Time (s)	HD (mm)	Time (s)	HD (mm)	Grid	Time (s)	HD (mm)
1	92.15	1.51	87.62	3.13	87.58	1.89	50.15	1.84	12×20	147.32	9.35
2	72.21	0.78	67.78	0.78	67.93	1.07	22.71	2.32	13×15	98.30	1.07
3	122.02	1.47	115.19	1.64	115.05	1.74	83.91	2.09	15×20	126.30	2.08
4	123.66	0.82	116.91	0.94	109.70	1.30	94.58	1.40	17×19	140.47	1.07
5	111.06	1.07	105.54	0.82	105.73	1.30	55.35	2.35	14×19	107.82	8.06
6	99.08	0.82	93.81	0.82	93.46	1.98	47.20	2.32	14×18	89.98	6.16
7	175.63	1.10	166.81	1.56	171.96	1.64	153.14	2.61	18×22	146.59	5.04
8	129.14	0.73	123.68	1.07	125.78	1.56	96.95	2.96	17×20	192.83	3.38
9	138.08	2.56	130.89	2.23	134.11	2.86	99.88	2.39	17×20	218.27	4.93
10	131.82	1.04	130.90	1.04	124.41	1.30	89.56	1.98	18×19	214.63	5.98
11	124.86	0.94	124.21	0.94	122.08	2.14	65.33	2.22	15×19	146.87	3.03
12	115.77	0.94	115.59	1.47	123.65	1.64	85.82	5.00	17×19	163.02	4.60
13	132.74	1.30	130.64	1.30	125.23	1.30	84.02	1.84	16×20	141.72	4.83
14	106.81	1.04	122.51	1.04	99.38	1.04	57.14	0.82	14×19	100.61	6.50
15	112.38	1.07	105.28	1.10	105.48	1.30	70.43	2.22	16×18	110.42	6.06
16	106.42	1.74	98.15	1.40	112.74	1.51	62.91	2.71	15×19	209.27	2.90
17	90.26	1.10	84.55	0.73	84.30	1.30	44.14	1.04	15×16	73.57	7.18
18	125.64	1.30	119.38	1.56	118.90	1.82	72.02	1.64	17×18	195.15	2.32
19	158.11	2.86	149.98	2.32	150.53	2.56	126.19	1.66	19×20	135.03	7.01
20	101.42	1.10	95.34	1.16	97.42	1.30	62.99	2.08	16×18	186.74	5.51
μ	**118.46**	**1.31**	**114.24**	**1.35**	**113.77**	**1.63**	**76.22**	**2.17**	-	**147.25**	**4.85**
σ	**23.54**	**0.57**	**23.05**	**0.61**	**23.43**	**0.48**	**29.79**	**0.85**	-	**43.81**	**2.30**

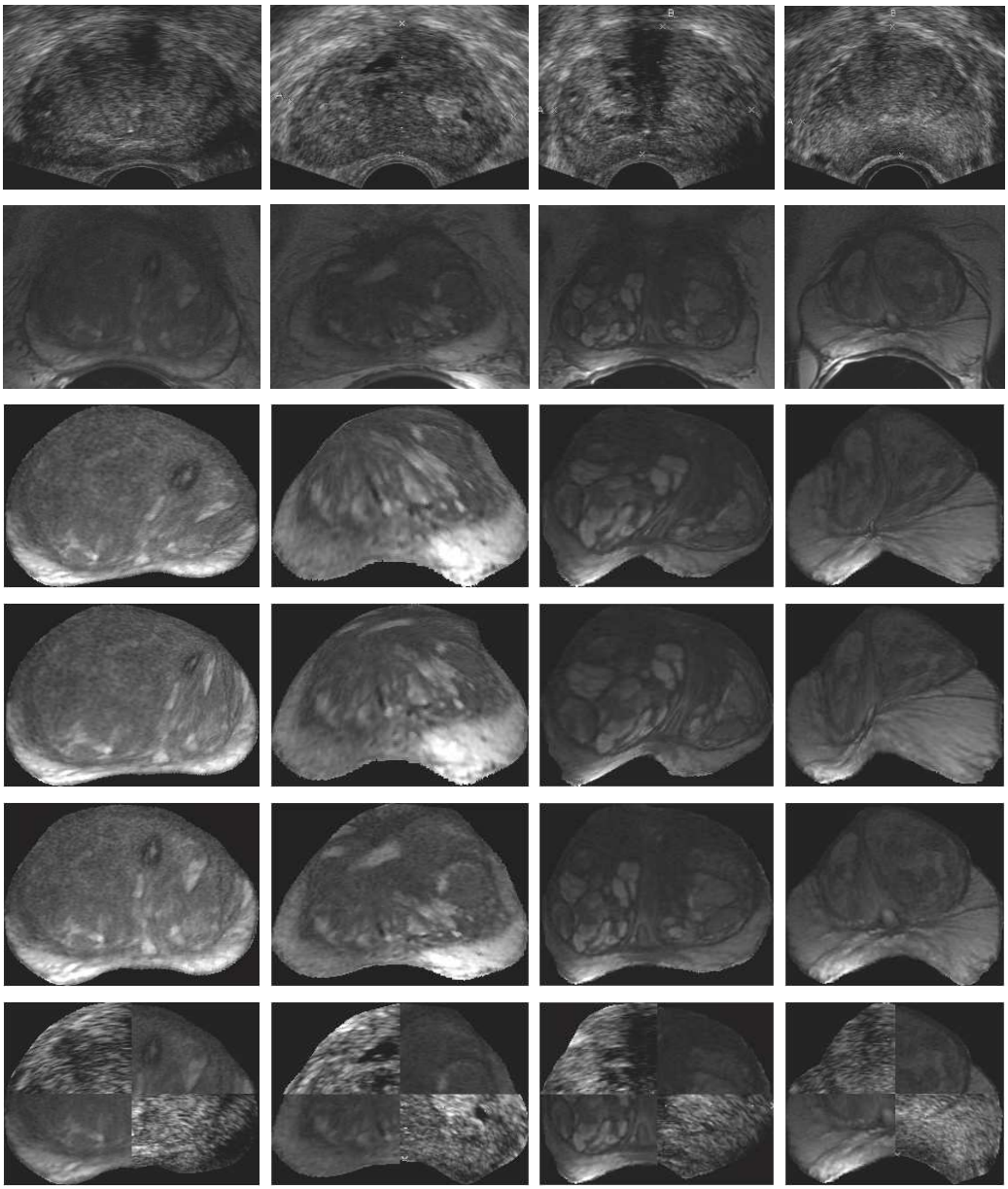

Figure 5.10: Qualitative registration results of NLTPS-UNI, NLTPS-CORR and NLTPS-REGCORR for patients $7, 8, 11$ and 12. Rows 1 and 2 are the fixed TRUS and the moving MR images respectively. Rows 3 and 4 show the transformed MR images for the methods NLTPS-UNI and NLTPS-CORR respectively. Rows 5 and 6 show the transformed MR images and the checker-board of the fixed TRUS and the transformed MR images for the method NLTPS-REGCORR (proposed).

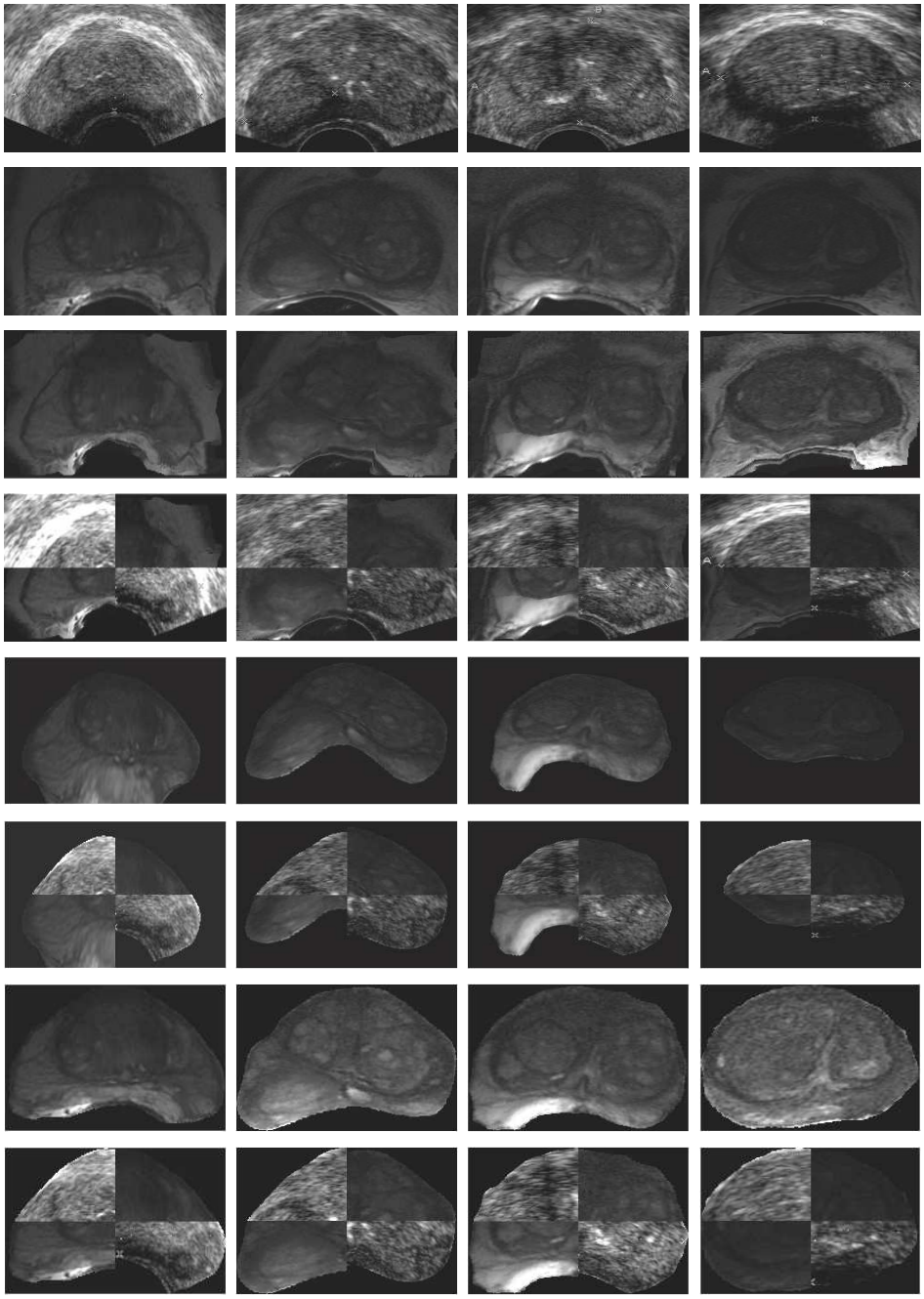

Figure 5.11: Qualitative registration results for TPS, B-splines compared with the proposed method (NLTPS-REGCORR). The columns signify patient cases $1, 5, 15$ and 17 respectively. Rows 1 and 2 show the fixed TRUS and moving MR images respectively. Rows 3 and 4 show the transformed MR and checkerboard using traditional TPS. Similarly, rows 5 and 6 show the results of B-splines and rows 7 and 8 show the results of the proposed method.

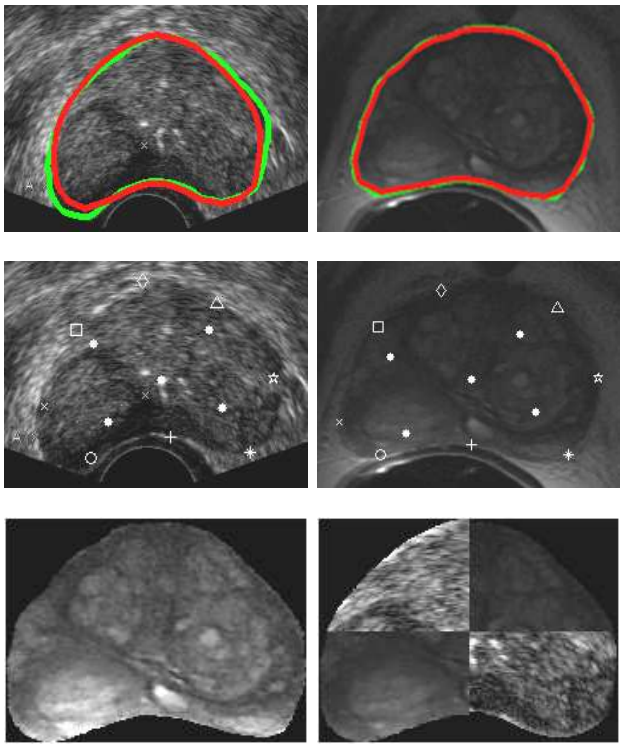

Figure 5.12: Qualitative registration results with point correspondences established according to automatically segmented prostate contours. The first row shows the contours obtained using automatic segmentation method (in red) and manual segmentation (in green) on both TRUS and MR images. The second row shows the point correspondences on the prostate for both the TRUS and MR images and the third row shows the resulting fused TRUS-MR image and the TRUS-MR checkerboard.

Table 5.4: Quantitative global and local registration accuracies when automatic segmentation ([62]) method is used. μ denotes the mean and σ denotes the standard deviation of the respective measures. A high DSC, low HD, low TRE and low TLE represent good registration accuracy.

P#	DSC	HD (mm)	TRE (mm)	TLE (mm)
5	0.986	0.78	1.28	0.09
6	0.981	1.30	0.90	0.02
7	0.985	1.30	2.27	0.06
8	0.983	1.56	1.40	0.07
9	0.982	1.56	1.58	0.23
10	0.987	1.10	1.65	0.04
11	0.977	1.66	1.60	0.05
12	0.983	1.40	2.03	0.22
13	0.981	1.30	3.04	0.12
14	0.979	1.40	1.67	0.04
μ	**0.982**	**1.34**	**1.74**	**0.09**
σ	**0.003**	**0.25**	**0.59**	**0.07**

by the automatic segmentation process; the registration accuracies do not change significantly when compared to the registration with manually segmented contours.

5.5.4 Registration of Non Mid-Gland Slices

The proposed registration method has been evaluated with one axial mid-gland slice for each of the 20 patients. However, 2D sweeps of the prostate from base to apex/mid-gland in TRUS are available for two patients 6 and 7 respectively. Therefore, to validate the proposed registration method for non mid-gland slices the afore-mentioned patient datasets are used. Since a tracking system is not used with the TRUS probe, the probe angle cannot be retrieved; that obviates an assumption in the validation process that the TRUS slices are parallel to the corresponding MR slices. A total of 9 axial slices are taken for patient 6 and 7 axial slices for patient 7 respectively. Table 5.5 shows the slice-by-slice registration accuracies for the patients 6 and 7 in terms of DSC, TRE and TLE. Figure 5.13 shows the TRUS-MR slices from base to apex for patient 6 and their qualitative registration results.

Table 5.6 summarizes the different experiments performed for mid-gland/non mid-gland registrations with manual/automatic segmentation on different patient

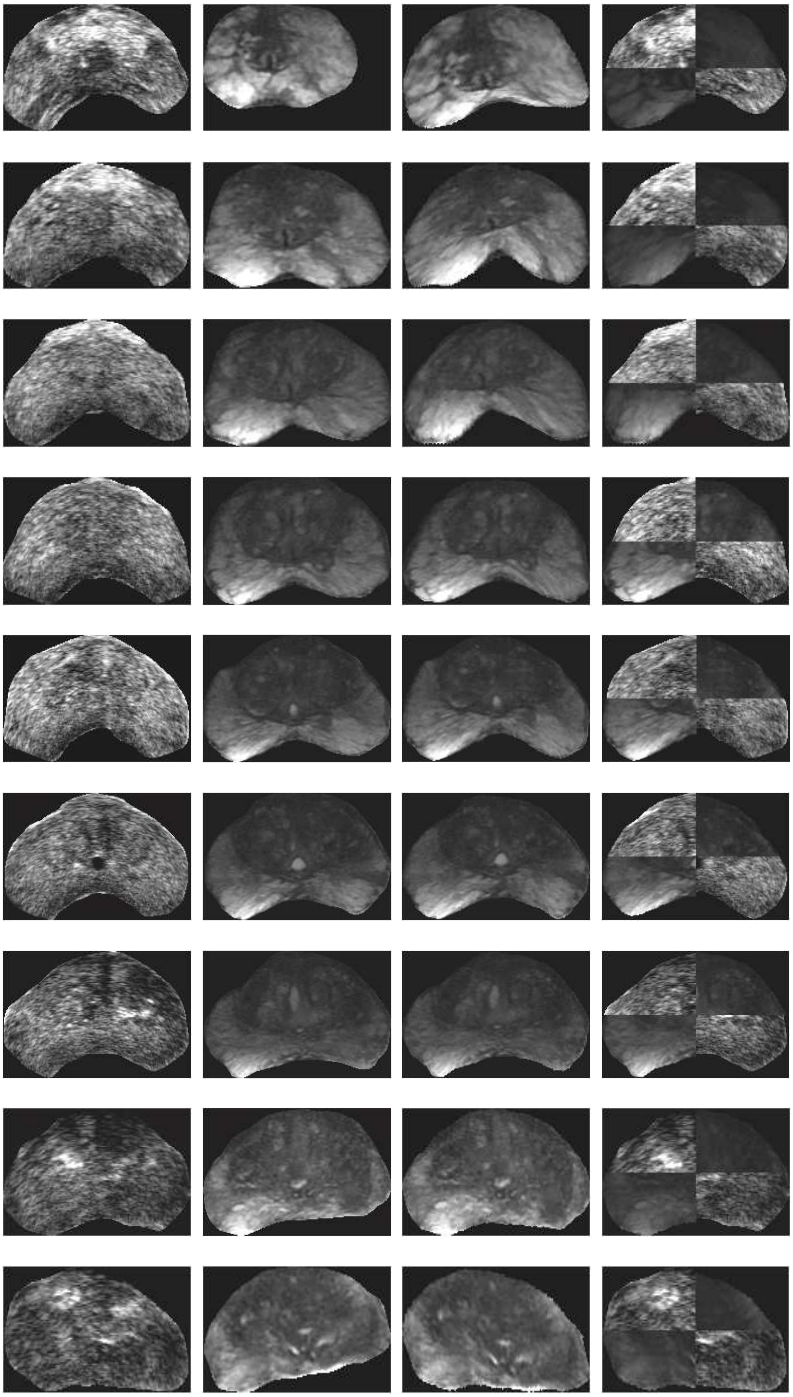

Figure 5.13: Qualitative results of the proposed method when applied to non mid-gland slice. The rows show the base to apex slice registrations (rescaled) top-to-bottom for Patient 6.

Table 5.5: Slice-by-slice registration accuracies for base to apex slices. μ denotes the mean and σ denotes the standard deviation of the respective measures. S# denotes slice number from base to apex. A high DSC, low TRE and low TLE represent good registration accuracy.

S#	Patient 6			Patient 7		
	DSC	TRE (mm)	TLE (mm)	DSC	TRE (mm)	TLE (mm)
1	0.961	1.39	0.12	0.978	1.73	0.06
2	0.974	1.26	0.09	0.985	2.69	0.03
3	0.981	0.70	0.02	0.981	0.95	0.02
4	0.977	1.66	0.21	0.980	2.20	0.08
5	0.974	0.73	0.03	0.974	2.80	0.56
6	0.973	0.29	0.01	0.976	3.21	0.23
7	0.972	1.09	0.54	0.984	3.57	0.19
8	0.980	0.95	0.25	-	-	-
9	0.982	1.08	0.08	-	-	-
μ	**0.975**	**1.02**	**0.15**	**0.980**	**2.45**	**0.17**
σ	**0.006**	**0.41**	**0.17**	**0.004**	**0.90**	**0.19**

cohorts.

Table 5.6: Quantitative registration results for mid-gland and off mid-gland registration with manual or automatic segmentation on different patient cohorts.

Exp#	**1**	**2**	**3**
Method	NLTPS-REGCORR	NLTPS-REGCORR	NLTPS-REGCORR
Segmentation	manual	manual	automatic
Prostate	mid-gland	off mid-gland	mid-gland
Patients	1 – 20	6, 7	5 – 14
DSC	0.980 ± 0.004	0.977 ± 0.006	0.982 ± 0.003
TRE (mm)	1.60 ± 1.17	1.64 ± 0.97	1.74 ± 0.59

5.5.5 Statistical Analysis

5.5.5.1 Control Points

It is observed from Table 5.7 for a varied number of control points (M1, M2 & M3) and for the proposed with 13 control points (NLTPS-REGCORR) that the average DSC values are almost similar. Therefore, to measure the statistical significance of the null hypothesis that the mean values of all the methods are similar we need to verify the normality and homogeneity of the variances (homoscedasticity) of the

Table 5.7: A comparison of the global and local registration accuracies for the different methods and their statistical significance. The methods are abbreviated from A to H for M1, M2, M3, NLTPS-UNI, NLTPS-CORR, NLTPS-REGCORR, TPS and B-splines respectively. HD and TRE are in (mm) with μ denoting the mean and σ the standard deviation. Statistical significance is computed for 95% confidence interval i.e a $p < 0.05$ is considered as similarity of means with high statistical significance, while a very low p-value denotes significantly different means. The letters within brackets in the p-value field (p) denote the methods that are used for comparison. The empty p-value fields signify that either the comparisons are irrelevant or could not be computed due to non-normal and heteroscedastic data.

Methods		**M1**	**M2**	**M3**	**NLTPS-UNI**	**NLTPS-CORR**	**NLTPS-REGCORR**	**TPS** ([135])	**B-splines** ([137])
Abbrv.		*A*	*B*	*C*	*D*	*E*	*F*	*G*	*H*
DSC	μ	0.981	0.981	0.981	0.987	0.985	0.980	0.975	0.944
	σ	0.004	0.006	0.005	0.003	0.010	0.004	0.007	0.036
	p	< 0.03 (*A,B,C,F*)	-	-	< 0.01 (*D,F*)	< 0.01 (*E,F*)	< 0.0001 (*D,E,F*)	-	-
HD	μ	-	-	-	1.31	1.35	1.63	2.17	4.85
	σ	-	-	-	0.57	0.61	0.48	0.85	2.30
	p	-	-	-	< 0.01 (*D,F*)	< 0.01 (*E,F*)	< 0.0001 (*D,E,F*)	-	-
TRE	μ	2.73	2.55	3.34	4.27	4.86	1.60	3.33	4.56
	σ	3.01	2.98	4.16	4.20	3.49	1.17	2.33	2.98
	p	=0.0035 (*A,B,C,F*)	-	< 0.05 (*C,F*)	-	-	< 0.005 (*E,F,H*)	-	< 0.0006 (*D-H*)

data ([144, 170]). Common data transformations such as log, square-root and arcsine transformations could not suitably scale the data to a normal distribution. Hence, Lilliefors test ([97]) was used on the raw data to verify the normality of the distribution. The test rejected the null hypothesis of normal distribution. Consequently, Levene's test ([96]) is used to verify the homogeneity of the variances for the three methods which accepted the null hypothesis (Levene's test is used to measure the homogeneity of variances if the data are non-normal, otherwise, Bartlett's test could have been used). Since the measurements of DSC are taken for the same samples over the methods (M1, M2, M3 and NLTPS-REGCORR), we considered Friedman's

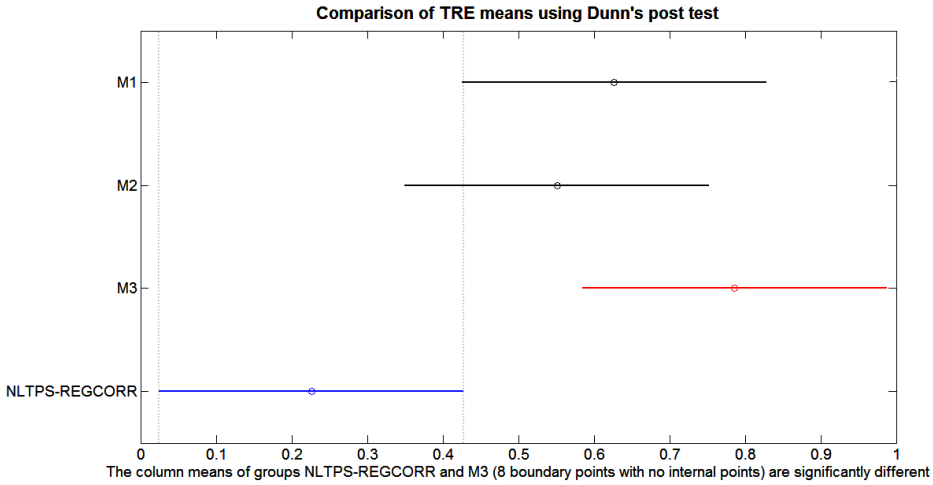

Figure 5.14: TRE means for different methods with significant difference between M3 (red line) and NLTPS-REGCORR (blue line).

test ([59]) (similar to two-way ANOVA) for paired data. The test accepted the null hypothesis that the mean ranks for the DSC of the 4 methods with different sets of control points are similar with $\chi^2 = 3.45, d.f = 3, p < 0.03$.

The TRE values in Table 5.1 and Table 5.2 respectively do not follow a normal distribution. However, the log transformation of the raw data accepted the null hypothesis of normality of the data using Lilliefors test. The null hypothesis of the homoscedasticity of variances for the log-transformed data is also true when Bartlett's test ([10]) is used. A one-way ANOVA (Analysis of Variance) ([56]) is used to test the null hypothesis of similarity of means where the null hypothesis is accepted at 95% confidence level with $F = 5.08, d.f = 3, p = 0.0035$. Although, the ANOVA test accepted the null hypothesis, a Dunn's post test ([48]) is additionally performed to identify the dissimilarities in the TRE means of the methods M1, M2, M3 and NLTPS-REGCORR. The pairwise comparison test revealed that only M3 and NLTPS-REGCORR TRE means are siginificantly different with $p < 0.05$. Figure 5.14 shows the mean estimates of the TRE with their confidence intervals for the given methods. The figure depicts that the mean TRE of the proposed NLTPS-REGCORR is significantly different than M3 method (proposed method with no internal points).

5.5.5.2 Registration Methods

It is observed from Table 5.7 that the DSC and HD values for all the three methods (NLTPS-UNI, NLTPS-CORR and NLTPS-REGCORR) are similar. Therefore, a statistical analysis of the mean DSC and HD values is done separately for the aforementioned method leaving out TPS ([135]) and the B-splines ([137]) registration methods. Common data transformations could not scale the given DSC values of Table 5.2 into a normal distribution and hence, Lilliefors test used to verify the normality of the distribution rejected the null hypothesis. Consequently, Levene's test is used to verify the homogeneity of the variances for the three methods which accepted the null hypothesis. Since the measurements of DSC of Table 5.2 and HD of Table 5.3 are taken for the same samples over the methods (NLTPS-UNI, NLTPS-CORR and NLTPS-REGCORR), we used Friedman's test for paired data. The test rejected the null hypothesis that the mean ranks for the DSC and HD and values of the 3 methods are similar with $\chi^2 = 25.27, d.f = 2, p < 0.0001$ and $\chi^2 = 17.29, d.f = 2, p < 0.0001$ respectively. This signifies that at least one of the three methods differs in mean rank from the rest. Therefore, Dunn's post test is used for pairwise comparison between the methods to identify the dissimilarity. The test identified that the means of the DSC values for NLTPS-UNI and NLTPS-CORR are not statistically significantly different and those for NLTPS-UNI & NLTPS-REGCORR and NLTPS-CORR & NLTPS-REGCORR are statistically significantly different with $p < 0.001$ for both respectively. Similar statistical significances are observed for the means of HD values for the first three methods of Table 5.3.

Analyzing the TRE columns of Table 5.2 it is observed that a log transformation of the raw data could suitably scale the data into a normal distribution. Therefore, Bartlett's test is used to analyze the homoscedasticity of the variances that accepted the null hypothesis. The data sample sizes being different for the 5 methods (19 values for NLTPS-UNI & NLTPS-CORR and 20 values for the remaining methods), the Kruskal-Wallis test (non-parametric one-way ANOVA)([92]) is used to compare the means of the ranked log-transformed TRE values. The test rejected the hypothesis of equality of ranked means with $\chi^2 = 19.6, d.f = 4, p = 0.0006$, which signifies that at least one of the method has statistically significantly different mean TRE than the remaining. Consequently, the Dunn's post test is performed

to find the dissimilarity in the mean ranks of the TRE values. The test revealed that NLTPS-REGCORR (proposed method) has a statistically significantly different mean TRE than NLTPS-CORR and the B-splines registration methods with $p < 0.005$, while not so significantly different than NLTPS-UNI and TPS registration methods. Nevertheless, the analysis of raw data for the TRE columns in Table 5.2 show a $2-3$ times improvement in mean TRE for the proposed method than NLTPS-UNI and TPS. The TLE value of 0.15 ± 0.12 mm for NLTPS-REGCORR signifies a low repeatability error in identification of the anatomical targets by clinical experts. Figure 5.15 shows the box-plot obtained from the Kruskal-Wallis test for the ranked TRE values of the 5 registration methods. Figure 5.16 shows the pairwise comparisons of log-transformed TRE values for the different methods. The figure reveals that NLTPS-REGCORR has statistically significantly different mean TRE than NLTPS-CORR and B-splines.

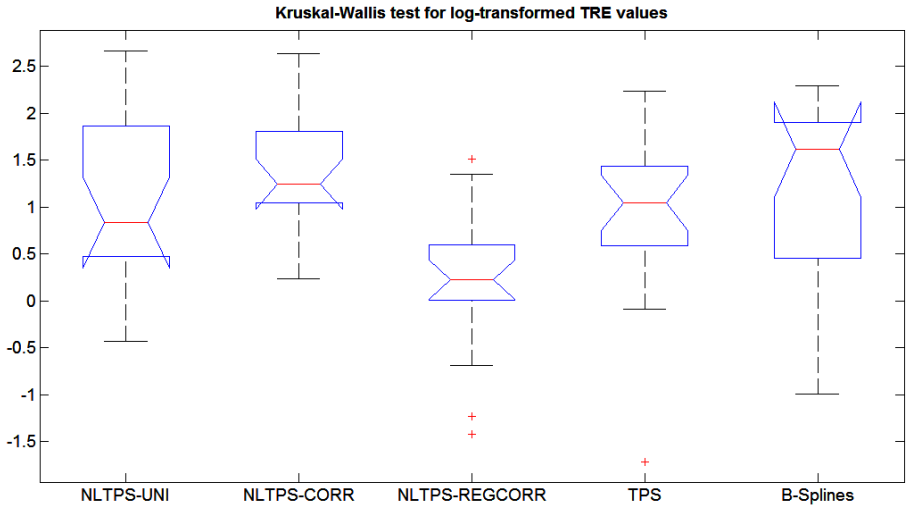

Figure 5.15: Kruskal-Wallis comparison of medians of ranked TRE values. Non-overlapping notches signify that the median values for the given methods are significantly different at 95% confidence level.

On analysis of the DSC data in Table 5.2 and HD data in Table 5.3 for NLTPS-REGCORR, TPS and B-Splines respectively, it is observed that the data do not follow a normal distribution and the data are heteroscedastic. Therefore, none of the classical statistical hypothesis testing method can be applied to compare the

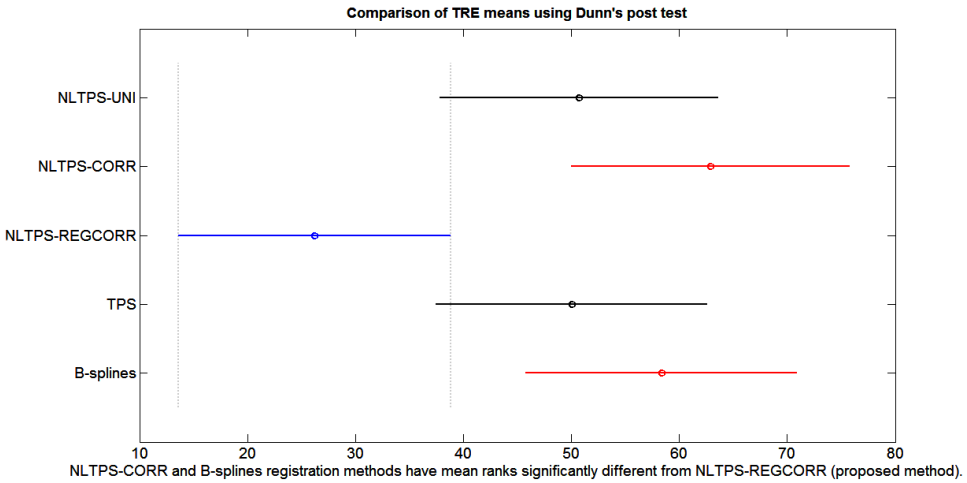

Figure 5.16: TRE means for different methods with significant difference between NLTPS-REGCORR (blue line) and NLTPS-CORR and B-splines (red lines).

means of the DSC and HD measures of the proposed method to that of the TPS and B-splines. However, the mean DSC and HD values of the proposed method are better than the TPS and B-splines methods.

5.5.5.3 Automatic Segmentation

The DSC values of Table 5.4 and the DSC values for patients 5–14 related to NLTPS-REGCORR in Table 5.2 follow a normal distribution with homogeneity of variances. Therefore, a two-tailed Student's t-test ([68]) is used to identify the similarity of the means of the DSC data for the proposed method with manual segmentation and the proposed method with automatic segmentation. The null hypothesis is accepted with $p < 0.01$ signifying that the mean DSC value obtained when automatic segmentation is employed is similar to that obtained with manual segmentation. However, for the HD values of the same set of patients as shown in Table 5.4 and Table 5.3 (HD column of NLTPS-REGCORR) need to be square-root transformed to be scaled into a normal distribution. Thereafter, the homoscedasticity of the data is determined and a two-tailed Student's t-test revealed statistically significant similar mean HD values with $p < 0.01$.

The log-transformed TRE data of Table 5.4 and those from TRE column of NLTPS-REGCORR for patients 5 – 14 of Table 5.2 show a normal distribution but

heterogeneity of variances. Therefore, a two-tailed Welch's t-test ([165]) is performed that accepted the null hypothesis signifying that the means of the log-transformed TRE of the methods compared are statistically significantly similar with $p < 0.01$.

5.6 Discussions

The statistical analysis in Section 5.5.5.1 of the DSC data in Table 5.1 for the methods with different sets of control points reveal that the mean DSC values for all the 3 methods and the proposed NLTPS-REGCORR in Table 5.2 are similar. However, the mean TRE of M3 (8 boundary points with no internal points) is significantly lower than the proposed method. This suggests that internal points are necessary to maintain clinically acceptable deformations of the prostate gland (as seen in Figure 5.9). Although methods M1 (6 boundary and 4 internal points) and M2 (10 boundary and 6 internal points) do not show statistically significantly different mean TRE values than NLTPS-REGCORR, the values are definitely higher than the proposed method that signify inaccurate local deformations.

The analysis in Section 5.5.5.2 of the data in Table 5.2 and Table 5.3 allow us to infer that the region overlap measures (DSC and HD) are slightly better for the methods NLTPS-UNI and NLTPS-CORR and inferior for traditional TPS and B-splines methods than those of NLTPS-REGCORR. However, the TRE values are low for the proposed method with high statistical significance when compared with NLTPS-CORR and B-splines registration methods. Although, the TRE values of TPS and NLTPS-UNI are not statistically significantly different than the proposed method, they are definitely $2-3$ times higher than NLTPS-REGCPRR. This signifies that the local deformations of the prostate gland anatomical structures (targets) are clinically acceptable as provided by the method NLTPS-REGCORR. The transformed MR images obtained as the results of the methods NLTPS-UNI and NLTPS-CORR (rows 3 and 4 of Figure 5.10) clearly illustrate the fact that the transformation of the gland anatomical structures are not acceptable for clinical procedures and may be verified quantitatively from the TRE value columns of NLTPS-UNI and NLTPS-CORR in Table 5.2 for the respective patients.

The possible reason for slightly improved region overlap measures with NLTPS-UNI and NLTPS-CORR compared to the proposed NLTPS-REGCORR is that the

non-linear TPS equations aim at minimizing the image differences of the TRUS and MR binary mask images. Therefore, the prostate boundaries are well aligned for NLTPS-UNI and NLTPS-CORR. On the contrary, NLTPS-REGCORR constrains the non-linear transformations with the additional term of regularized bending energy and correspondence localization errors. This results in smooth and clinically meaningful gray-level deformations of the gland anatomical structures in addition to a satisfactory prostate overlap of the transformed MR image with that of the TRUS. The global overlap measures shown in Table 5.2 and Table 5.3 when compared to those of the proposed method apparently indicate that our proposed method provides better prostate gland overlap than B-splines, although not significantly better than traditional TPS.

Considering the TRE measure to be more appropriate in evaluating registration accuracy, our method provides the least mean TRE with less than 3 mm (as suggested by the clinical experts) accuracy when compared to the traditional spline-based methods or the variations of the proposed method. Patient cases $1, 5, 15$ and 17 of Figure 5.11 (columns $1-3$ and $5-6$) reveal that the B-spline transformation (rows $5-6$) has significantly distorted the prostate gland, which are also reflected in the TRE values of the respective patient rows of Table 5.2. Although traditional TPS transformation (rows $3-4$) does not show any significant deformation of the prostate other than rugged transformations around the prostate edges as shown in Figure 5.11, the TRE values for the respective patients are higher than the proposed method as seen from Table 5.2. Therefore, the proposed method seems to provide better registration accuracies when compared with the other methods.

The analysis of the global and local registration accuracies in Table 5.4 and in Table 5.2 for patients $5-14$ shows that automatic segmentation does not significantly affect the registration accuracies compared to when manual segmentation is used. The example shown in Figure 5.12 also shows that there are significant overlaps between the manually and automatically segmented contours both in TRUS and MR images. Finally, the validation of the proposed registration method on the base and non mid-gland slices (Table 5.6) have shown high registration accuracies with < 3 mm average TRE for patients 6 and 7 respectively.

The average times required for the NLTPS-CORR and NLTPS-REGCORR methods are similar (see Table 5.3). However, the average time is slightly higher for

NLTPS-UNI considering 16 control points being used instead of 13 control points as in NLTPS-REGCORR. The complexity for the algorithms NLTPS-REGCORR and its variations (NLTPS-UNI and NLTPS-CORR) is $O(N + M)$, where, N and M are the number of foreground pixels for the fixed and the moving images respectively. The traditional TPS has the least average computation time, since the complexity $O(n)$ involves only the number of correspondences (n) across the fixed and moving images. However, it is to be noted that the implementation does not guarantee bijectivity of the TPS transformation and therefore suffers from distorted transformations in some cases e.g. see Figure 5.11 patients 5 and 15 (columns 2 and 5, rows 3 and 4 respectively). The B-splines method requires the maximum time for registration owing to evaluation of the image similarity measure (NMI) and following a multiresolution framework for 3 resolutions. Despite the use of a multiresolution framework, the traditional B-splines method fails to provide good registration accuracy in most cases. On the contrary, our proposed method does not follow any multiresolution framework; however, by the virtue of the non-linear polynomial functions, a smooth and bijective transformation is achieved. The computation time of the proposed algorithm being highly dependent on the number of image pixels can be parallelized and considering its unoptimized implementation in MATLAB, a speed-up of computation time is possible by C++/GPU programming.

5.7 Conclusions

A new non-linear diffeomorphic framework with TPS being the underlying transformation has been proposed to register prostate multimodal images. A method to establish point correspondences on a pair of TRUS and MR images has also been proposed that is based on the computation of Bhattacharyya distance for shape-context representations of contour points. The bijectivity of the diffeomorphism is maintained by integrating over a set of non-linear functions for both the fixed and transformed moving images. The regularized bending energy and the localization errors of the point correspondences established between the fixed and moving images have further been added to the system of non-linear equations added to the TPS constraints. This additional constraint ensured regularized deformations of the local anatomical structures inside the prostate that are meaningful for clinical interven-

tions like prostate biopsy. The performance of the proposed method has been compared against two variations of non-linear TPS transformations where the control points had been uniformly placed on a grid for the first and the control points were established using the proposed point correspondence method for the latter. Both these methods did not involve the regularization and only relied on the non-linear transformation functions. The results obtained on real patient datasets concluded that the overall performance of the proposed method in terms of global and local registration accuracies is better compared to the two variations as well as traditional TPS and B-splines based deformable registration methods, and therefore could be feasibly applied for prostate biopsy procedures. The proposed method has been validated against a varied number of control points that inferred that control points inside the prostate gland are necessary to maintain clinically meaningful deformations and that 8 boundary points capturing the inflexions of the prostate curve are optimally suitable than less or more boundary control points. The proposed method has been shown to be not affected by automatic segmentation inaccuracies owing to the robustness of the automatic segmentation method employed. Validation of the registration method on the base and non mid-gland slices has shown high global and local registration accuracies illustrating the robustness of the method.

The proposed non-linear TPS framework with regularization may be applied to 3D prostate volume registration. However, a slice-by-slice point correspondences may be established after resampling the prostate volumes. The TRUS-MR slice correspondences chosen manually in our experiment can also be chosen automatically with the use of an EM tracker attached to the TRUS probe that will provide the spatial position of the TRUS slice in a pre-acquired prostate TRUS/MR volume during the needle-biopsy. An automatic method based on information theory and statistical shape analysis to find the MR slice that closely corresponds to the TRUS axial slice is discussed in details in Chapter 7.

Chapter 6

Off-line Deformation Learning for Fast Multimodal Registration

In this chapter, we propose a method to learn deformation parameters off-line for fast multimodal registration of ultrasound and magnetic resonance prostate images during ultrasound guided needle biopsy. The method is based on a learning phase where deformation models are built from the deformation parameters of a spline-based non-linear diffeomorphism between training ultrasound and magnetic resonance prostate images using spectral clustering. Deformation models comprising of the eigen-modes of each cluster in a Gaussian space are applied on a test magnetic resonance image to register with the test ultrasound prostate image. The deformation model with the least registration error is finally chosen as the optimal model for deformable registration. The rationale behind modeling deformations is to achieve fast multimodal registration of prostate images while maintaining registration accuracies which is otherwise computationally expensive.

6.1 Introduction

As mentioned in Chapter 1 that the prostate of the same patient may exhibit deformations between the TRUS and the MR images. The deformations are caused by the insertion of the endorectal probe during the MR acquisition, bowel or gas inside the rectum and displacement of patient position between the TRUS and MR

imaging procedures. However, the deformation is mostly observed as flattening of the part of the prostate adjacent to the rectum. Therefore, in our work we attempt to model such deformations of the prostate from a set of corresponding MR images co-registered with the TRUS images. The deformable registration of the training set of TRUS and MR images is done using the method of Chapter 5, Section 5.3. However, instead of using 13 point correspondences as in Section 5.2, we employ the shape-context based method of Belongie et al. [14] and Bhattacharyya distance [20] to set 8 contour point correspondences across the TRUS and the MR prostate images and only the prostate centroids as the internal points. Reducing the number of control points from 13 to 8 firstly, speeds-up the training time; furthermore, it is shown in the results section of this chapter that reducing the number of internal points does not significantly affect the transformation.

The deformable registration in Section 5.3 is based on the solution of an overdetermined system of non-linear functions integrated over the segmented prostate regions in both the TRUS and MR. The MR image transformation employs a thin-plate spline (TPS) interpolation. The combination of TPS based interpolation and the set of polynomial functions ensures a smooth diffeomorphic transformation of the MR image at the cost of increased computation time. However, the MR images need to be registered with the TRUS images in near real time during prostate biopsy. Therefore, to achieve fast registration we propose to model the TPS weight parameters obtained from the diffeomorphic registration of training TRUS-MR images and then apply the modeled parameters to register a new set of TRUS-MR images. A single deformation model in Gaussian space derived from the principal eigen-modes of the deformation vectors as shown by [61] is not sufficient to model all the variations of prostate deformation. Therefore, we propose to cluster the deformation vectors into similar groups using a spectral clustering approach. The principal eigen-modes of the deformation vectors of each of these clusters in a Gaussian space form a deformation model. The registration of a test set of TRUS-MR images involves recovering the affine parameters from the established point correspondences and the TPS weight parameters of each of the deformation model are consecutively applied to deform the moving MR image. The model with the least registration error between the TRUS-MR images is chosen as the optimal deformation model.

6.2 Learning Prostate Deformations

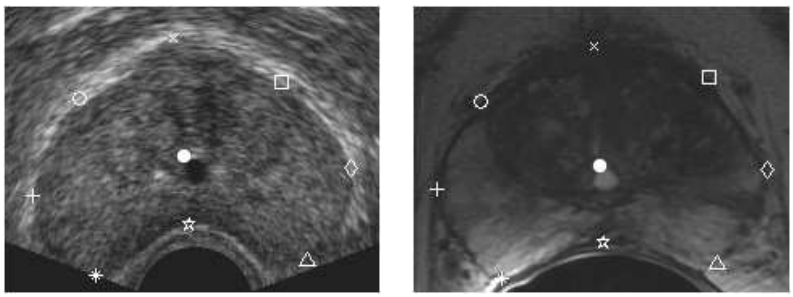

(a) (b)

Figure 6.1: Point correspondences example. (a) points in TRUS, (b) point correspondences of (a) in MR.

The proposed method is based on the following components:

1. Point correspondences established on both the TRUS and MR images that are required for both the training and testing phases,
2. the non-linear diffeomorphic framework required for deformation of the training MR images,
3. spectral clustering of TPS weight vectors during the training and
4. linear estimation of deformation parameters applied on the test MR image.

The point correspondences are established by the method as explained in Chapter 5, Section 5.2. However, unlike the previous method, only 8 correspondences on the boundary and 1 centroid are selected automatically. Figure 6.1 shows the sets of point correspondences across the TRUS and the MR images.

After the correspondences are established, the non-linear deformations of the training set of MR images are achieved by the method as described in Chapter 5, Section 5.3. However, since the number of point correspondences are less in this case, only 9×2 TPS weight parameters and 6 affine parameters need to be estimated. Therefore, only 36 equations generated from the $\omega(\cdot)$ function in Equation (5.16) are sufficient to obtain a stable solution, where $(a_k, b_k) \in \langle (0,0), (1,0), (0,1), \ldots, (5,5) \rangle$.

The spectral clustering of the TPS weight parameters to form deformation models and the application of the linear estimations of the deformation models to deform a new test MR image are described in subsequent subsections.

6.2.1 Spectral Clustering

The deformation parameters i.e. the TPS weight parameters obtained for the set of training fixed and moving images are grouped into similar deformation clusters by a spectral clustering approach that determines the number of clusters automatically. Since, the TPS weight parameters are essentially row vectors of length 9×2 for x- and y- directions, we firstly compute the resultant direction vector of size 9×1. Then the cosine similarities of $\mathcal{P}$ resultant deformation vectors $W_i = (w_1, w_2, \ldots, w_9), i = 1, \ldots, \mathcal{P}$ of the training set are used to construct a $\mathcal{P} \times \mathcal{P}$ similarity matrix $\mathcal{W}$. The objective is to determine k disjoint clusters and the algorithm may be defined in the following steps [118]:

1. Form the similarity matrix $\mathcal{W} \in \mathbb{R}^{\mathcal{P} \times \mathcal{P}}$, i.e. $\mathcal{W}_{ij} = \frac{W_i \cdot W_j}{\|W_i\| \|W_j\|}$, where, $\mathcal{W}_{ii} = 1$.
2. Define the degree matrix D as a diagonal matrix, where D_{ii} is the sum of elements of the $\mathcal{W}_i$ row.
3. Construct the normalized Laplacian L as $D^{-1/2} \mathcal{W} D^{-1/2}$.
4. Compute the first k eigenvectors of L to build the matrix $U \in \mathbb{R}^{\mathcal{P} \times k}$ by stacking the eigenvectors into columns.
5. Re-normalize the matrix U to V so that each row has unit-length, i.e. $V_{ij} = U_{ij} / (\sum_j U_{ij}^2)^{1/2}$
6. Treating each row of V as a point in $\mathbb{R}^k$, apply K-means clustering to re-normalized V matrix.

Finally the deformation vector W_i is now assigned to cluster j, iff the row V_i of the matrix V is assigned to cluster j. Likewise, k disjoint deformation clusters are formed. In this case, k is the number of largest eigen-vectors of matrix L that comprises of 88% of the total variations. The size of the training dataset being small, the choice of 88% energy ensures that more than one deformation vector is present in one cluster and avoids over fragmentation of the deformation vectors.

6.2.2 Linear Estimation

Geva et al. [61] showed an off-line linear estimation of basis functions from a deformation space. They performed a PCA of the coefficients of a bivariate B-splines transformation to represent them by their principal eigen-modes. Motivated by such method, given a test moving image we may also transform it by the linear estimation of the TPS deformation (weight) parameters as

$$w_{iv} = \sum_{s=1}^{N_s} a^s b_{iv}^s \tag{6.1}$$

where N_s is the number of principal axes on which the coefficients are projected after PCA, a^s and b_{iv}^s are the respective eigen-value and the eigen-vector. Therefore, the transformation $\varphi(\mathrm{x})$ of Equation (5.7) of Chapter 5 may be written as

$$\begin{aligned}\varphi_v(\mathrm{x}) &= a_{v1}x_1 + a_{v2}x_2 + a_{v3} \\ &\quad + \sum_{i=1}^{n}\sum_{s}^{N_s} a^s b_{iv}^s U(\|p_i^m - \mathrm{x}\|).\end{aligned} \tag{6.2}$$

The number of principal axes N_s for each deformation cluster k is determined by retaining 95% of the principal modes of variation. Additionally, to consider a Gaussian space of the projections on N_s principal axes, we also take into account the $-2\sigma, -1\sigma, 0\sigma, +1\sigma, +2\sigma$, variations of N_s principal components, where σ is the standard deviation. Therefore, $k \times 5$ deformation models are formed from the training set of deformation vectors. The affine parameters of the TPS transformation in Equation (6.2) are obtained by SSD minimization Equation (2.3) of the point correspondences established on the test moving and fixed images.

Finally to obtain the optimal transformation of the test moving image, the registration error is computed as the percentage of non-overlapping area γ (Equation (6.3)) in the prostate foregrounds of the fixed and the transformed moving images and the one with least registration error is considered as the final transformation.

$$\gamma = \frac{|\varphi(M(E)) \oplus F(E)|}{|M| + |F|} \cdot 100\% \tag{6.3}$$

where, E are the foreground pixels of the registered moving image M and the fixed

Table 6.1: Registration accuracies and computation time for different methods. HD and TRE are in (mm) and time is in seconds.

Methods	**NLTPS-REGCORR**	**DEF-NL**	**DEF-L**
DSC	0.98±0.004	0.978±0.010	0.927±0.25
HD	1.63±0.48	2.05±1.26	5.14±3.67
TRE	1.60±1.17	1.71±1.23	2.44±1.17
Time	113.77±23.43	106.34±32.45	4.99±3.52

image F.

6.3 Experiments and Results

The validation of our method is done using 25 patients axial mid-gland slices for both the TRUS and MR images with an average size of 249×219 pixels with each pixel dimension being 0.2734×0.2734 mm. A leave-one-out approach is used where the deformation models are formed from 24 datasets and are applied to transform the remaining one. The registration accuracy is evaluated in terms of DSC that measures the global overlap of the prostate regions, 95% HD that measures the contour accuracy and TRE that measures the extent of overlap of the anatomical targets in the transformed MR image and the TRUS image. Table 6.1 shows the registration accuracies for the method NLTPS-REGCORR as described in Chapter 5 with 20 patient datasets, the NLTPS-REGCORR method on 9 point correspondences without deformation learning abbreviated as DEF-NL, and the deformation estimation (DEF-L) i.e. non-linear deformation applied to a set of training TRUS-MR images, spectral clustering to group deformations and thereby applying linearly estimated deformation parameters to transform a test moving MR for 25 datasets in a leave-one-out framework.

It is to be noted in Table. 6.1 that the method NLTPS-REGCORR using 13 correspondences needs more computation time than DEF-NL i.e. our proposed method with 9 point correspondences only. However, the registration accuracies of DEF-NL are comparable to that of NLTPS-REGCORR. The area and contour overlap accuracies in terms of DSC and HD for our method without the deformation learning approach are statistically significantly better with Student's t-test $p < 0.0001$ and $p < 0.001$ respectively than that with the deformation learning. The TRE for our

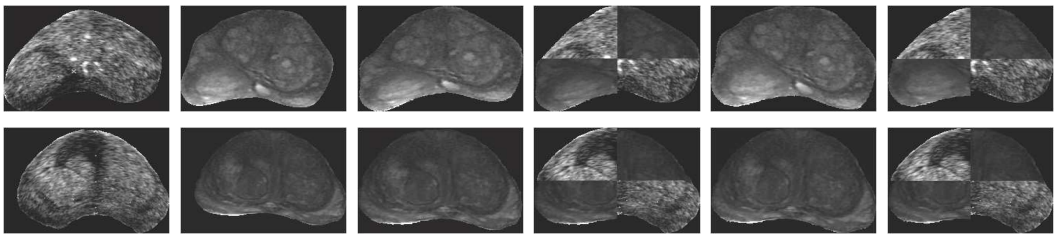

Figure 6.2: Qualitative registration results. The first two columns show the fixed TRUS and the moving MR images respectively. The 3^{rd} and the 4^{th} columns show the registration results for the proposed method without the deformation learning and the remaining columns show the results with the deformation learning.

method without the deformation learning approach is also slightly better than that with the deformation learning with a statistical significance of $p < 0.005$. Nevertheless, the computation time of our method with deformation learning shows a statistically significant reduction with $p < 0.0001$ than the remaining methods. Fig. 6.2 shows the registration results for 2 patients, where it is observed that our method with and without deformation learning produce similar results. The accuracy of our method is qualitatively comparable with that of Xu et al. [168] that demonstrates a near real-time TRUS-MR prostate fusion method with an average registration error of 2.3 ± 0.9 mm but requires 15 seconds for the registration process. Our method was implemented in MATLAB 2009(b) with 1.66GHz processor and 2GB memory. The method shows a significant speed-up of computation time when the off-line deformation learning approach is employed while maintaining a clinically significant average target registration error of < 2.87mm.

6.4 Conclusions

A method of deformable registration between TRUS and MR prostate images with prior learning of deformation parameters has been proposed in this chapter. Spectral clustering has been used to group similar deformations from training TRUS-MR images and thereafter the eigen-modes of deformations for each deformation cluster in a Gaussian space have been used to deform a new MR image corresponding to the TRUS image. The method is fast and efficient to transform a moving image with good registration accuracy and may be used during prostate biopsy if programmed

on GPU. The accuracy of resulting deformation may be further increased if more patient sets are used to learn the deformation parameters.

Chapter 7

2D TRUS-MRI Slice Correspondence for Prostate Biopsy

This chapter presents a novel method to identify the 2D axial MR slice from a pre-acquired MR prostate volume that closely corresponds to the 2D axial TRUS slice obtained during prostate biopsy. The method combines both shape and image intensity information. The segmented prostate contours in both the imaging modalities are described by shape-context representations and matched using the Chi-square distance. NMI and CC between the TRUS and MR slices are computed to find image similarities. Finally, the joint probability values comprising shape and image similarities are used in a rule-based framework to provide the MR slice that closely resembles the TRUS slice acquired during the biopsy procedure.

7.1 Introduction

Fusion of pre-biopsy MR on interventional TRUS may be done in several ways. An Electro Magnetic (EM) tracker attached to the 2D TRUS probe may be used that sweeps the prostate to reconstruct a 3D TRUS volume. The 3D TRUS volume is then fused with the MR volume to obtain the spatial position of the 2D TRUS slice during biopsy within the pre-biopsy MR volume [168]. On the other hand, a 3D

TRUS probe may be directly used to acquire 3D TRUS volume and a volume-volume registration may be performed [12]. However, neither a 3D TRUS probe is commonly available in diagnostic centers nor the use of the EM tracker is an established clinical practice. Therefore, intending to solve the 2D TRUS-MR slice correspondence problem, we propose a method based on Chi-square distance of shape-context representations of the prostate contours and image similarity measures like NMI and CC of the TRUS-MR slices. The probability of an MR slice being the correct match for the corresponding TRUS slice is determined from the joint probabilities of shape similarity and each of the image similarity measures (NMI and CC) yielding two sets of probability values. The shape and image similarities assume independence, therefore multiplication of the same provides the combined probability. The slice having the maximum joint probability among the obtained sets of probability values is normally chosen as the correct match. However, owing to the segmentation inaccuracies and inter-modality prostate deformations, the overlap area between the TRUS and MR images will differ in the sense that it would incorporate some error in the image-based similarity and hence in the choice of the correct MR slice from joint shape and image similarities. Therefore, a rule-based approach is adopted to prioritize the shape similarity in such cases over image similarities.

The novelties of the proposed method may be summarized as follows:

1. Using shape context representations of the contours to find prostate shape similarities between TRUS and MR slices.

2. Combining shape information (here shape context) with image intensity information (NMI and CC), thereby yielding the combined probability of an MR slice that closely resembles the TRUS slice both in shape and intensity spaces.

3. Rule-based approach to prioritize the shape similarity in case of ambiguous maximum joint probability values of shape and image similarities.

7.2 The Slice Correspondence Method

The prostate is manually segmented from the 2D TRUS axial slice and the pre-biopsy axial MR volume where the TRUS slices are considered to be parallel to the

MR axial plane. The manual segmentation ensures better evaluation of our method, although in future we will use the fast automatic prostate segmentation methods in both MR and US modalities by Ghose et al. [63, 64]. The shape similarity measure using Chi-square distance is explained in section 7.2.1, the use of image similarities (NMI and CC) are explained in section 7.2.2 and the explanation of joint shape and image similarities with the rule-based approach to choose the best matching MR slice corresponding to the axial TRUS slice are in section 7.2.3.

7.2.1 Shape Similarity

The first part of establishing a shape similarity measure across the segmented prostate images in the TRUS and the MR involves establishing point correspondences on the prostate contours of the TRUS slice and all the MR slices in the respective volume. The point correspondences are established using the same method of shape-contexts and Bhattacharyya distance as discussed in Chapter 5, Section 5.2. However, instead of establishing only 8 points on the contour, we establish many points depending on the number of uniformly-sampled points on the TRUS contour.

After the corresponding points are identified, the Chi-square (χ^2) distances between the TRUS slice and each of the MR slices are calculated based on the corresponding shape-context histograms of the point correspondences and is given by $\mathcal{C}_{ij}$ as

$$\mathcal{C}_{ij} = \frac{1}{2}\sum_{k=1}^{5}\sum_{\theta=1}^{12}\frac{(\hat{h}_i(k,\theta) - \hat{h}'_j(k,\theta))^2}{\hat{h}_i(k,\theta) + \hat{h}'_j(k,\theta)}. \tag{7.1}$$

The final distance is the sum of all the χ^2 distances of the corresponding points (shape-context histograms) in TRUS and MR and is given by $\mathcal{H}$ as

$$\mathcal{H} = \sum_{i=1}^{l}\mathcal{C}_{ij}, \tag{7.2}$$

where, $\hat{h}_i(k,\theta)$ and $\hat{h}'_j(k,\theta)$ are the normalized shape-context histograms of the TRUS and the MR images respectively, and l is the number of point correspondences. The TRUS-MR slice pair with minimum sum of χ^2 distance i.e. $\mathcal{H}$ is identified and

its significance will be discussed in the following subsection.

7.2.2 Image Similarities

Image similarity measures have been extensively used in multimodal image registration problem to ensure that the moving image is transformed with close resemblance to the fixed image. Our problem is to find an MR slice in the volume that closely resembles the TRUS slice. Therefore, to find such similarity we employ the well-known NMI and CC as image similarity measures. Fei et al. [53] demonstrated that CC is more discriminative as an image similarity in low resolutions and NMI at higher resolutions for registration problems. Related to our problem, some TRUS slices have smaller prostate sizes than the other. Therefore, considering the variability in prostate sizes we decided to use both NMI and CC as image similarity measures.

The TRUS-MR slice pair identified with the minimum $\mathcal{H}$ as obtained from Equation (7.2) is used to retrieve the 2D rigid transformation (in-plane rotation and translation) parameters between them; and the remaining MR slices in the volume are rigidly registered with the TRUS slice using the same transformation parameters. This registration step ensures similar 2D in-plane rigid alignment of all the MR slices of the volume with the 2D TRUS slice. After the alignment of the MR volume with the TRUS slice, pairwise NMI and CC are computed for each MR-TRUS slice pair. The NMI and CC are computed according to the Equation (2.8) and Equation (2.4) as given in Chapter 2.

7.2.3 Choosing the Best Matching MR Slice

The MR slice corresponding to the observed TRUS slice should ideally be the one with lowest $\mathcal{H}$ obtained from Section 7.2.1 and with maximized NMI or CC as obtained from Section 7.2.2. The values of these statistical shape and image similarity measures are consecutively transformed into probability density functions (pdfs) to compute the joint probability.

Given a set of independent random variables $\mathbf{X} = \{\mathbf{x}_1 \dots \mathbf{x}_n\}$, each defined by the pdf $p(\mathbf{x}_i)$, $i = 1 \dots n$, the joint probability of the independent random variables is

given by

$$p(\mathbf{X} = \mathbf{x}_1, \ldots \mathbf{X} = \mathbf{x}_n) = p(\mathbf{X} = \mathbf{x}_1) \cdot \ldots \cdot p(\mathbf{X} = \mathbf{x}_n) \tag{7.3}$$

In this work, the set of independent random variables is $\mathbf{X} = \{\mathcal{H}', \text{NMI}, \text{CC}\}$, where $\mathcal{H}' = 1 - \mathcal{H}$ and their respective probability values constituting the pdfs. Therefore, two sets of joint probability values are obtained by combining the shape and image similarities as

$$\begin{aligned} P_{\text{NMI}} &= p(\mathbf{X} = \mathcal{H}', \mathbf{X} = \text{NMI}) = p(\mathbf{X} = \mathcal{H}') \cdot p(\mathbf{X} = \text{NMI}) \\ P_{\text{CC}} &= p(\mathbf{X} = \mathcal{H}', \mathbf{X} = \text{CC}) = p(\mathbf{X} = \mathcal{H}') \cdot p(\mathbf{X} = \text{CC}) \end{aligned} \tag{7.4}$$

After obtaining the joint probabilities, the idea is to find the MR slice that corresponds to the TRUS slice jointly maximizing the $\mathcal{H}'$ and NMI or $\mathcal{H}'$ and CC. Let us consider the maximum joint probabilities of P_{NMI} and P_{CC} be P_{NMI}^{max} and P_{CC}^{max} respectively. Then the rule-based method to identify the best MR slice is given in Algorithm 2 as

Algorithm 2 The rule to choose the best MR slice

if $|P_{\text{NMI}}^{max} - P_{\text{CC}}^{max}| > \lambda$ **then**
  Choice = MR slice corresponding to $\max(P_{\text{NMI}}^{max}, P_{\text{CC}}^{max})$
else
  Choice = MR slice corresponding to the maximum value of $\mathcal{H}'$
end if

The value of λ is determined through the experimental validation procedure. If P_{NMI}^{max} and P_{CC}^{max} both have closely separated values then it is difficult to bias on any one of the joint probability (P_{NMI}^{max} or P_{CC}^{max}) to determine the best matching MR slice. Therefore, in such cases the shape similarity measure is prioritized in determining the slice choice.

7.3 Results and Discussions

The results are validated against the MR slice choices obtained from an expert radiologist and an expert urologist for 20 patients axial mid-gland TRUS slices.

Table 7.1: Expert choices and the results for the MR slices corresponding to a TRUS slice obtained by our method. Agr. is the abbreviation used for Agreements. The matched cases are shown in bold.

Patients/ MR Slice	1	2	3	4	5	6	7	8	9	10	11	12	13	14	15	16	17	18	19	20	**Agr.(%)**
Expert 1	6	**8**	9	7	6	10	**6**	10	5	7	**6**	**5**	12	**8**	**6**	5	7	7	**6**	7	**65%**
Expert 2	2	7	6	5	6	**9**	**6**	**8**	**7**	**6**	**6**	4	**13**	**8**	**4**	**8**	**10**	9	**6**	7	**80%**
Our method	3	**8**	3	6	5	**9**	**6**	**8**	**7**	**6**	**6**	**5**	**13**	**8**	**6**	**8**	**10**	6	**6**	4	-

The axial MR slices have slice thickness of 3 mm with inter-slice gap of 3.5 mm where the pixel dimension is 0.2734 mm × 0.2734 mm. The value of λ is determined experimentally as 0.15 that is the value which maximizes the number of cases in agreement to that of the expert choices. This means that if the maximum joint probability values P_{NMI}^{max} and P_{CC}^{max} are similar by more than 85% then the slice choice is dependent only on the maximum shape similarity rather than joint image and shape similarities. Table 7.1 shows the choices of the axial MR slice corresponding to an axial TRUS slice provided by the experts (independently) and the results we obtained using our method. The inter-slice gap being 3.5 mm, we have considered the $[-1, +1]$ slices i.e. a statistically significant 20% error when computing the inter-expert and between expert and our method accuracies of slice choice.

It is observed from Table 7.1 that the automatic MR slice choice matched at least one of the expert choices for 18 cases wherein the experts agree in their choices for 11 patient cases (patients $2, 5, 6, 7, 10, 11, 12, 13, 14, 19$ & 20). The expert choices matched exactly in 6 cases ($5, 7, 11, 14, 19$ & 20) out of which our result matched exactly for 4 patient cases ($7, 11, 14$ & 19) and -1 slice away for patient 5 respectively. Since, the expert choices agreed exactly and $[-1, +1]$ slice away in 11 out of 20 cases, they are in agreement of 55%.

Comparing each of the expert choices independently with our method, the exact matches with expert 1 are for 7 patients ($2, 7, 11, 12, 14, 15$ & 19) while $[-1, +1]$ slice away for 6 patients ($4, 5, 6, 10, 13,$ & 18). Therefore, 13 out of 20 cases i.e. 65% results are in agreement with that of the choices of expert 1. Similarly for 11 cases ($6, 7, 8, 9, 10, 11, 13, 14, 16, 17$ & 19) our results exactly matched expert 2 choices and are $[-1, +1]$ slice away for 5 patient cases ($1, 2, 4, 5,$ & 12). This signifies that the results of our method are in 80% agreement with that of expert 2 slice choices. The

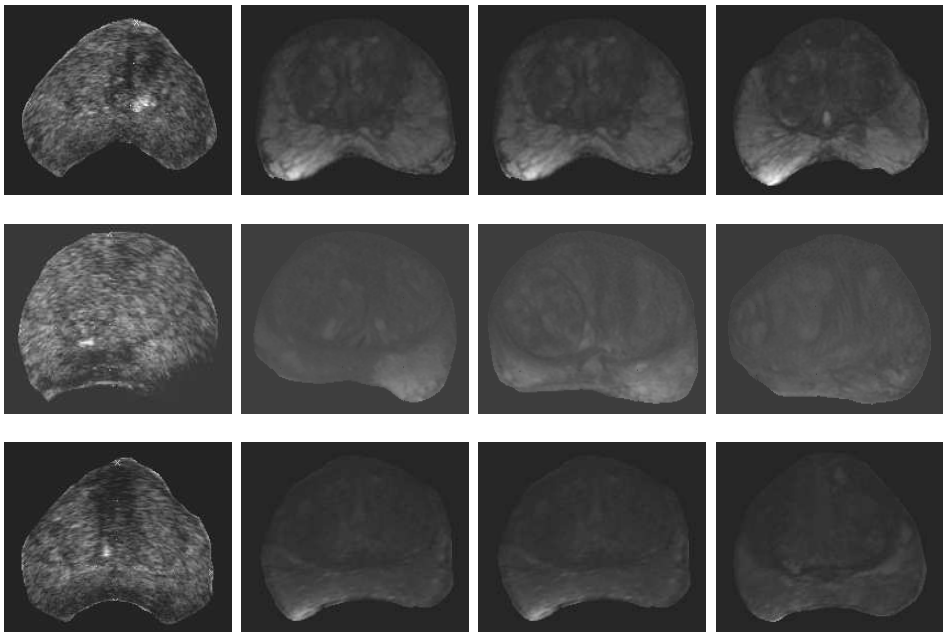

Figure 7.1: TRUS-MR corresponding slices. Rows (top to bottom) show patient cases $5, 3$ and 20 respectively. The 1^{st} column shows the TRUS slices, the 2^{nd} and the 3^{rd} show the expert 1 and 2 MR slice choices respectively and the last column shows the obtained result using our method.

agreements between our method and each of the expert choices are shown in the last column of Table 7.1. The inter-expert variability in the choice of MR slice being high (55% agreement), our method performs better with an agreement of 65% for expert 1 that shows a 18.18% increase in performance and with 80% agreement for expert 2 that shows an increase in performance by 45%. The overall performance of our method is said to be 90% considering accurate slice matches in 18 out of 20 cases while failing for patient 3 and 20. Figure 7.1 shows patient case 5 where the result obtained is one slice below than that of the choices of experts 1 and 2 as shown in Table 7.1. Figure 7.1 also shows patient cases 3 and 20 where the results are not close to any of the expert choices. However, observing the slice choice by our method and that of the expert for patient 20 it may be noted that both the choices are visually similar.

The method has been implemented in MATLAB and the complete process takes 3 secs on an average to find out the corresponding MR slice from a set of $12 - 14$ slices. It is to be noted that Xu et al. [168] employed an EM tracker to locate

the spatial position of the 2D TRUS slice (during biopsy) in the 3D TRUS volume. Thereafter, to compensate for the prostate motion, the sum-of-squared differences (SSD) between the maximum translational and rotational TRUS slices within a short time frame of the biopsy and the corresponding spatial 2D TRUS slices obtained in the 3D TRUS volume was minimized. Similarly, considering an error of $[-1, +1]$ slices from the actual MR slice, we can directly use the slice obtained by our proposed method for multimodal registration between TRUS and MR employing the method NLTPS-REGCORR in Chapter 5, Section 5.3. However, if an EM tracker is additionally attached to the TRUS probe during biopsy, then it would be possible to locate an approximate position of the TRUS slice in MR volume. Consequently, our method can be employed to search for the best slice within a smaller subset in the neighborhood of the correct MR slice thereby improving on the accuracy of slice choice.

7.4 Conclusions

A method to find out 2D MR slice correspondence of a 2D axial TRUS slice during biopsy has been reported in this chapter. The method is based on statistical shape and image similarity measures and their joint probabilities and applying a rule-based method to prioritize the shape similarity in certain cases. The method is fast in finding out MR correspondences that are nearly the same as the choices obtained from two experts. Since EM tracker is not easily available in hospitals in Europe and 3D TRUS is normally not employed for biopsy purposes, our proposed method may provide a good starting point for multimodal fusion of TRUS-MR images to improve the sampling of biopsy tissues. Although the results reported in this paper are validated only for mid-gland or close to mid-gland axial slices, the validations for the base/apex TRUS axial slices, TRUS sagittal slices and cross-validation of our method with the use of an EM tracker have been left as future works.

Chapter 8

Conclusions

In this thesis, we investigated algorithms to spatially align 2D inter-operative TRUS and pre-operative MR prostate images. This alignment is particularly challenging, when two different modalities are involved and non-linear geometric transformations are required to cope with the soft-tissue deformations.

In Chapter 2 we provided the theoretical background of image registration and Chapter 3 provided an extensive review on the existing methods related to prostate multimodal registration. The analysis of this chapter led to the consensus that radial-basis transformations provided more registration accuracies when dealing with TRUS and MR prostate images. Therefore, in Chapter 4, a detailed investigation on commonly used radial-basis transformation has been made. A geometric method to establish point correspondences across the TRUS and MR images has been proposed that was used to drive the TPS spline transformation. A variant of B-spline based free-form deformation was also proposed that involved computation of the NMI from images transformed by amplitude responses of directional quadrature filters. A comparison between the traditional B-splines (with NMI from raw-intensity images), the variant of the B-splines and the traditional TPS allowed to conclude that registration accuracy in terms of tumor localization may be improved if NMI is computed from transformed images to drive the B-splines transformations rather than NMI computed from raw-intensity images. However, TPS provided a higher contour accuracy compared to the variant of B-splines transformation.

The search for a registration method that provided high global and local registra-

tion accuracies for prostate biopsy, motivated us to propose the new diffeomorphic non-linear TPS-based registration in Chapter 5. A new method to establish point correspondences was also proposed that relied on statistical shape measures. Several experimental results concluded on the optimal number of point correspondences required to achieve good registration accuracy. The registration parameters were estimated from the solution of an over-determined system of non-linear equations with TPS as the underlying transformation. The additional constraint as the localization error of the point correspondences with the regularization of the TPS bending energy in the registration framework ensured high contour overlap as well as improved tumor localization.

In Chapter 6 we sought to minimize the computational complexity of the proposed diffeomorphic registration framework of Chapter 5 and proposed a method to learn the TPS deformation parameters offline from a set of training TRUS-MR prostate images. Since, all the deformations could not be accommodated in a single group, a spectral clustering approach was introduced that separated deformations into disjoint clusters. Linear estimations of deformation clusters in their Gaussian space were then applied to deform an unseen moving MR images using TPS transformation. While the affine parameters were estimated from the point correspondences established on the test TRUS-MR images. The method exhibited a statistically significant speed-up in computation while not compromising on the registration accuracies to larger extents.

Finally, we attempted to provide a solution to the unavailability of an EM tracker and 3D TRUS for biopsy procedure by proposing an automatic method to search for the best pre-operative axial MR slice match to the corresponding inter-operative axial TRUS slice. The method based on joint shape and image similarities provided better results than the consensus of two human experts.

Future Research

It is to be noted that in this thesis, we primarily focused on 2D transformations due to unavailability of 3D TRUS data. Therefore, we concentrated on the investigation of algorithms that can be applied for 2D cases, specifically TPS. We need to investigate more on intensity-based transformations like demons registrations and

finite-element model transformations when 3D data is available.

A major challenge in the current thesis is finding the MR slices corresponding to the TRUS biopsy slice without the employment EM tracker or 3D TRUS. Therefore, we need to validate our proposed method of slice correspondence and that of the non-linear diffeomorphic registration in conjunction to the use of the EM tracker. The proposed methods can be parallelized if programmed on GPU and therefore may be useful for real-time multimodal fusion of prostate images during biopsy. For improved biopsy sampling we also intend to develop a method to fuse preoperative MRS with interoperative TRUS images.

In offline learning of deformation vectors we need more training TRUS-MR data to accommodate the variations of prostate deformations. Also in the spectral clustering approach we used simple k-means approach where the effect of other methods like fuzzy C-means, mean-shift would be worth evaluation.

Publications

Journals

- "A spline-based non-linear diffeomorphism for multimodal prostate registration", J. Mitra, Z. Kato, R. Martí, A. Oliver, X. Lladó, D. Sidibé, S. Ghose, J. C. Vilanova, J. Comet, F. Meriaudeau, *Medical Image Analysis* , In Press, http://dx.doi.org/10.1016/j.media.2012.04.006, May 2012.

- "Prostate multimodality image registration based on B-splines and quadrature local energy", Jhimli Mitra, Robert Martí, Arnau Oliver, Xavier Lladó, Soumya Ghose, Joan C. Vilanova, Fabrice Meriaudeau, *International Journal of Computer Assisted Radiology and Surgery*, vol. 7, pp. 445-454, Heidelberg, Germany, Springer-Verlag, May 2012.

International Conferences

- "Spectral clustering to model deformations for fast multimodal prostate registration", J. Mitra, Z. Kato, S. Ghose, D. Sidibé, R. Martí, X. Lladó, A. Oliver, J. C. Vilanova, F. Meriaudeau, IAPR International Conference on Pattern Recognition (ICPR), to appear, Tsukuba, Japan, November 2012.

- "Joint Probability of Shape and Image Similarities to Retrieve 2D TRUS-MR Slice Correspondence for Prostate Biopsy", J. Mitra, S. Ghose, D. Sidibé, R. Martí, A. Oliver, X. Lladó, J. C. Vilanova, J. Comet, F. Meriaudeau, IEEE Engineering in Medicine and Biology Society (EMBS) Conference, to appear, San Diego, California, USA, Sep-Oct, 2012.

- "Weighted Likelihood Function of Multiple Statistical Parameters to Retrieve 2D TRUS-MR Slice Correspondence for Prostate Biopsy", J. Mitra, S. Ghose, D. Sidibé, A. Oliver, R. Martí, X. Lladó, J. C. Vilanova, J. Comet, F. Meriaudeau, International Conference on Image Processing (ICIP), to appear, Orlando, Florida, USA, September 2012.

- "A shape-based statistical method to retrieve 2D TRUS-MR slice correspondence for prostate biopsy", J. Mitra, A. Srikantha, D. Sidibé, R. Martí, A. Oliver, X. Lladó, S. Ghose, J. C. Vilanova, J. Comet and F. Meriaudeau, Proc. of SPIE Medical Imaging: Image Processing, vol. 8314, pp. 83143M-1-9, San Diego, California, February 2012.

- "A Non-linear Diffeomorphic Framework for Prostate Multimodal Registration", J. Mitra, Z. Kato, F. Meriaudeau, R. Martí, A. Oliver, X. Lladó, S. Ghose, J. C. Vilanova, Proc. of International Conference on Digital Image Computing: Techniques and Applications (DICTA), pp.31-36, Noosa, Australia, December 2011.

- "Quadrature Filter Enhanced B-spline registration applied to prostate multimodal images", J. Mitra, R. Martí, A. Oliver, X. Lladó, S. Ghose, J. C. Vilanova, F. Meriaudeau, Proc. of Computer Assisted Radiology and Surgery (CARS), vol. 6 (supplement 1) pp. S323-S324, Berlin, Germany, June 2011.

- "A comparison of thin-plate splines with automatic correspondences and b-splines with uniform grids for multimodal prostate registration", J. Mitra, R. Martí, A. Oliver, X. Lladó, J. C. Vilanova, and F. Meriaudeau, SPIE Medical Imaging, vol. 7964, pp. 79642T-1-8, Lake Buena Vista, Orlando, Florida, February 2011.

- "Multimodal prostate registration using thin-plate splines from automatic correspondences", J. Mitra, A. Oliver, R. Martí, X. Lladó, J. C. Vilanova, and F. Meriadeau, Proc. of International Conference on Digital Image Computing: Techniques and Applications (DICTA), pp. 587-592, Sydney, Australia, December 2010.

- "A thin-plate spline based multimodal prostate registration with optimal correspondences", J. Mitra, A. Oliver, R. Martí, X. Lladó, J. C. Vilanova, and F. Meriaudeau, Proc. of International Conference on Signal-Image Technology & Internet-Based Systems (SITIS), pp. 7-11, Kuala Lumpur, Malaysia, December 2010.

Other Related Publications

Journals and conferences co-authored.

Journal

- "Statistical shape and texture model of quadrature phase information for prostate segmentation", Soumya Ghose, Arnau Oliver, Robert Martí, Xavier Lladó, Jordi Freixenet, Jhimli Mitra, Joan C. Vilanova, Josep Comet, Fabrice Meriaudeau, *International Journal of Computer Assisted Radiology and Surgery*, vol. 7, issue 1, pp.43-55, Heidelberg, Germany, Springer-Verlag, January 2012.

- "A Survey of Prostate Segmentation Methodologies in Ultrasound, Magnetic Resonance and Computed Tomography Images", Soumya Ghose, Arnau Oliver, Robert Martí, Xavier Lladó, Jordi Freixenet, Jhimli Mitra, Joan C. Vilanova, Désiré Sidibé, Fabrice Meriaudeau, *Computer Methods and Programs in Biomedicine* , In Press, http://dx.doi.org/10.1016/j.cmpb.2012.04.006, June 2012.

International Conferences

- "Graph Cut Energy Minimization in a Probabilistic Learning Framework for 3D Prostate Segmentation in MRI", S. Ghose, J. Mitra, A. Oliver, R. Martí, X. Lladó, J. Freixenet, J. C. Vilanova, D. Sidibé, F. Meriaudeau, IAPR International Conference on Pattern Recognition (ICPR), to appear, Tsukuba, Japan, November 2012.

- "A Mumford-Shah Functional based Variational Model with Contour, Shape, and Probability Prior information for Prostate Segmentation", S. Ghose, J. Mitra, A. Oliver, R. Martí, X. Lladó, J. Freixenet, J. C. Vilanova, J. Comet, D. Sidibé, F. Meriaudeau, IAPR International Conference on Pattern Recognition (ICPR), to appear, Tsukuba, Japan, November 2012.

- "A Supervised Learning Framework for Automatic Prostate Segmentation in TransRectal Ultrasound Images", S. Ghose, J. Mitra, A. Oliver, R. Martí, X. Lladó, J. Freixenet, J. C. Vilanova, J. Comet, D. Sidibé, F. Meriaudeau, Advanced Concepts for Intelligent Vision Systems (ACIVS), to appear, Brno, Czech Republic, September 2012.

- "Spectral Clustering of Shape and Probability Prior Models for Automatic Prostate Segmentation in Ultrasound Images", S. Ghose, J. Mitra, A. Oliver, R. Martí, X. Lladó, J. Freixenet, J. C. Vilanova, J. Comet, D. Sidibé, F. Meriaudeau, IEEE Engineering in Medicine and Biology Society (EMBS) Conference, to appear, San Diego, California, USA, Sep-Oct, 2012.

- "A Coupled Schema of Probabilistic Atlas and Statistical Shape and Appearance Model for 3D Prostate Segmentation in MR Images", S. Ghose, J. Mitra, A. Oliver, R. Martí, X. Lladó, J. Freixenet, J. C. Vilanova, D. Sidibé, F. Meriaudeau, International Conference on Image Processing (ICIP), to appear, Orlando, Florida, USA, September 2012.

- "A hybrid framework of multiple active appearance models and global registration for 3D prostate segmentation in MRI", S. Ghose, A. Oliver, R. Martí, X. Lladó, J. Freixenet, J. Mitra, J. C. Vilanova, J. Comet, and F. Meriaudeau, SPIE Conference on Medical Imaging: Image Processing, vol. 8314, pp. 83140S-1-9, San Diego, California, February 2012.

- "Statistical shape and probability prior model for automatic prostate segmentation", S. Ghose, A. Oliver, R. Martí, X. Lladó, J. Freixenet, J. Mitra, J. C. Vilanova, J. Comet, and F. Meriaudeau, Proc. of International Conference on Digital Image Computing: Techniques and Applications (DICTA), pp.340-345, Noosa, Australia, December 2011.

- "Multiple mean models of statistical shapes and probability priors for automatic prostate segmentation", Soumya Ghose, Arnau Oliver, Robert Martí, Xavier Lladó, Jordi Freixenet, Jhimli Mitra, Joan C. Vilanova, Josep Comet, Fabrice Meriaudeau, MICCAI Workshop on Prostate Cancer Imaging: Computer Aided Diagnosis, Prognosis, and Intervention, vol. 6963, pp. 35-46, Toronto, Canada, Springer Lecture Notes in Computer Science, September 2011.

- "Quadrature phase-based statistical shape and appearance for prostate segmentation", S. Ghose, A. Oliver, R. Martí, X. Lladó, J. Freixenet, J. Mitra, J. C. Vilanova, F. Meriaudeau, Proc. of CARS 2011, vol. 6 (supplement 1), pp. S12-16, Berlin, Germany, June 2011.

Bibliography

[1] T. Aach, A. Kaup, and R. Mester. On texture analysis: Local energy transforms versus quadrature filters. *Signal Processing*, 45:173–181, 1995.

[2] R. Alterovitz, K. Goldberg, J. Kurhanewicz, J. Pouliot, and I.-C. Hsu. Image registration for prostate MR spectroscopy using biomechanical modeling and optimization of force and stiffness parameters. In *Proc. of 26th Annual Int. Conf. of the IEEE Engineering in Medicine and Biology Society (EMBS)*, volume 3, pages 1722–1725, San Francisco, CA, USA, 2004.

[3] R. Alterovitz, K. Goldberg, J. Pouliot, I.-C. Hsu, Y. Kim, S. M. Noworolski, and J. Kurhanewicz. Registration of MR prostate images with biomechanical modeling and nonlinear parameter estimation. *Medical Physics*, 33(2):446–454, February 2006.

[4] D. Amsellem-Ouazana, P. Younes, S. Conquy, M. Peyromaure, T. Flam, B. Debré, and M. Zerbib. Negative prostatic biopsies in patients with a high risk of prostate cancer. is the combination of endorectal MRI and magnetic resonance spectroscopy imaging (MRSI) a useful tool? a preliminary study. *European Urology*, 47:582–586, 2005.

[5] M. Andersson and H. Knutsson. Adaptive filtering. http://www.imt.liu.se/edu/courses/TBMI02, 2010. Accessed 29th June, 2012.

[6] G. L. Andriole, E. D. Crawford, R. L. Grubb, S. S. Buys, D. Chia, T. R. Church, M. N. Fouad, E. P. Gelmann, D. J. Reding, J. L. Weissfeld, L. A. Yokochi, B. O'Brien, J. D. Clapp, J. M. Rathmell, T. L. Riley, R. B. Hayes,

B. S. Kramer, G. Izmirlian, A. B. Miller, P. F. Pinsky, P. C. Prorok, J. K. Gohagan, and C. D. Berg. Mortality results from a randomized prostate-cancer screening trial. *The New England Journal of Medicine*, 360(13):1310–1319, 2009.

[7] S. Angenent, S. Haker, A. Tannenbaum, and R. Kikinis. On the Laplace-Beltrami operator and brain surface flattening. *IEEE Transactions on Medical Imaging*, 18:700–711, 1999.

[8] K. S. Arun, T. S. Huang, and S. D. Blostein. Least-squares fitting of two 3-d point sets. *' IEEE Transactions on Pattern Analysis and Machine Intelligence*, 9(5):698–700, September 1987.

[9] E. Bardinet, L. D. Cohen, and N. Ayache. Tracking and motion analysis of the left ventricle with deformable superquadrics. *Medical Image Analysis*, 1(2):129–149, 1996.

[10] M. S. Bartlett. Properties of sufficiency and statistical tests. *Proceedings of the Royal Society of London, Series A, Mathematical and Physical Sciences*, 160(901):268–282, May 1937.

[11] M. Baumann, P. Mozer, V. Daanen, and J. Troccaz. Prostate biopsy assistance system with gland deformation estimation for enhanced precision. In *Proc. of Medical Image Computing and Computer-Assisted Intervention*, volume 5761 of *LNCS*, pages 57–64, September, 2009.

[12] M. Baumann, P. Mozer, V. Daanen, and J. Troccaz. Prostate biopsy tracking with deformation estimation. *Medical Image Analysis*, 16(3):562–576, 2012.

[13] M. S. Bazaraa, H. D. Sherali, and C. M. Shetty. *Nonlinear Programming: Theory and Algorithms*. John Wiley and Sons Inc., 2 edition, 1993.

[14] S. Belongie, J. Malik, and J. Puzicha. Shape matching and object recognition using shape contexts. *IEEE Transactions on Pattern Analysis and Machine Intelligence*, 24(4):509–522, April 2002.

[15] P. Besl and N. McKay. A method for registration of 3D shapes. *IEEE Transactions on Pattern and Machine Intelligence (PAMI)*, 14(2):239–256, 1992.

[16] N. Betrouni, M. Vermandel, D. Pasquier, and J. Rousseau. Ultrasound image guided patient setup for prostate cancer conformal radiotherapy. *Pattern Recognition Letters*, 28:1808–1817, 2007.

[17] D. Beyersdorff, M. Taupitz, B. Winkelmann, T. Fischer, S. Lenk, S. A. Loening, and B. Hamm. Patients with a history of elevated prostate-specific antigen levels and negative transrectal US guided quadrant or sextant biopsy results: value of MR imaging. *Radiology*, 224:701–706, 2002.

[18] D. Beyersdorff, K. Taymoorian, T. Knösel, D. Schnorr, R. Felix, B. Hamm, and H. Bruhn. MRI of prostate cancer at 1.5 and 3.0 T: Comparison of image quality in tumor detection and staging. *American Journal of Roentgenology*, 185(5):1214–1220, November 2005.

[19] A. Bharatha, M. Hirose, N. Hata, S. K. Warfield, M. Ferrant, K. H. Zou, E. Suarez-Santana, J. Ruiz-Alzola, A. D'Amico, R. A. Cormack, R. Kikinis, F. A. Jolesz, and C. M. C. Tempany. Evaluation of three-dimensional finite element-based deformable registration of pre- and intraoperative prostate imaging. *Medical Physics*, 28(12):2551–2560, December 2001.

[20] A. Bhattacharyya. On a measure of divergence between two statistical populations defined by their probability distribution. *Bulletin of the Calcutta Mathematical Society*, 35:99–110, 1943.

[21] H. A. Bogers, J. P. Sedelaar, H. P. Beerlage, J. J. de la Rosette, F. M. Debruyne, H. Wijkstra, and R. G. Aarnink. Contrast-enhanced three-dimensional power Doppler angiography of the human prostate: correlation with biopsy outcome. *Urology*, 54(1):97–104, 1999.

[22] F. Bookstein. Principal warps: Thin-plate splines and the decomposition of deformations. *IEEE Transactions on Pattern Analysis and Machine Intelligence*, 11(6):567–589, June 1989.

[23] F. Bookstein. *Morphometric Tools for Landmark Data: Geometry and Biology.* Cambridge University Press, Cambridge, UK, 1991.

[24] D. Boukerroui, J. A. Noble, and M. Brady. On the choice of band-pass quadrature filters. *Journal of Mathematical Imaging and Vision*, 21:53–80, 2004.

[25] P. Boyle and J. Ferlay. Cancer incidence and mortality in Europe 2004. *Annals of Oncology*, 16(3):481–488, March 2005.

[26] K. K. Brock, C. Mnard, J. Hensel, and D. A. Jaffray. A multi-organ biomechanical model to analyze prostate deformation due to large deformation of the rectum. In *Proc. of SPIE*, volume 6143, pages 614312.1–12, 2006.

[27] T. Budiharto, P. Slagmolen, J. Hermans, F. Maes, J. Verstraete, F. V. den Heuvel, T. Depuydt, R. Oyen, and K. Haustermans. A semi-automated 2d/3d marker-based registration algorithm modelling prostate shrinkage during radiotherapy for prostate cancer. *Radiotherapy and Oncology*, 90(3):331 – 336, 2009.

[28] T. E. Byrne. A review of prostate motion with considerations for the treatment of prostate cancer. *Medical Dosimetry*, 30(3):155–161, 2005.

[29] P. Carroll and K. Shinohara. Transrectal ultrasound guided prostate biopsy. Technical report, Department of Urology, University of California, San Francisco, 2010. http://urology.ucsf.edu/patientGuides/pdf/uroOnc/Prostate_Biopsy.pdf, accessed [18th Oct, 2010].

[30] P. R. Carroll, F. V. Coakley, and J. Kurhanewicz. Magnetic resonance imaging and spectroscopy of prostate cancer. *Reviews in Urology*, 8(Suppl. 1):S4–S10, 2006.

[31] T. Chen, S. Kim, J. Zhou, D. Metaxas, G. Rajagopal, and N. Yue. 3D meshless prostate segmentation and registration in image guided radiotherapy. In *Proc. of Medical Image Computing and Computer-Assisted Intervention*, volume 5761 of *LNCS*, pages 43–50, London, UK, September 2009.

[32] M. R. Cheung and K. Krishnan. Interactive deformation registration of endorectal prostate MRI using ITK thin plate splines. *Academic Radiology*, 16(3):351–357, March 2009.

[33] N. Chrisochoides, A. Fedorov, A. Kot, N. Archip, P. Black, O. Clatz, A. Golby, R. Kikinis, and S. K. Warfield. Toward real-time image guided neurosurgery using distributed and grid computing. In *Proc. of ACM/IEEE Conference on Supercomputing (SC 2006)*, page 37, 2006.

[34] S. Cirillo, M. Petracchini, P. D. Monica, T. Gallo, V. Tartaglia, E. V. E, U. Ferrando, and D. Regge. Value of endorectal MRI and MRS in patients with elevated prostate-specific antigen levels and previous negative biopsies to localize peripheral zone tumours. *Clinical Radiology*, 63:871–879, 2008.

[35] A. Collignon, F. Maes, D. Delaere, D. Vandermeulen, P. Suetens, and G. Marchal. Automated multimodality image registration using information theory. In *Proc. of Intl. Conf. on Information Processing in Medical Imaging*, pages 287–298, 1995.

[36] D. W. Cool, J. Bax, C. Romagnoli, A. D. Ward, L. Gardi, V. Karnik, J. Izawa, J. Chin, and A. Fenster. Fusion of MRI to 3D TRUS for mechanically-assisted targeted prostate biopsy: System design and initial clinical experience. In *Proc. of MICCAI Workshop on Prostate Cancer Imaging, Computer Aided Diagnosis, Prognosis and Intervention*, volume 6963 of *LNCS*, pages 121–133, September 2011.

[37] J. R. Crouch, S. M. Pizer, E. L. Chaney, Y.-C. Hu, G. S. Mageras, and M. Zaider. Automated finite-element analysis for deformable registration of prostate images. *IEEE Transactions on Medical Imaging*, 26(10):1379–1390, October 2007.

[38] V. Daanen, J. Gastaldo, J. Y. Giraud, P. Fourneret, J. L. Descotes, M. Bolla, D. Collomb, and J. Troccaz. MRI/TRUS data fusion for brachytherapy. *International Journal of Medical Robotics*, 2(3):256–261, September 2006.

[39] E. D'Agostino, F. Maes, D. Vandermeulen, and P. Suetens. A viscous fluid model for multimodal non-rigid image registration using mutual information. In *Proc. of Medical Image Computing and Computer-Assisted Intervention*, volume 2489 of *LNCS*, pages 541–548, 2002.

[40] A. D. B. d'Aische, M. D. Craene, S. Haker, N. Weisenfeld, C. Tempany, B. Macq, and S. K. Warfield. Improved non-rigid registration of prostate MRI. In *Proc. of Medical Image Computing and Computer-Assisted Intervention*, volume 3216 of *LNCS*, pages 845–852, 2005.

[41] C. Davatzikos. Spatial transformation and registration of brain images using elastically deformable models. *Computer Vision and Image Understanding*, 66(2):207–222, 1997.

[42] H. J. de Koning, A. Auvinen, A. B. Sanchez, and et al. Large-scale randomized prostate cancer screening trials: program performances in the european randomized screening for prostate cancer trial and the prostate, lung, colorectal and ovary cancer trial. *International Journal of Cancer*, 97:237–244, 2002.

[43] L. R. Dice. Measures of the amount of ecologic association between species. *Ecology*, 26(3):297–302, 1945.

[44] C. Domokos, J. Nemeth, and Z. Kato. Nonlinear shape registration without correspondences. *IEEE Transactions on Pattern Analysis and Machine Intelligence*, 34:943–958, 2012.

[45] J. Donovan, F. Hamdy, D. Neal, T. Peters, S. Oliver, L. Brindle, D. Jewell, P. Powell, D. Gillatt, D. Dedman, N. Mills, M. Smith, S. Noble, and A. Lane. Prostate testing for cancer and treatment (ProtecT) feasibility study. *Health Technology Assessment*, 7(14):1–88, 2003.

[46] T. M. Downs, C. G. Grossfeld, K. Shinohara, and P. R. Carroll. *Image-guided cancer detection and treatment.* Humana Press Inc., Totowa, New Jersey, August 2003.

[47] A. du Bois d'Aische, M. D. Craene, S. Haker, N. Weisenfeld, C. Tempany, B. Macq, and S. K. Warfield. Improved non-rigid registration of prostate MRI. In *Proc. of Medical Image Computing and Computer-Assisted Intervention*, volume 3216 of *LNCS*, pages 845–852, Rennes, France, September 2004.

[48] O. J. Dunn. Multiple comparisons using rank sums. *Technometrics*, 6(3):241–252, August 1964.

[49] K. Eichler, S. Hempel, J. Wilby, L. Myers, L. M. Bachmann, and J. Kleijnen. Diagnostic value of systematic biopsy methods in the investigation of prostate cancer: a systematic review. *Journal of Urology*, 175(5):1605–1612, May 2006.

[50] A. Eklund, M. Andersson, and H. Knutsson. Phase based volume registration using CUDA. *IEEE ICASSP*, pages 658–661, 2010.

[51] M. R. Engelbrecht, G. J. Jager, R. J. Laheij, A. L. Verbeek, H. J. van Lier, and J. O. B. JO. Local staging of prostate cancer using magnetic resonance imaging: a meta-analysis. *European Radiology*, 12:2294–2302, 2002.

[52] P. Fallavollita, C. Burdette, D. Y. Song, P. Abolmaesumi, and G. Fichtinger. C-arm tracking by intensity-based registration of a fiducial in prostate brachytherapy. In *Proc. of the First international conference on Information Processing in Computer-Assisted Interventions*, pages 45–55, Geneva, Switzerland, 2010.

[53] B. W. Fei, J. L. Duerk, D. T. Boll, J. S. Lewin, and D. L. Wilson. Slice-to-volume registration and its potential application to interventional MRI-guided radio-frequency thermal ablation of prostate cancer. *IEEE Transactions on Medical Imaging*, 22(4):515–525, 2003.

[54] B. W. Fei, C. Kemper, and D. L. Wilson. A comparative study of warping and rigid body registration for the prostate and pelvic MR volumes. *Computerized Medical Imaging and Graphics*, 27:267–281, 2003.

[55] B. W. Fei, A. Wheaton, Z. Lee, and a. D. L. W. J. L. Duerk. Automatic MR volume registration and its evaluation for the pelvis and prostate. *Physics in Medicine and Biology*, 47:828–838, 2002.

[56] R. A. Fisher. *Statistical Methods for Research Workers.* Oliver & Boyd, Edinburgh and London, 1932.

[57] D. R. Forsey and R. H. Barrels. Hierarchcal B-spline refinement. *Computer Graphics*, 22(4):205–212, 1988.

[58] R. Francois, R. Fablet, and C. Barillot. Robust statistical registration of 3D ultrasound images using texture information. In *Proc. of IEEE International Conference on Image Processing*, volume 1, pages I–581–4, 2003.

[59] M. Friedman. A correction: The use of ranks to avoid the assumption of normality implicit in the analysis of variance. *Journal of American Statistical Association*, 34(205):109, March 1939.

[60] A. K. George, M. Sonmez, R. J. Lederman, and A. Z. Faranesh. Robust automatic rigid registration of mri and x-ray using external fiducial markers for xfm-guided interventional procedures. *Medical Physics*, 38(1):125–141, 2011.

[61] N. Geva, R. Hagege, and J. M. Francos. Parametric modeling and linear estimation of elastic deformations. In *IEEE Intl. Conference on Acoustics, Speech and Signal Processing (ICASSP)*, pages 1301–1304, May 2011.

[62] S. Ghose, A. Oliver, R. Martí, X. Lladó, J. Freixenet, J. Mitra, J. C. Vilanova, J. Comet, and F. Meriaudeau. Multiple mean models of statistical shape and probability priors for automatic prostate segmentation. In *Proc. of MICCAI Workshop on Prostate Cancer Imaging, Computer Aided Diagnosis, Prognosis and Intervention*, volume 6963 of *LNCS*, pages 35–46, September 2011.

[63] S. Ghose, A. Oliver, R. Martí, X. Lladó, J. Freixenet, J. Mitra, J. C. Vilanova, J. Comet, and F. Meriaudeau. A hybrid framework of multiple active appearance models and global registration for 3D prostate segmentation in MRI. In *Proc. of SPIE Medical Imaging-Image Processing*, volume 8314, pages 8314S–1–9, February 2012.

[64] S. Ghose, A. Oliver, R. Martí, X. Lladó, J. Freixenet, J. Mitra, J. C. Vilanova, J. Comet, and F. Meriaudeau. Statistical shape and texture model of quadrature phase information for prostate segmentation. *International Journal of Computer Assisted Radiology and Surgery*, 7(1):43–55, 2012.

[65] S. Ghose, A. Oliver, R. Martí, X. Lladó, J. Freixenet, J. Vilanova, and F. Meriaudeau. Prostate segmentation with texture enhanced active appearance model. In *Proc. IEEE International Conference on Signal-Image Technology & Internet-Based Systems*, pages 18–22, December 2010.

[66] S. Ghose, A. Oliver, R. Martí, X. Lladó, J. Freixenet, J. Vilanova, and F. Meriaudeau. Texture guided Active Appearance Model propagation for prostate segmentation. In *Proc. of MICCAI Workshop on Prostate Cancer Imaging, Computer Aided Diagnosis, Prognosis and Intervention*, volume 6367 of *LNCS*, pages 111–120, 2010.

[67] S. Ghose, A. Oliver, R. Martí, X. Lladó, J. Freixenet, J. Vilanova, and F. Meriaudeau. A probabilistic framework for automatic prostate segmentation with a statistical model of shape and appearance. In *Proc. IEEE International Conference on Image Processing*, pages 725–728, September 2011.

[68] W. S. Gosset. The probable error of a mean. *Biometrika*, 6(1):1–25, March 1908.

[69] A. Hagemann, K. Rohr, H. Stiehl, U. Spetzger, and J. Gilsbach. Biomechanical modeling of the human head for physically based, nonrigid image registration. *IEEE Transactions on Medical Imaging*, 18(10):875–884, October 1999.

[70] M. A. Haider, T. H. van der Kwast, J. Tanguay, A. J. Evans, A. T. Hashmi, G. Lockwood, and J. Trachtenberg. Combined T2-weighted and diffusion-weighted MRI for localization of prostate cancer. *American Journal of Roentgenology*, 189:323–328, 2007.

[71] A. Heidenreich, M. Bolla, S. Joniau, M. D. Mason, V. Matveev, N. Mottet, H.-P. Schmid, T. H. van der Kwast, T. Wiegel, and F. Zattoni. Guidelines on Prostate Cancer. Technical report, European Association of Urology, 2010.

[72] J. M. Hensel, C. Ménard, P. W. M. Chung, M. F. Milosevic, A. Kirilova, J. L. Moseley, M. A. Haider, and K. K. Brock. Development of multiorgan finite element-based prostate deformation model enabling registration of endorectal coil magnetic resonance imaging for radiotherapy planning. *International Journal of Radiation Oncology, Biology and Physics*, 68(5):1522–1528, 2007.

[73] A. Hill, C. J. Taylor, and A. D. Brett. A framework for automatic landmark identification using a new method of nonrigid correspondence. *IEEE Transactions on Pattern Analysis and Machine Intelligence*, 22(3):241–251, March 2000.

[74] Y. Hu, H. U. Ahmed, C. A. an D. Pendsé, M. Sahu, M. Emberton, D. Hawkes, and D. Barratt. MR to ultrasound image registration for guiding prostate biopsy and interventions. In *Proc. of Medical Image Computing and Computer-Assisted Intervention*, volume 5761 of *LNCS*, pages 787–794, 2009.

[75] Y. Hu, H. U. Ahmed, Z. Taylor, C. Allem, M. Emberton, D. Hawkes, and D. Barratt. MR to ultrasound registration for image-guided prostate interventions. *Medical Image Analysis*, 16(3):687–703, 2012.

[76] D. P. Huttenlocher, G. A. Klanderman, and W. J. Rucklidge. Comparing images using the Hausdorff distance. *IEEE Transaction in Pattern Analysis and Machine Intelligence*, 15(9):850–863, 1993.

[77] F. Ino, K. Ooyama, and K. Hagihara. A data distributed parallel algorithm for nonrigid image registration. *Parallel Computing*, 31:19–43, 2005.

[78] V. Iremashvili, L. Pelaez, M. Jorda, M. Manoharan, M. Arianayagam, D. L. Rosenberg, and M. S. Soloway. Prostate sampling by 12-core biopsy: Comparison of the biopsy results with tumor location in prostatectomy specimens. *Urology*, 79(1):37 – 42, 2012.

[79] B. Jähne. *Digital Image Processing*. Springer-Verlag, 6th edition, 2005.

[80] A. Jarc, J. Perŏs, P. Rogelj, M. Perše, and S. Kovačič. Texture features for affine registration of thermal (FLIR) and visible images. Computer Vision Winter Workshop 2007, 2007.

[81] A. Jemal, R. Siegel, E. Ward, Y. Hao, J. Xu, T. Murray, and M. J. Thun. Cancer statistics, 2008. *CA Cancer Journal for Clinicians*, 58(2):71–96, February 2008.

[82] J. Jiang, J. Colli, and R. El-Galley. A simple method for estimating the optimum number of prostate biopsy cores needed to maintain high cancer detection rates while minimizing unnecessary biopsy sampling. *Journal of Endourology*, 24:143–147, 2010.

[83] R. Jonker and A. Volgenant. A shortest augmenting path algorithm for dense and sparse linear assignment problems. *Computing*, 38:325–340, May 1987.

[84] S. Kadoury, P. Yan, S. Xu, N. Glossop, P. Choyke, B. Turkbey, P. Pinto, B. J. Wood, and J. Kruecker. Realtime TRUS/MRI fusion targeted-biopsy for prostate cancer: A clinical demonstration of increased positive biopsy rates. In *Proc. of MICCAI Workshop on Prostate Cancer Imaging, Computer Aided Diagnosis, Prognosis and Intervention*, volume 6367 of *LNCS*, pages 52–62, 2010.

[85] I. Kaplan, N. E. Oldenburg, P. Meskell, M. Blake, P. Church, and E. J. Holupka. Real time MRI-ultrasound image guided stereotactic prostate biopsy. *Magnetic Resonance Imaging*, 20:295–299, 2002.

[86] V. V. Karnik, A. Fenster, J. Bax, D. W. Cool, L. Gardi, I. Gyacskov, C. Romagnoli, and A. D. Ward. Assessment of image registration accuracy in three-dimensional transrectal ultrasound guided prostate biopsy. *Medical Physics*, 37(2):802–813, 2010.

[87] R. Keys. Cubic convolution interpolation for digital image processing. *IEEE Transactions on Signal Processing, Acoustics, Speech, and Signal Processing*, 29(6):1153–1160, 1981.

[88] A. Khamene, D. Zikic, M. Diallo, T. Boettger, and E. Rietzel. A novel intensity similarity metric with soft spatial constraint for a deformable image registration problem in radiation therapy. In *Proc. of Medical Image Computing and Computer-Assisted Intervention*, volume 5761 of *LNCS*, pages 828–836, 2009.

[89] A. P. Kirkham, M. Emberton, and C. Allen. How good is mri at detecting and characterising cancer within the prostate? *European Urology*, 50:1163–1174, June 2006.

[90] K. Kitajima, Y. Kaji, Y. Fukabori, K. Yoshida, N. Suganuma, and K. Sugimura. Prostate cancer detection with 3 T MRI: comparison of diffusion-weighted imaging and dynamic contrast-enhanced MRI in combination with T2-weighted imaging. *Journal of Magnetic Resonance Imaging*, 31:625–631, 2010.

[91] D. J. Kroon. B-spline grid, image and point based registration. http://www.mathworks.com/matlabcentral/fileexchange/20057, 2008. Accessed 29th June, 2012.

[92] W. H. Kruskal and W. A. Wallis. Use of ranks in one-criterion variance analysis. *Journal of the American Statistical Association*, 47(260):583–621, 1952.

[93] N. Lawrentschuk and U. Lindner. Recent advances in magnetic resonance imaging of prostate cancer. *F1000 Reports in Medicine*, 2:86, 2010.

[94] S. Lee, G. Wolberg, K.-Y. Chwa, and S. Y. Shin. Image metamorphosis with scattered feature constraints. *IEEE Transactions on Visualization and Computer Graphics*, 2(4):337–354, October 1996.

[95] S. Lee, G. Wolberg, and S. Y. Shin. Scattered data interpolation with multilevel B-splines. *IEEE Transactions on Visualization and Computer Graphics*, 3:228–244, July 1997.

[96] H. Levene. *Robust tests for equality of variances*. Contributions to Probability and Statistics. Stanford University Press, Palo Alto, California, I. Olkin edition, 1960.

[97] H. W. Lilliefors. On the Kolmogorov-Smirnov test for normality with mean and variance unknown. *Journal of American Statistical Association*, 62(318):399–402, June 1967.

[98] D. C. Liu and J. Nocedal. On the limited memory method for large scale optimization. *Mathematical Programming B*, 45(3):503–528, 1989.

[99] J. Lu, R. Srikanchana, M. McClain, Y. Wang, J. Xuan, I. A. Sesterhenn, M. T. Freedman, and S. K. Mun. A statistical volumetric model for characterization and visualization of prostate cancer. In *Proc. of SPIE*, volume 3976, pages 142–153, Feb 2000.

[100] G. Lughezzani, M. Sun, L. Budäus, R. Thuret, S. F. Shariat, P. Perrotte, and P. I. Karakiewicz. Effect of the number of biopsy cores on prostate cancer detection and staging. *Future Oncology*, 6:381–390, 2010.

[101] F. Maes, A. Collignon, D. Vandermeulen, G. Marchal, and P. Suetens. Multimodality image registration by maximization of mutual information. *IEEE Transactions on Medical Imaging*, 16(2):187–198, 1997.

[102] F. Maes, D. Vandermeulen, and P. Suetens. Comparative evaluation of multiresolution optimization strategies for multimodality image registration by maximization of mutual information. *Medical Image Analysis*, 3(4):373–386, 1999.

[103] J. B. A. Maintz and M. A. Viergever. A survey of medical image registration. *Medical Image Analysis*, 2(1):1–36, 1998.

[104] D. W. Marquardt. An algorithm for least-squares estimation of nonlinear parameters. *SIAM Journal on Applied Mathematics*, 11(2):434–441, 1963.

[105] C. R. Maurer, J. M. Fitzpatrick, M. Y. Wang, S. Member, R. L. Galloway, R. J. Maciunas, and G. S. Allen. Registration of head volume images using implantable fiducial markers. *IEEE Transactions on Medical Imaging*, 16:447–462, 1997.

[106] C. R. Maurer, J. J. McCrory, and J. M. Fitzpatrick. Estimation of accuracy in localizing externally attached markers in multimodal volume head images. In *Proc. of SPIE Medical Imaging*, volume 1898, pages 43–54, 1993.

[107] J. E. McNeal, E. A. Redwine, F. S. Freiha, and T. A. Stamey. Zonal distribution of prostatic adenocarcinoma. correlation with histologic pattern and direction of spread. *American Journal of Surgical Pathology*, 12(12):897–906, 1988.

[108] J. Mitra, A. Oliver, R. Martí, X. Lladó, J. C. Vilanova, and F. Meriaudeau. Multimodal prostate registration using thin-plate splines from automatic correspondences. In *Proc. of Intl. Conference on Digital Image Computing:Techniques and Applications (DICTA'10)*, pages 587–592, Sydney, Australia, Dec. 2010.

[109] T. Mizowaki, G. N. Cohen, A. Y. C. Fung, and M. Zaider. Towards integrating functional imaging in the treatment of prostate cancer with radiation: The

registration of the MR spectroscopy imaging to ultrasound/CT images and its implementation in treatment planning. *International Journal of Radiation Oncology Biology and Physics*, 54(5):1558–1564, 2002.

[110] M. H. Moghari and P. Abolmaesumi. Understanding the effect of bias in fiducial localization error on point-based rigid-body registration. *IEEE Transactions on Medical Imaging*, 29(10):1730–1738, 2010.

[111] J. M. F. nad J. B. West and C. R. J. Maurer. Predicting error in rigid-body point-based registration. *IEEE Transactions on Medical Imaging*, 17(5):694–702, October 1998.

[112] R. Narayanan, J. Kurhanewicz, K. Shinohara, E. D. Crawford, A. Simoneau, and J. S. Suri. MRI-ultrasound registration for targeted prostate biopsy. In *Proc. of IEEE Intl. Symposium on Biomedical Imaging: From Nano to Macro (ISBI'2009)*, pages 991–994, Boston, MA, June/July 2009.

[113] S. Natarajan, L. S. Marks, D. J. Margolis, J. Huang, M. L. Macairan, P. Lieu, and A. Fenster. Clinical application of a 3D ultrasound-guided prostate biopsy system. *Urologic Oncology*, 29:334–342, 2011. Seminar Article.

[114] M. A. P.-C. neda and F. Arámbula-Cosió. Resection simulations with local tissue deformations for computer assisted surgery of the prostate. In *Proc. of Mexican International Conference on Artificial Intelligence*, volume 2313 of *LNAI*, pages 450–459, 2002.

[115] J. A. Nelder and R. Mead. A simplex method for function minimization. *The Computer Journal*, 7:308–313, 1965.

[116] J. Nemeth, C. Domokos, and Z. Kato. Nonlinear registration of binary shapes. In *Proc. of IEEE International Conference on Image Processing (ICIP'09)*, pages 1001–1004, Cairo, Egypt, Nov. 2009.

[117] J. Nemeth, C. Domokos, and Z. Kato. Recovering planar homographies between 2D shapes. In *Proc. IEEE International Conference on Computer Vision (ICCV'09)*, pages 2170–2176, Kyoto, Japan, Sept. 2009.

[118] A. Y. Ng, M. I. Jordan, and Y. Weiss. On spectral clustering: Analysis and an algorithm. In *Proc. of Advances in Neural Information Processing Systems*, pages 849–856. MIT Press, 2001.

[119] M. Nielsen, P. Johansen, A. Jackson, and B. Lautrup. Brownian warps: A least committed prior for nonrigid registration. In *Proc. of Medical Image Computing and Computer-Assisted Intervention*, volume 2489 of *LNCS*, pages 557–564, 2002.

[120] S. Oguro, J. Tokuda, H. Elhawary, S. Haker, R. Kikinis, C. M. Tempany, and N. Hata. MRI signal intensity based B-spline nonrigid registration for pre- and intraoperative imaging during prostate brachytherapy. *Magnetic Resonance Imaging*, 30(5):1052–1058, 2009.

[121] R. Onur, P. J. Littrup, J. E. Pontes, and F. J. B. Jr. Contemporary impact of transrectal ultrasound lesions for prostate cancer detection. *Journal of Urology*, 172:512–514, 2004.

[122] S. Ourselin, A. Roche, S. Prima, and N. Ayache. Block matching: A general framework to improve robustness of rigid registration of medical images. In *Proc. of Medical Image Computing and Computer-Assisted Intervention*, volume 1935 of *LNCS*, pages 557–566, 2000.

[123] C. Papadimitriou and K. Stieglitz. *Combinatorial Optimization:Algorithms and Complexity*. Prentice Hall, 1982.

[124] A. Papoulis. *Probability, Random Variables and Stochastic Processes*. Mc Graw Hill, 3rd edition, 1991.

[125] D. M. Parkin, F. I. Bray, and S. S. Devesa. Cancer burden in the year 2000: the global picture. *European Journal of Cancer*, 37(Suppl 8):S4–66, October 2001.

[126] C. R. Porter, C. O'Donnell, E. D. Crawford, E. J. Gamito, J. Kim, and A. Tewari. Predicting the outcome of the random prostate biopsy. Technical report, Department of Urology, State University of New York, Stony Brook,

NY, 2010. http://www.cancernews.com/data/Article/230.asp, accessed [5th Apr, 2012].

[127] M. J. D. Powell. An iterative method for finding stationary value of a function of several variables. *The Computer Journal*, 5:47, 1962.

[128] A. Prando, J. Kurhanewicz, A. P. Borges, E. M. O. Jr., and E. Figueiredo. Prostatic biopsy directed with endorectal MR spectroscopic imaging findings in patients with elevated prostate specific antigen levels and prior negative biopsy findings: early experience. *Radiology*, 236:903–910, 2005.

[129] H. Prautzsch, W. Boehm, and M. Paluszny. *Bézier and B-spline Techniques*. Springer-Verlag, 2002.

[130] W. H. Press, B. P. Flannery, S. A. Teukolsky, and W. T. Vellerling. *Numerical recipes in C: The Art of Scientific Computing*. Cambridge University Press, London, UK, 2nd edition, 1993.

[131] W. H. Press, S. A. Teukolsky, W. T. Vetterling, and B. P. Flannery. *Numerical Recipes: The Art of Scientific Computing*. Cambridge University Press, New York, 3rd edition, 2007.

[132] R. S. Purohit, K. Shinohara, M. V. Meng, and P. R. Carroll. Imaging clinically localized prostate cancer. *Urologic Clinics of North America*, 30(2):279–293, May 2003.

[133] C. Reynier, J. Troccaz, P. Fourneret, A. Dusserre, C. Gay-Jeune, J.-L. Descotes, M. Bolla, and J.-Y. Giraud. MRI/TRUS data fusion for prostate brachytherapy. preliminary results. *Medical Physics*, 31(6):1568–1575, 2004.

[134] A. Roche, G. Malandain, X. Pennec, and N. Ayache. The correlation ratio as a new similarity measure for multimodal image registration. In *Proc. of Medical Image Computing and Computer-Assisted Intervention*, volume 1496 of *LNCS*, pages 1115–1124, 1998.

[135] K. Rohr, H. S. Stiehl, R. Sprengel, T. M. Buzug, J. Weese, and M. H. Kuhn. Landmark-based elastic registration using approximating thin-plate splines.

IEEE Transactions on Pattern Analysis and Machine Intelligence, 20(6):526–534, June 2001.

[136] M. J. Roobol and F. H. Schroder. European randomized study of screening for prostate cancer: achievements and presentation. *BJU International*, 92(Suppl. 2):117–122, 2003.

[137] D. Rueckert, L. I. Sonoda, C. Hayes, D. L. G. Hill, M. O. Leach, and D. J. Hawkes. Nonrigid registration using free-form deformations: Application to breast MR images. *IEEE Transactions on Medical Imaging*, 18(8):712–721, 1999.

[138] V. Scattoni, M. Raber, F. Abdollah, M. Roscigno, F. Dehò, D. Angiolilli, C. Maccagnano, A. Gallina, U. Capitanio, M. Freschi, C. Doglioni, P. Rigatti, and F. Montorsi. Biopsy schemes with the fewest cores for detecting 95% of the prostate cancers detected by a 24-core biopsy. *European Urology*, 57:1–8, 2010.

[139] W. Shao, R. Wu, K. V. Ling, C. H. Thng, H. S. S. Ho, C. W. S. Cheng4, and W. S. Ng. Evaluation on similarity measures of a surface-to-image registration technique for ultrasound images. In *Proc. of Medical Image Computing and Computer-Assisted Intervention*, volume 4191 of *LNCS*, pages 742–749, 2006.

[140] D. G. Shen, E. Herskovits, and C. Davatzikos. An adaptive focus statistical shape model for segmentation and shape modeling of 3d brain structures. *IEEE Transactions on Medical Imaging*, 20:257–271, 2001.

[141] D. Shepard. A two-dimensional interpolation function for irregularly-spaced data. In *Proc. of the 1968 23rd ACM national conference*, pages 517–524, 1968.

[142] A. K. Singh, J. Kruecker, S. Xu, N. Glossop, P. Guion, K. Ullman, P. L. Choyke, and B. J. Wood. Initial clinical experience with real-time transrectal ultrasonography-magnetic resonance imaging fusion-guided prostate biopsy. *British Journal of Urology International*, 101(7):841–845, 2008.

[143] A. C. Society. Cancer facts and figures 2011. www.cancer.org/Research/CancerFactsFigures/CancerFactsFigures/cancer-facts-figures-2011, 2011. Accessed 29th June, 2012.

[144] R. R. Sokal and F. J. Rohlf. *Biometry: The principles and practice of statistics in biological research*. W. H. Freeman, New York, 3 edition, 1995.

[145] J. C. Spall. Overview of the simultaneous perturbation method for efficient optimization (http://techdigest.jhuapl.edu/td/td1904/spall. pdf). *APL Technical Digest*, 19:482–492, 1998.

[146] T. A. Stamey, N. Yang, A. R. Hay, J. E. McNeal, F. S. Freiha, and E. Redwine. Prostate-specific antigen as a serum marker for adenocarcinoma of the prostate. *New England Journal of Medicine*, 317(15):909–916, October 1987.

[147] M. Steggerda, C. Schneider, M. V. Herk, L. Zijp, L. Moonen, and H. V. D. Poel. The applicability of simultaneous TRUS-CT imaging for the evaluation of prostate seed implants. *Medical Physics*, 32(7):2262–2270, July 2005.

[148] C. Studholme, D. L. G. Hill, and D. J. Hawkes. Automated 3D registration of MR and PET brain images by multi-resolution optimization of voxel similarity measures. *Medical Physics*, 24(1):25–35, 1997.

[149] C. Studholme, D. L. G. Hill, and D. J. Hawkes. An overlap invariant entropy measure of 3D medical image alignment. *Pattern Recognition*, 32(1):71–86, 1998.

[150] R. Szeliski and S. Lavallée. Matching 3-D anatomical surfaces with non-rigid deformations using octree-splines. *International Journal of Computer Vision*, 18(2):171–196, 1996.

[151] J. Tang, X. Li, N. Wang, S. Zhang, Q. Lin, J. Li, and H. Shi. Correlation between hypoechoic nodules on ultrasonography and benign hyperplasia in the prostatic outer gland. *Journal of Ultrasound in Medicine*, 24(4):483–488, April 2005.

[152] S. Theodoridis and K. Koutroumbas. *Pattern Recognition*. Academic Press, 3rd edition, 2006.

[153] J. P. Thirion. Image matching as a diffusion process: an analogy with Maxwells demons. *Medical Image Analysis*, 2(3):243–260, 1998.

[154] B. Turkbey, P. A. Pinto, H. Mani, M. Bernardo, Y. Pang, Y. L. McKinney, K. Khurana, G. C. Ravizzini, P. S. Albert, M. J. Merino, and P. L. Choyke. Prostate cancer: value of multiparametric MR imaging at 3 T for detection-histopathologic correlation. *Radiology*, 255:89–99, 2010.

[155] N. M. Ung and L. Wee. Fiducial registration error as a statistical process control metric in image-guidance radiotherapy with fiducial markers. *Physics in Medicine and Biology*, 56:7473–7485, 2011.

[156] W. J. van de Ven, G. J. Litjens, J. O. Barentsz, T. Hambrock, and H. J. Huisman. Required accuracy of MR-US registration for prostate biopsies. In *Proc. of MICCAI Prostate Cancer Imaging*, volume 6963 of *LNCS*, pages 92–99, 2011.

[157] J. Veltman, T. Goossen, P. Laguna, H. Wijkstra, and J. de la Rosette. New technical improvements for TRUS in the diagnosis of prostate cancer. *European Urology Supplements*, 1:8–14, 2002.

[158] J. C. Vilanova, C. Barceló-Vidal, J. Comet, M. Boada, J. Barceló, J. Ferrer, and J. Albanell. Usefulness of prebiopsy multi-functional and morphologic MRI combined with the free-to-total PSA ratio in the detection of prostate cancer. *American Journal of Roentgenology*, 196(6):W715–W722, 2011.

[159] P. Viola and W. Wells. Alignment by maximization of mutual information. *International Journal of Computer Vision*, 24(2):137–154, 1997.

[160] S. Vishwanath, B. N. Bloch, M. Rosen, J. Chappelow, R. Toth, N. Rofsky, R. Lenkinski, E. Genega, A. Kalyanpur, and A. Madabhushi. Integrating structural and functional imaging for computer assisted detection of prostate cancer on multi-protocol *In Vivo* 3 Tesla MRI. In *Proc. of SPIE*, volume 7260, pages 72603I.1–12, 2009.

[161] G. Wahba. *Spline Models for Observational Data*. Society for Industrial and Applied Mathematics, Philadephia, PA, 1990.

[162] A. D. Ward, C. Crukley, C. A. McKenzie, J. Montreuil, E. Gibson, C. Romagnoli, J. A. Gomez, M. Moussa, J. Chin, G. Bauman, and A. Fenster. Prostate: Registration of digital histopathologic images to in vivo mr images acquired by using endorectal receive coil. *Radiology*, 2012. doi:10.1148/radiol.12102294.

[163] A. E. Wefer, H. Hricak, D. B. Vigneron, F. V. Coakley, Y. Lu, J. Wefer, U. Mueller-Lisse, P. R. Carroll, and J. Kurhanewicz. Sextant localization of prostate cancer: comparison of sextant biopsy, magnetic resonance imaging and magnetic resonance spectroscopic imaging with step section histology. *Journal of Urology*, 164:400–404, 2000.

[164] Z. Wei, G. Wan, L. Gardi, G. Mills, D. Downey, and A. Fenster. Robot-assisted 3D-TRUS guided prostate brachytherapy: System integration and validation. *Medical Physics*, 31(3):539–548, 2004.

[165] B. L. Welch. The generalization of 'studentś' problem when several different population varlances are involved. *Biometrika*, 34(1-2):28–35, 1947.

[166] W. M. Wells, P. Viola, H. Atsumi, S. Nakajima, and R. Kikinis. Multi-modal volume registration by maximization of mutual information. *Medical Image Analysis*, 1(1):35–51, 1996.

[167] G. Xiao, B. Bloch, J. Chappelow, E. Genega, N. Rofsky, R. Lenkinski, and A. Madabhushi. A structural-functional MRI-based disease atlas:application to computer-aided-diagnosis of prostate cancer. In *Proc. of SPIE Medical Imaging:Image Processing*, volume 7623, pages 762303.1–12, Feb, 2010.

[168] S. Xu, J. Kruecker, B. Turkbey, N. Glossop, A. K. Singh, P. Choyke, P. Pinto, and B. J. Wood. Real-time MRI-TRUS fusion for guidance of targeted prostate biopsies. *Computer Aided Surgery*, 13(5):255–264, 2008.

[169] P. Yan, S. Xu, B. Turkbey, and J. Kruecker. Optimal search guided by partial active shape model for prostate segmentation in trus images. In *Proc. of SPIE Medical Imaging*, volume 7261, pages 72611G.1–72611G.11, 2009.

[170] J. H. Zar. *Biostatistical analysis*. Prentice Hall, Upper Saddle River, NJ, 4 edition, 1999.

[171] Y. Zhan, M. Feldman, J. Tomaszeweski, C. Davatzikos, and D. Shen. Registering histological and MR images of prostate for image-based cancer detection. In *Medical Imaging and Computer-Assisted Intervention*, volume LNCS 4191, pages 620–628, 2006.

[172] Y. Zhan, Y. Ou, M. Feldman, J. Tomaszeweski, C. Davatzikos, and D. Shen. Registering histologic and MR images of prostate for image-based cancer detection. *Academic Radiology*, 14(11):1367–1381, 2007.

[173] Y. Zhu, S. Williams, and R. Zwiggelaar. Computer technology in detection and staging of prostate carcinoma: A review. *Medical Image Analysis*, 10:178–199, 2006.

[174] B. Zitová and J. Flusser. Image registration methods: a survey. *Image and Vision Computing*, 21:977–1000, 2003.